Università degli Studi Roma Tre

Scuola Dottorale in Geologia dell'Ambiente e delle Risorse XXVIII Ciclo Sezione Geologia

Assessment of Soil Shaking Features in Urban Areas

PhD Student Dott. Maurizio Piersanti

Tutor Prof. Giuseppe Della Monica

Co-Tutor Arrigo Caserta PhD

Roma, 11 marzo 2016

INDEX

1. INTRODUCTION

The damages produced during moderate and large earthquakes are principally influenced by the interaction of seismic wavefield with the shallow subsurface geology and soil conditions. For this reason the degree of shake-ability of the ground during strong ground motion at locations with high vulnerability has been a matter of growing interest in seismological investigations dealing with seismic hazard analysis. Site amplifications in shallow unconsolidated sediments can be predicted using the theory of linear elastic wave propagation and computing S-wave resonances due to reverberation of seismic energy between the free surface and the sediment structure overlying a bedrock. The knowledge of the shallow shear wave velocity structure is essential for reasonable strong motion predictions at a given site. The assessment of soil shaking features in urban areas is crucial to quantify the expected local seismic response under strong motion conditions. During last decades many studies of this kind were conducted on some big cities (Fäh et al. 1997; Faccioli 1999; Jimenez et al. 2000; Raptakis et al. 2004; Panza et al. 2004; Ansal et al. 2010).

The city of Cosenza is located in the southern part of the Crati Basin in the Calabria region, geologically taken part of the Calabrian Arc. As well as the southern Apennines and eastern Sicily, it represents a very active tectonic area, in particular one of the most active area in the entire Mediterranean Region. Many geological studies were performed in the Crati Basin (Tortorici et al., 1995, Van Dijk et al., 2000, Spina et al., 2011, Tortorici et al., 2002), with the aim to reconstruct the actual stratigraphy of the area and to define its structural geological setting. The historical centre of Cosenza has been affected by numerous earthquakes during last years causing many damages to its architectural heritage; nevertheless, until now, no detailed geotechnical studies on the near-surface geology are available in literature. In order to fill this gap and better understand and quantify the expected ground shaking within the city of Cosenza, a multidisciplinary research project called pon-MASSIMO (http://openmap.rm.ingv.it/ponmassimo/) was carried on and a detailed analysis was made of the physical and mechanical properties of the different lithotypes constituting the recent sedimentary fill of Crati valley.

One of the purposes of the MASSIMO project is to study and monitor the response of different types of constructions to seismic stress by considering the near-surface geology, the topographic characteristics and the elastic properties of soils in relation to the monument architectural and static preservation. The selected Test Site is the Calabria Region (Italy), where some preliminary architectural constructions have been selected in three main urban areas, i.e. Cosenza, Vibo Valentia and Reggio Calabria. As mentioned before, this PhD thesis analyses in detail the urban area is the city of Cosenza.

1.1 Objectives of the PhD Project

The main purposes of this PhD dissertation are

- Realize a geological reconstruction of the top of the bedrock

- Assess possible site effects in the area of the Test Site chosen by the MASSIMO project: the *San Agostino Church* and the *Monumental Complex of the Bretti&Enotrii* in the city of Cosenza;

The choice of the specific Test Site was made by the Cultural Heritage, considering its architectural and Historical importance for the city of Cosenza. The aforementioned purposes are reached by means of several techniques and different approaches, in particular inversion techniques in the context of ambient vibration methods in order to obtain vertical shear-wave velocity profiles and laboratory tests on sampled soils. A special attention has been paid to the reliability of the inverted profiles and to the possibility of including information from other types of experiments in the inversion process. The derivation of one-dimensional shear-wave velocity profiles from surface wave dispersion curves is a classical inversion problem in geophysics, generally solved using linearized methods (see Tarantola for further readings). The inversion of dispersion curves is known to be strongly non-linear and affected by non-uniqueness, i.e. various models may explain the same data set with an equal misfit. During this thesis, we used the open source program GEOPSY (www.geopsy.org) which uses the Neighbourhood Algorithm (Sambridge, 1999a, 1999b, Wathelet et al, 2004, Wathelet, 2008) for inverting dispersion curves. The software allows the inclusion of prior information on the different parameters and a major effort has been made to optimize the computation time at the different stages of inversion, including frequency

information measured with the H/V technique. This has been necessary to design a geognostic drillings campaign, and to calibrate and compare the dynamic geological profiles.

1.2 Thesis Outline

This Doctoral Thesis has been organised in three different blocks. The first part describes the state of art of the geological knowledge of the Crati Basin, that is the regional context where the city of Cosenza is located. The second part is pure methodological: it tries to give an insight to the different methodologies used to evaluate site effects and to assess the dynamic behaviour of soils; great emphasis is given to the characteristics of surface waves and their use for site characterization. The remaining part presents the results of the application of the methods described and the relative conclusions.

- **Section 1** In this Section a geological overview of the Crati Basin and in particular of the area of city of Cosenza is presented; such overview includes geological settings, morpho–tectonics, seismology and hydrogeology of the Crati Basin.
- **Section 2** Describes the characteristics of the seismic waves, both body waves and surface waves; particular emphasis is given to the surface waves, especially to their dispersive characteristic and their use for site characterization.
- **Section 4** The concept of *site effects* is presented. More in detail the techniques used to evaluate it are presented, including seismic noise analysis (Nakamura technique, seismic arrays), and laboratory tests (grain-size analysis, resonant column and cyclic torsional shear tests). The phenomenon of soil liquefaction is also introduced, including simplified techniques used to evaluate it.
- **Section 5** In this section all the results of the study are presented**.**
- **Section 6** Some comments and conclusions are summarised, together with the indication of some specific topics, about which some further research efforts are needed in the future.

Le savant n'étudie pas la nature parce que cela est utile; il l'étudie parce qu'il y prend plaisir et il y prend plaisir parce qu'elle est belle. Si la nature n'était pas belle, elle ne vaudrait pas la peine d'être connue, la vie ne vaudrait pas la peine d'être vécue. Je ne parle pas ici, bien entendu, de cette beauté qui frappe les sens, de la beauté des qualités et des apparences; non que j'en fasse fi, loin de là, mais elle n'a rien à faire avec la science; je veux parler de cette beauté plus intime qui vient de l'ordre harmonieux des parties, et qu'une intelligence pure peut saisir.

The scientist does not study nature because it is useful to do so. He studies it because he takes pleasure in it, and he takes pleasure in it because it is beautiful. If nature were not beautiful it would not be worth knowing, and life would not be worth living. I am not speaking, of course, of the beauty which strikes the senses, of the beauty of qualities and appearances. I am far from despising this, but it has nothing to do with science. What I mean is that more intimate beauty which comes from the harmonious order of its parts, and which a pure intelligence can grasp.

Jules Henri Poincaré

(Science et Method, 1908)

2. GEOLOGICAL SETTINGS

The city of Cosenza is located in the southern part of the Crati river Valley, a Plio-Pleistocene asymmetric half-graben with a N-S trend in the southern part and a SW-NE trend in the northern part, delimited on eastern side by the Sila Mountains and on South and West by the Catena Costiera (Figure 2.1). The graben is filled by Tertiary and Quaternary (from Late Miocene up to Present) clastic deposits (essentially gravels, sands and clays) overlying a Palaeozoic metamorphic bedrock.

Considering the aim of this work the geological succession of the Crati Basin and in detail of the urban area of Cosenza can be divided in two different groups:

1. *Sedimentary covers*: they are represented by marine deposits, composed of basal beige-clear sand and silt formation, blue clay formation and brown sand and conglomerate formation interbedded with levels of gravel, and alluvial deposits of Crati river and its tributaries.

2. *Metamorphic bedrock*: it is formed by different lithologies, such as biotite garnet-biotite gneiss and schists with acid intrusive complex (quartzdiorite, quartzmonzonite, granodiorite and granite); often, granitic outcrops are intruded into metamorphic rocks.

2.1 Geology

As mentioned above, the city of Cosenza is located in the southern part of the Crati river Valley. The Crati Basin is a tectonic depression (graben) located in the western sector of northern Calabria, geologically representing part of the Calabrian Arc. In the frame of the Mediterranean mobile belt, the Calabrian Arc is an arc-shaped continental fragment located between the E-W trending Sicilian Maghrebides, to the South, and the NW–SE trending Apennines, to the North. The Calabrian Arc (Figure 2.1) consists of a series of thrust nappes composed of tectonic units deriving from the deformation of different palaeo-geographic domains (Spina et al., 2011).

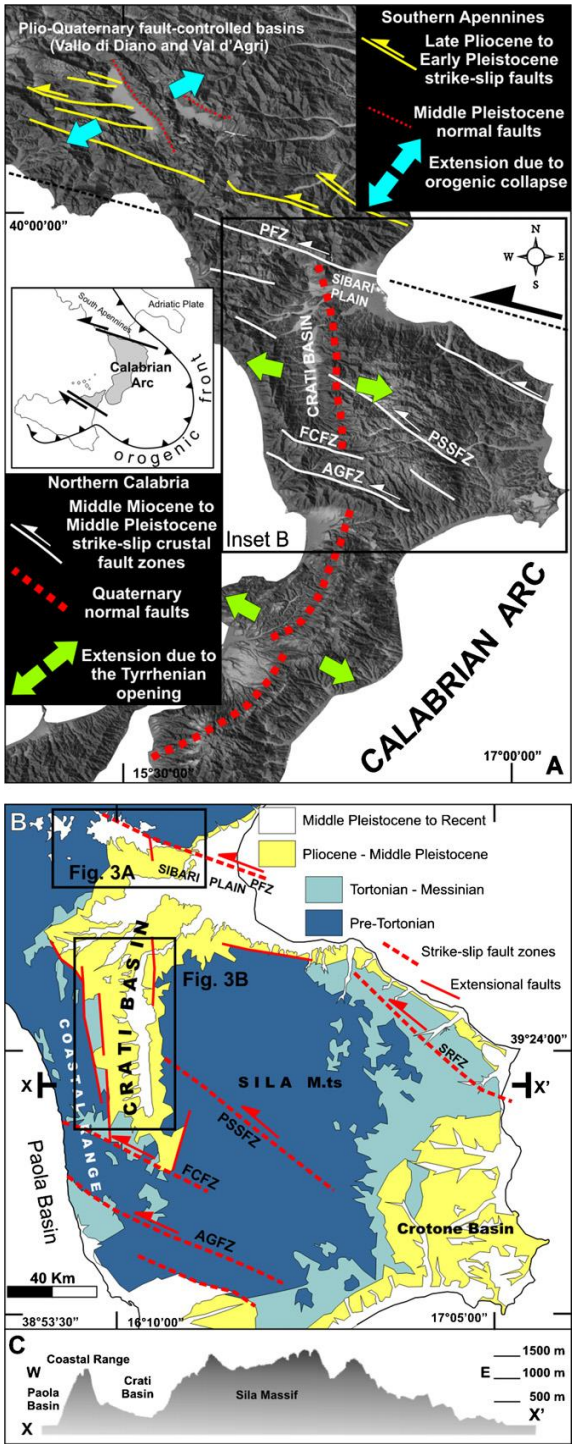

Figure 2.1 (a) Digital elevation model showing main strike-slip faults and extensional basins of the southern Apennines and northern Calabria. Major strike-slip fault zones: Pollino Fault Zone (PFZ), Petilia-S.Sosti Fault Zone (PSSFZ), Falconara-Cosenza Fault Zone (FCFZ), Amantea-Gimigliano Fault Zone (AGFZ), S.Nicola-Rossano Fault Zone (SRFZ). (b) Geological sketch of northern Calabria. (c) Topographic section across the Crati Basin, the Coastal Range and the Sila Massif (From Spina et al., 2011).

The backbone of the Calabrian Arc is composed of Palaeozoic crystalline rocks, which have been interpreted either as basement units belonging to the African continental margin or as part of the European palaeo-margin. Since the Oligocene, these basement rocks thrusted onto ophiolite-bearing units of the Neotethys domain. Since the Early Miocene, the whole tectonic edifice over-thrusted carbonate platform rocks of the Apulian continental margin.

The progressive migration of the Calabrian Arc towards the southeast occurred, since Middle Miocene times, along a NW–SE to WNW–ESE-trending regional strike-slip fault system characterized by left- and right-lateral movements in the northern and in the southern sector of the Calabrian Arc, respectively. Such faults, dissecting the pre-existing thrust sheets, played an important role in the Neogene-Quaternary geodynamic evolution of the Central Mediterranean area. Based on structural studies supported by seismic and bore-hole data, Van Dijk et al. (2000) proposed that the whole tectonic system consisted of Middle Miocene–Early Pleistocene crustal transpressional fault zones, mainly dipping towards the NE, characterized by left-lateral and reverse kinematics. Along these structures, in correspondence of their restraining bends, extrusion of the deep-seated units of the Calabrian Arc together with underlying Mesozoic carbonate rocks have been recently described by Tansi et al. (2007). Since the Middle Pleistocene, a strong regional, still active uplift affected the northern Calabrian Arc. This has been interpreted as the isostatic response to the removal of the high-density mantle/ lithosphere root, due to detachment of the Ionian subducted slab. The Crati Basin, forming part of this zone, is bounded by the Coastal Range to the west, by the Sila Massif to the east, and by the Pollino Ridge to the north (Figure 2.2). The basin is morphologically asymmetric with a steeper and shorter fluvial drainage along its eastern border, and the Crati River flowing along the easternmost side of the valley.

The Crati Basin is filled by Upper Miocene to Holocene clastic marine and fluvial deposits covering the Palaeozoic crystalline bedrock, in the southern part of the basin, and Meso - Cenozoic carbonates in its northern sector (i.e. in the Pollino area). The original stratigraphic contact between the basin infill and its bedrock is still well exposed all along the western side of the Sila Massif. Although the main depocentre is located in the northernmost sector of the basin (Sibari Plain), the thickness of the deposits increases from the Coastal Range towards the Sila foothills. Published stratigraphic data are mainly from specific sectors of the basin;

however it has been proposed that the whole basin fill consists of two main depositional sequences bounded by a regional angular unconformity. The first sequence, Late Miocene to Early Pliocene in age, is characterized in the structural highs by a Messinian unconformity, whereas the second one, spanning from the Middle-Late Pliocene to the Pleistocene, is represented by distinct lithofacies grading one into another both vertically and laterally.

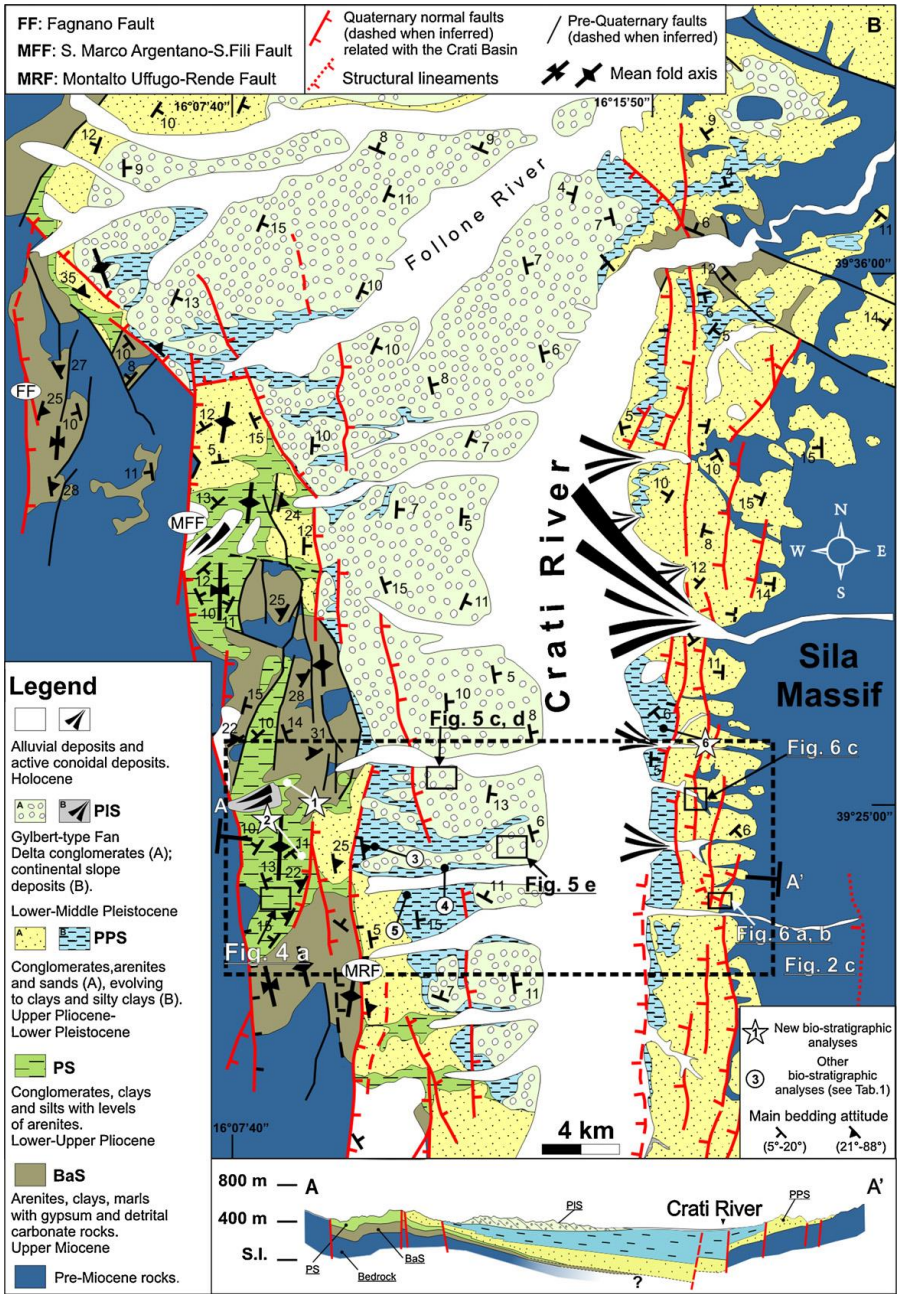

Figure 2.2 Geological maps of the Southern and Central sectors of the Crati Basin (From Spina et al., 2011).

The city of Cosenza is part of Sheet n° 236 - I NO the Geological Map of Italy (see Figures 2.3a, 2.3b); in the southernmost part of Crati river Basin the lithologies encountered in the area are:

- **Units of Gneiss, para-gneiss and biotitic-garnetiferous schistes (*sbg*) -** Form the basis upon which the various sedimentary units; this complex, rarely outcropping in the urban area of Cosenza, consists of para-gneiss and biotitic schists, often with garnets visible to the naked eye, with frequent injections of granitic material from fine-grained to coarse-grained. The condition of considerable mechanical loosening, evidenced by the numerous and often approximated lines of discontinuity, promotes the disruptive action and chemical alteration of atmospheric agents, and therefore, the formation of debris and alteration coverage present over most of surface outcrop of the formation. The permeability is generally low, with substantial increase in degraded and fractured areas. The processes of alteration and degradation tend to decrease with depth and the thickness of the altered material is usually minimal in areas subject to intense erosion (like the engravings valleys and slopes with steepness greater than 35%), while it reaches a maximum of a few tens of meters in the less steep and with plenty of water circulation. Therefore, in relation to different physical-mechanical behaviour, in the areas of outcrop of the formation, from ground level down, it is necessary to distinguish the following levels: - Angular pebbles of various sizes set in a sandy matrix containing clay and topsoil, at higher surface; - Rocky mass with degraded areas, at this level fractures tend to be filled by fine materials transported by water circulating; - Compact bedrock. The geotechnical behaviour of the geological formation is strictly depending on the state of continuity and alterations of the same: where the rock is fresh presents a high erosion resistance and low permeability, where instead is altered and degraded presents high permeability and low resistance to erosion.

- **Units of Sands (P^{S}_{2-3}; P^{S}_{3}) -** This geological formation is more widespread within the urban area. The complex consists of clear brown to medium-grained sands, sometimes through a micro-conglomerates. The formation is intercalated with thin layers of silty-clay and gravel lenses with polygenic elements. The upper part of the series in many cases is mainly composed of gravels, sands

and conglomerates subject. The complex is generally compact and has a moderate resistance to erosion. Its permeability is generally high.

- **Units of Clays, Silty Clays (P^{a}_{3}; $P^{a}_{2\text{-}3}$) -** The clays of this unit are light gray coloured. They look to be massive to thinly laminated, locally interbedded light brown silt layers, sometimes containing, up to the roof of the sequence, interbedded conglomerates and sands. Pass gradually upwards to sands with intercalated layers of clayey and sandy. The erosion resistance of the formation is poor and low permeability.

- **Unit of Conglomerates (P^{cl}_{3}) -** Constitute the major summit of the slopes of the hill of the municipality, in fact, can be traced along the axes of erosion of many small valleys. The formation outcrops mainly in the hydrographic right of the River Crati along the section before Sila, even at altitudes higher than 600/700 m above sea level. The sequence consists of conglomerates rich in matrix coloured red and pink, with elements of various sizes, up to decimetre, little rounded and surrounded by coarse sandy matrix. The elements that constitute the conglomerates have a variable composition from area to area: in general, consist essentially of granitic, phyllites and sedimentary rocks together, in other cases only gneissic rocks. Locally, the transition to the underlying sand is gradual and occurs by intercalation of sandy and conglomeratic levels. The complex is generally well compacted and has a good resistance to erosion. The permeability is high.

- **Conglomerates of ancient alluvial river terraces (q^{cl}) -** Represent the substrate support of the entire new city, starting from the confluence of Crati and Busento River and reaching the Campagnano Torrent. The deposits mainly consist of non-cemented gravel with sandy or clayey matrix with interbedded lenses of coarse grained sand and/or polygenic conglomerates. The thickness is generally of a few meters. The total deposits are quite constipated and have a moderate resistance to erosion. The permeability is medium to high and is a function of the particle size of the sediment.

- **Floods (a, f) –** They constitute a considerable part of the terrains in the area of study, characterized by materials deposited during the various floodings of the River Crati that have occurred relatively recently (Holocene). The deposits are gravelly/sandy/silty/clayey continental deposits, now stabilized and secured. The lithological variability, even in the short surroundings, is their most

obvious feature, depending on their formation by fluvial dynamics. Thicknesses are slightly constipated and highly permeable.

- **Recent Deposits (ac) -** Represent the deposits of loose beds of river plain, consist of gravel and sand in earthy matrix.

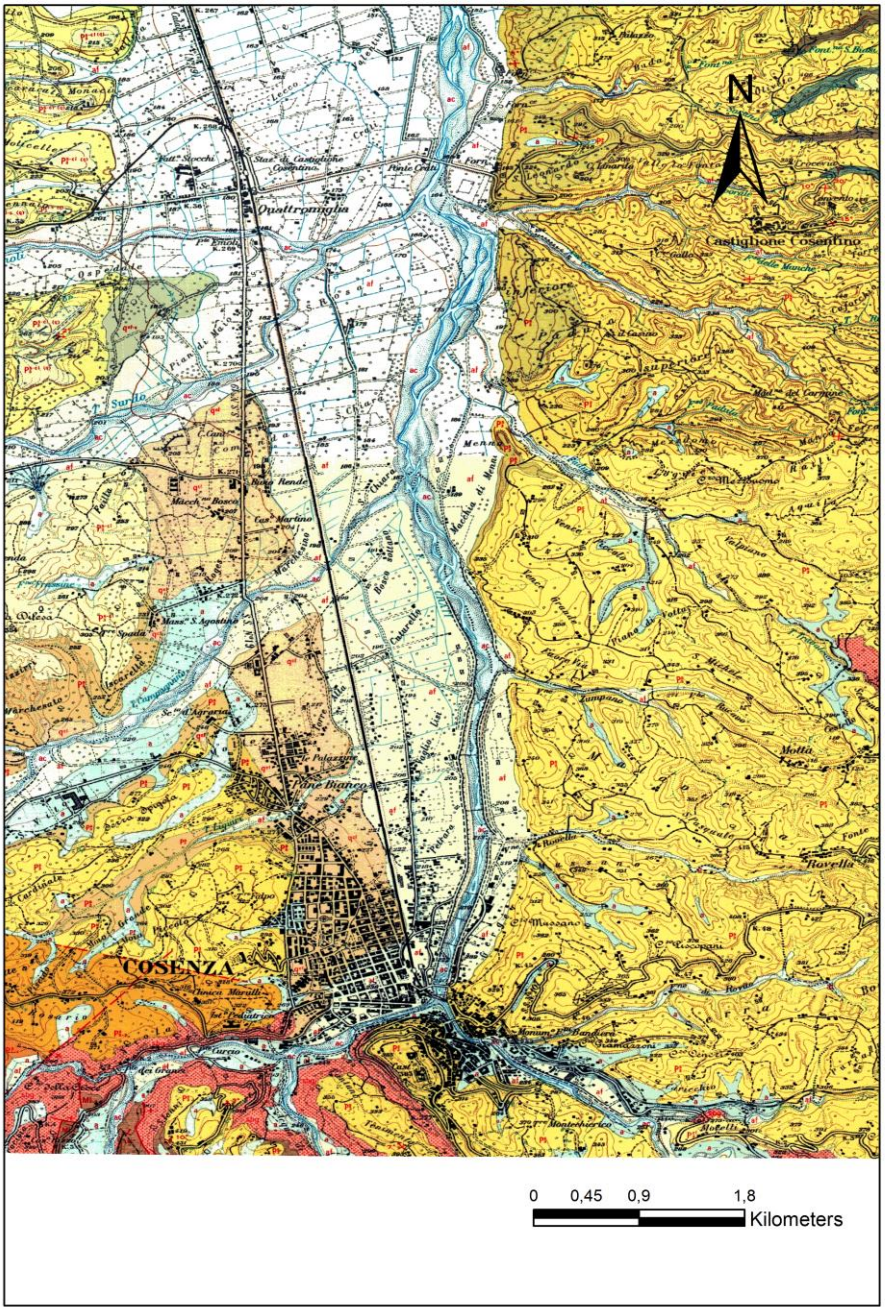

Figure 2.3a Geological map of the Crati Basin processed with ArcGis software, including Sheet n° 236 - I NO (Cosenza), and Sheet n° 229 - II SO (S. Pietro in Guarano).

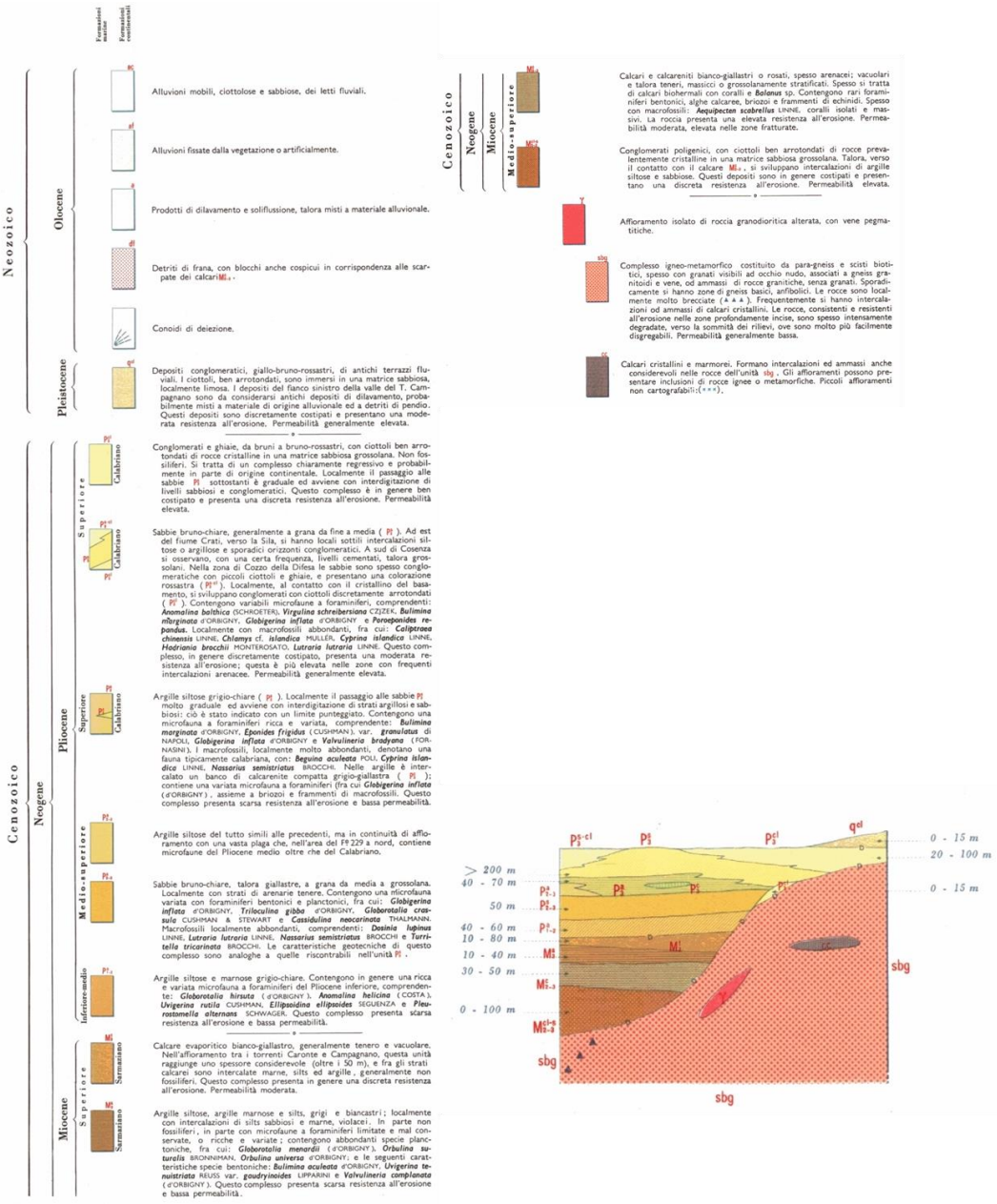

Figure 2.3b Legend of the Geological Map.

2.2 *Morpho – Tectonic*

The Crati Basin is part of a series of basins located along the Tyrrhenian side of the Calabrian Arc. According to Monaco and Tortorici (2000), these basins (including the Mesima and Gioia basins) are part of the Siculo-Calabrian Rift Zone, a sector undergoing crustal extension where basin-bounding normal faults produced strong (M≥6.5) historical earthquakes and still release seismic energy. The extensional basins are segmented by long-lived, NW–SE striking left-lateral fault zones. The various basin segments exhibit different trends. Although the recent tectonic evolution of these basins is generally accepted by most of the authors, as it was previously mentioned, their structural style and tectonic setting are still strongly debated.

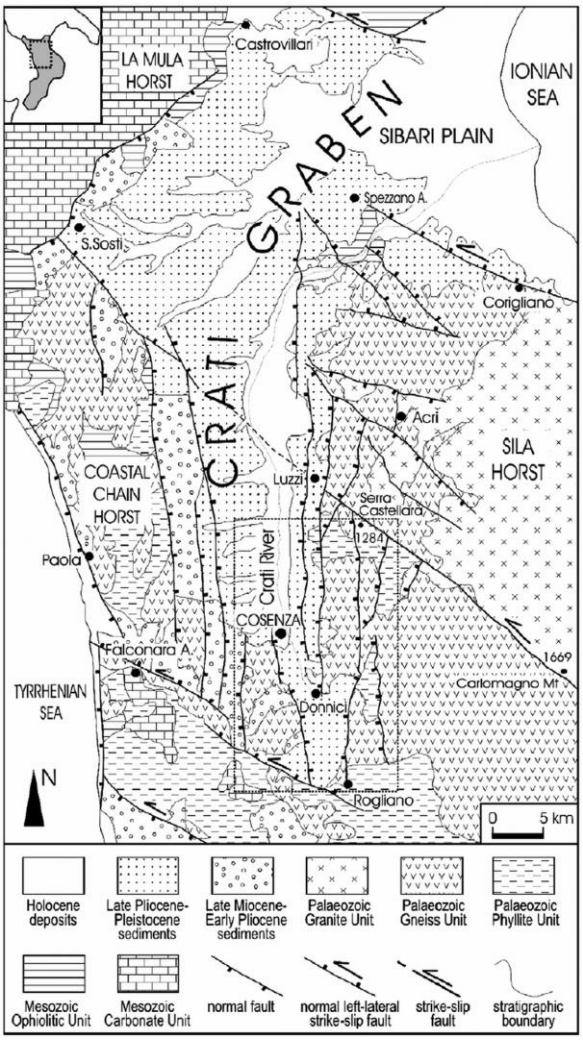

Figure 2.4 Neo-tectonic sketch of the Crati Valley (from Tansi et al., 2005).

The southern portion of the graben of the Crati Basin, geographically corresponding to the Catena Costiera-Crati Valley-Sila Plateau element, is bounded on the West and East, from stair casing normal faults systems, oriented N-S and lowered to the Crati river, culminating for discards and extension, respectively, with the lines "San Marco Argentano-San Fili" and "Rogliano-Bisignano." The faults, belonging to the N-S system, are connected to a extensional tectonics stage with axes of maximum extension oriented ESE-WNW, lasted from upper Pliocene until the end of the Pleistocene, particularly intense from the Middle Pleistocene, and is still active, as evidenced by the intense seismic activity in the region.

The northern part of the graben is more complex and characterized by two systems of normal faults, trending WNW-ESE and NE-SW. The first is inherited from a previous left strike slip band, of regional significance (Pollino Line) that has developed on the border between Calabria and Basilicata valley during the lower-middle Pleistocene. During the late Pleistocene extensional stages, these faults have been reactivations "in normal".

In the Crati valley, the fault system WNW-ESE is the director of "San Sosti-Luzzi," which marks the transition between the southern and northern part of the graben, and the lineation of "Spezzano Albanese-Cirò Marina" (Fault of Rossano) that delimits the northern outcrop of the crystalline-metamorphic units outcropping in the Sila Plateau. As for the faults that make up the Pollino Fault, these guidelines also show evidence of double kinematic mechanism.

The system of NE-SW normal faults is less evident and finds its highest expression in Sangineto Line which skirts the Crati graben to the N-W. Various authors attribute an important role in the geodynamic structure: the formation of the Crati basin is in fact attributed to the activity of left strike slip of Sangineto Line. Even the faults belonging to the system NE-SW have been reactivated by Quaternary tectonics associated with the late extensional phase.

2.3 Seismology

The Calabrian Arc, as well as the southern Apennines and eastern Sicily, represents a very active area, in particular one of the most active area in the entire Mediterranean Region, characterized by historic crustal events, the largest of which reached (in the latest 6 centuries) an MKS intensity of X – XII ($6 < M \leq 7.1$), and by

the occurrence of intermediate and deep focus earthquakes located along the inner side of the arc, beneath the southern Tyrrhenian sea. The occurrence in the Calabrian Arc of both intense Quaternary faulting and active crustal seismicity suggest that these phenomena must be related to each other. Events of high intensity (I = IX-X MCS) have repeatedly affected the territories of Cosenza (1835, 1854, 1870), Bisignano (1184, 1887) and Roggiano Gravina (1913).

The city of Cosenza has been affected by numerous earthquakes, such as the earthquakes of 12 October 1835, with maximum intensity (Intensity X) in Castiglione Cosentino, 12 February 1854 (Intensity X in Donnici) and 4 October 1870 (Intensity X in Mangone). Cosenza and its surroundings tend to be severely affected by shocks even with its epicenter in nearby areas, as evidenced by the reconstruction of the effects of the earthquakes of 27 March 1638 and 8 September 1905.

In order to characterize the historical seismicity of the city of Cosenza the "Catalogue of strong earthquakes in Italy from 491 BC to 1997" - ***CFTI***, "***P***arametric ***C***atalog of ***I***talian earthquakes" (http://storing.ingv.it/cfti4med/, the "Italian macroseismic database" (http://emidius.mi.ingv.it/CPTI11/) and DBMI11 (http://emidius.mi.ingv.it/DBMI11/), "***C***atalogue of the ***I***talian ***S***eismicity, 1981 to 2002" - CSI 1.1 were consulted. All these database are provided by ***INGV*** (***I***stituto ***N***azionale di ***G***eofisica e ***V***ulcanologia, Italy, http://terremoti.ingv.it/it/).

I[MCS]	Data	Ax	Np	Io	Mw
9	1184 05 24	Valle del Crati	6	9	6.74 ±0.44
7	1556 11 17	COSENZA	1	7	5.14 ±0.34
8-9	1638 03 27 15:05	Calabria	213	11	7.03 ±0.12
8	1638 06 08 09:45	Crotonese	42	10	6.89 ±0.25
HD	1656 06	Calabria, Cosenza	1	7-8	5.35 ±0.34
5	1659 11 05 22:15	Calabria centrale	126	10	6.55 ±0.13
4	1693 01 08 22:15	Calabria settentrionale	8	8	5.67 ±0.69
5	1738 06	Pizzo (VV)	4	6-7	4.93 ±0.34
F	1743 02 20 16:30	Basso Ionio	77	9	7.13 ±0.19
5-6	1744 03 21 20:00	Crotonese	29	8	5.74 ±0.44

I[MCS]	Data	Ax	Np	Io	Mw
7	1767 07 14 01:05	Cosentino	8	8-9	5.98 ±0.61
7	1783 03 28 18:55	Calabria	323	11	6.98 ±0.08
F	1805 07 26 21:00	Molise	223	10	6.62 ±0.11
6-7	1832 03 08 18:30	Crotonese	101	10	6.59 ±0.16
8	1835 10 12 22:35	Cosentino	36	9	5.83 ±0.32
6-7	1836 04 25 00:20	Calabria settentrionale	46	9	6.20 ±0.25
8	1854 02 12 17:50	Cosentino	89	10	6.21 ±0.16
5	1857 12 16 21:15	Basilicata	340	11	7.03 ±0.08
3	1869 11 28	VIBO VALENTIA	21	5-6	4.66 ±0.34
7-8	1870 10 04 16:55	Cosentino	56	9-10	6.10 ±0.19
2-3	1873 03 12 20:04	Marche meridionali	196	8	5.95 ±0.10
3	1875 12 06	S.MARCO IN LAMIS	97	8	5.98 ±0.16
7	1886 03 06	COSENTINO	11	7-8	5.55 ±0.60
5	1887 12 03 03:45	Calabria settentrionale	142	8	5.49 ±0.14
4	1894 11 16 17:52	Calabria meridionale	303	9	6.07 ±0.10
6	1905 09 08 01:43	Calabria meridionale	895		7.04 ±0.16
4	1907 10 23 20:28	Calabria meridionale	274	8-9	5.87 ±0.25
4-5	1908 03 01 05:23	NICASTRO	30	5	4.72 ±0.25
6	1908 12 28 04:20	Calabria meridionale-Messina	800	11	7.10 ±0.15
6	1913 06 28 08:52	Calabria settentrionale	151	8	5.66 ±0.14
4	1947 05 11 06:32	Calabria centrale	254	8	5.70 ±0.13
4	1963 11 12 08:22	BISIGNANO	10	4-5	4.29 ±0.46
4-5	1996 04 27 00:38	Cosentino	123	6-7	4.86 ±0.11
4-5	1997 07 08 08:13	Cosentino	52	5	4.31 ±0.18
4-5	2001 10 18 11:02	Cosentino	115	5-6	4.31 ±0.09

Table 2.1 Historical seismicity in the city of Cosenza (from http://emidius.mi.ingv.it/DBMI11/): **I** is the intensity resented in the city of Cosenza, $\mathbf{N_p}$ is the number of points of intensity (locations affected by the event), $\mathbf{I_0}$ is the epicentral intensity, $\mathbf{M_w}$ is the moment magnitude scale.

Another important means used to characterize the seismicity of the Crati Basin is the ***DISS***, (***D***atabase of ***I***ndividual ***S***eismogenic ***S***ources - INGV, http://diss.rm.ingv.it/diss/) through which three individual seismogenetic sources have been defined in the study area. An individual seismogenic source is defined by geological and geophysical data and is characterized by a full set of geometric (strike, dip, length, width and depth), kinematic (rake), and seismological parameters (single event displacement, magnitude, slip rate, recurrence interval). Each parameter is then rated for accuracy. Individual seismogenic sources are assumed to exhibit strictly-periodic recurrence with respect to rupture length/width, slip per event, and expected magnitude. They are compared to worldwide databases for internal consistency in terms of length, width, single event displacement and magnitude, and can be augmented by fault scarp or fold axis data when available (usually structural features with documented Late Pleistocene – Holocene activity).

The three individual seismogenetic sources defined in the Crati Basin are shown in the Figure 2.5:

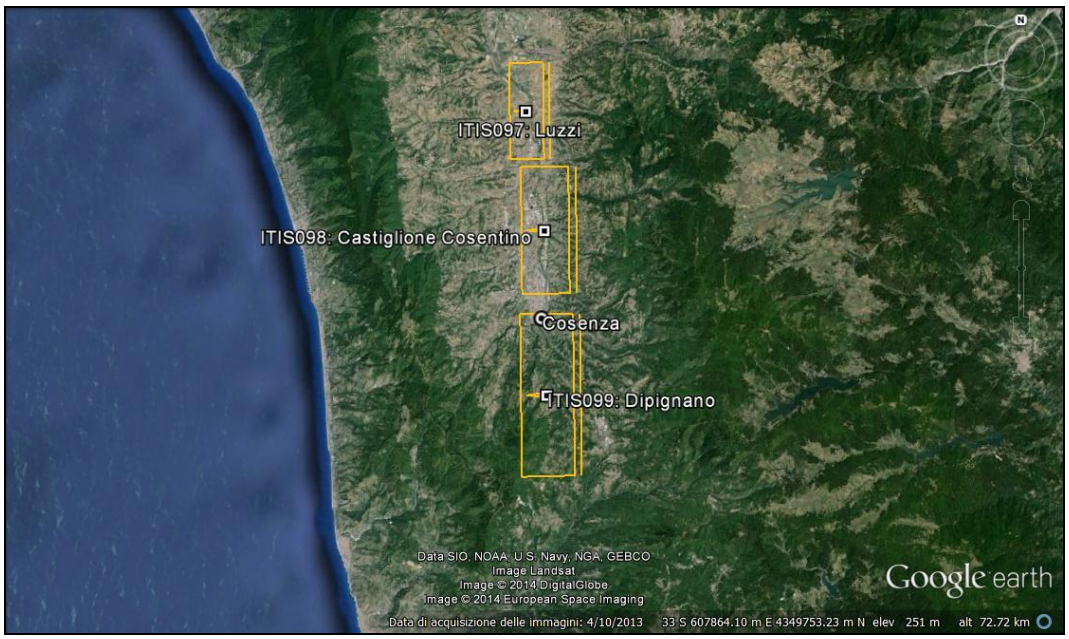

Figure 2.5 Location of the individual seismogenetic sources defined in the Crati Basin (from http://diss.rm.ingv.it/diss/).

- ***Luzzi Source***: it is based on data regarding the recent tectonic activity of the southern sector of the Crati Valley constrained by the occurrence of the 14 July 1767 earthquake (Mw 5.8). Luzzi Source is located along the eastern side of the

valley, between the Mucone River and the Caprio Creek. The drainage pattern shows that the Crati River flows closer to the eastern side of the Valley, thus suggesting a possible active subsidence of that side of the valley. The geometry of this source has been constrained mainly by geological and geomorphological observations, in particular the drainage pattern and the deformation of the top of the metamorphic substratum along with the overlying Pleistocene units, highlighted by Carobene and Damiani (1985). The location of this source is constrained to the south by the occurrence of another Mw 5.9 earthquake on 12 october 1835 (CPTI, 2004). The following geometrical parameters are proposed for the source: the strike (N180°) is chosen according to that of Crati Valley fault system; the fault dips 65° towards the West, according to geological and geomorphological data; the rake is assumed to be 270° (pure normal faulting), based on geodynamic considerations and focal mechanisms of the area; the length (7.6 km) is constrained by the geological section of Carobene and Damiani (1985) and by scaling relationships with the 1767 earthquake magnitude; the down-dip width (6.3 km) is obtained by scaling relationships. Maximum macroseismic intensity of the 1767 earthquake was VIII-IX and the macroseismic epicenter is located about 12 km north of Cosenza, near the Caprio Creek (DBMI04, Stucchi et al., 2007). The location of Luzzi Source is consistent with the location of the highest damage, and fit well the macroseismic pattern that suggests the activation of a shallow source.

- ***Castiglione Cosentino Source***: it is located along the eastern side of the valley, in the southernmost portion of it. The geometry of this source is constrained by geological and geomorphological observations, in particular the drainage pattern and the distribution of the radon anomalies in the area. The drainage pattern shows that the Crati River flows closer to the eastern side of the Valley, thus suggesting a possible active subsidence of that side of the valley. The orientation of the N-S trending normal fault shows a clear correlation with the geometry of radon anomalies in soil gas (according to Tansi et al., 2005b). The location of Castiglione Cosentino Source is constrained to the north by the occurrence of another Mw 5.8 earthquake on 14 July 1767 (CPTI, 2004), and to the south by the presence of a transverse structure known in literature as Vette Line. This lineament was the locus of a series of earthquakes with

magnitude between 4 and 5 that occurred in the nineteenth and twentieth centuries (CPTI, 2004). Another event having a Mw 5.2 (CPTI, 2004) took place in 1556 along the Vette Line. Maximum macroseismic intensity was X and macroseismic epicenter is located immediately NE of Cosenza (DBMI04, Stucchi et al., 2007). Macroseismic field of the 1835 event is consistent with the geometry of the proposed shallow source. We propose the following geometrical parameters for the source: the strike (N180°) is chosen according to that of Crati Valley fault system; the fault dips 60° towards the West, according to geological and geomorphological data; the rake is assumed to be 270° (pure normal faulting), based on geodynamic considerations and focal mechanisms of the area; the length (10 km) and the down-dip width (7.5 km) are constrained by scaling relationships with the 1835 earthquake magnitude.

- ***Dipignano Source***: it is based on data regarding the recent tectonic activity of the southern sector of the Crati Valley constrained by the occurrence of the 12 February 1854 earthquake (Mw 6.1). The geometry of this source is constrained mainly by geological and geomorphological observations. The location of this source is constrained to the north by the occurrence of another Mw 5.9 earthquake on 12 october 1835 (CPTI, 2004), and by the presence of well-known Vette Line. This transverse structure was the locus of a series of earthquakes with magnitude between 4 and 5 that occurred in the nineteenth and twentieth centuries (CPTI, 2004). Another event having a Mw 5.2 (CPTI, 2004) took place in 1556 along the Vette Line. The following geometrical parameters for the source are proposed: the strike (N180°) is chosen according to that of Crati Valley fault system; the fault dips 62° towards the West, according to geological and geomorphological data; the rake is assumed to be 270° (pure normal faulting), based on geodynamic considerations and focal mechanisms of the area; the length (12.7 km) is constrained by scaling relationships with the 1854 earthquake magnitude; the down-dip width (6.3 km) is obtained by scaling relationships. Maximum macroseismic intensity was X and macroseismic epicenter is located immediately NE of Cosenza (DBMI04, Stucchi et al., 2007). Macroseismic field of the 1854 event is consistent with the geometry of the proposed source.

2.4 *Hydrogeology*

The Crati River and its tributaries, within the hydrogeological basin of Sybaris, is the most important hydrographic system of the Calabria region. From the southern part of the basin, Crati flows exactly South-North up under Tarsia; there turns North-East and flows into the Ionian Sea (Figure 2.6).

Figure 2.6 Crati river in relation to its homonymous Basin .

The Crati is fed by many tributaries, some of which descend to the East or North-East from the western mountain range, while others flow out from the Sila. In the southern part of the Sila streams flow out mainly to the west; the northern part instead feeds a number of streams that flow to the northeast: some of these reach the Crati in its lower course, others go directly to the Ionian Sea. The drainage of the western flank of the western mountain range is made by rivers that descend to the west to the Tyrrhenian Sea.

The analysis of the piezometric surfaces (Celico et al., 2000) allowed to detect, at large scale, in the field of high and medium Crati Valley, the presence of an axis of preferential drainage groundwater, coinciding precisely with the riverbed of the Crati river (Cassa per il Mezzogiorno, 1977), whereas in the lower Crati Valley (the Plain of Sybaris), the changes in areas iso-piezometrics lets you highlight, along the northwestern sector, the presence of substantial water supplies from the carbonate massif of Pollino through the Plain of Castrovillari.

On the right bank of the Crati river it is clear the presence of axes drainage preferential headed to the coastal zone.

The knowledge of the terrain permeability features and the study of depositional sequences in the study area allowed to identify two main types of aquifers:

1. *Sila aquifers*: they are hosted in acid intrusive complex and in biotite and garnet-biotite gneiss and schist rocks (*sbg*);

2. *Crati river Valley aquifers*: hosted in Plio-Pleistocene sandy-gravelly-conglomeratic deposits and in Holocene alluvial deposits. These aquifers are laterally and vertically limited by impermeable Plio-Pleistocene clayey-sandy deposits.

The aquifers of the Crystalline basement are deeper and highly productive, whereas those of the Crati river Valley are more superficial and have less capacity; the crystalline basement hosts, in fact, represent a regional aquifer with a good lateral continuity. It is probable that there is a groundwater-streamwater exchange active system between the water body of crystalline basement and that occurring in the alluvial deposits. On the contrary, in the latter a series of small suspended and overlapped groundwater bodies have been characterized; they are stored in the gravel and sand levels and they seem to constitute a multilayer aquifer. The dimension and the hydraulic potential of these groundwater bodies vary with the not well-known horizontal extension of the layers in which they are stored, but probably the potentiality is limited for their low permeability. The blue clay formation represents the aquiclude level. These aquifers are however located below the riverbed and therefore presumably the river feed the groundwaters. The features of these aquifers depend also on the structural-geological settings. In fact, an active fault alignment puts into contact the post-orogenic formations with the crystalline bedrock, constituting a preferential way of infiltration and transfer of the water. However, the basement groundwater circulation is very articulated and that is also due to the heterogeneity of these rocks. Beneath the alluvial deposits, in beige clear sand and silt formation, it is probable the presence of a regional aquifer separated from the overhanging water bodies by the Plio-Pleistocene clays.

Further investigations may be aimed to define the possibility of likely connection among the Crati river valley aquifers and those hosted in the Crystalline basement and the existence of possible drainage processes between them.

3. SEISMIC WAVES

Seismic waves can be divided into progressive and standing waves. Progressive seismic waves propagate away from seismic sources; standing seismic waves, also known as free oscillation of the Earth, represent vibrations of the Earth as a whole; in particular, this kind of waves are generated by strong earthquakes.

From the point of view of the spatial concentration of energy, waves can be divided into *body waves* and *surface waves*. Body waves can propagate into the interior of the corresponding medium, whereas surface waves are concentrated along the surface of the medium. Note that instead of surface waves we should rather speak of a broader category of *guided waves*: guided waves can propagate along the surface of a medium (surface waves), along internal discontinuities, or other waveguides.

In this Chapter an overview of the main characteristics of the seismic waves is presented; particular emphasis is given to the surface waves, and their use site characterization.

3.1 Body Waves

The theory of the elasticity explains that there are two types of elastic body waves:

1. *Longitudinal waves*, also called compressional, dilatational or irrotational waves. In seismology they are also known as *P waves* (primary waves), because they represent the first waves appearing on seismograms. This waves involve compression and rarefaction of the material as the wave passes through it, but not rotation. Every particle of the medium, through which the wave passes, vibrates about its equilibrium position in the direction in which the wave travels.

2. *Transverse waves*, also called shear, rotational or equivoluminal waves. In seismology, they are also called *S waves* (secondary waves). These waves involve shearing and rotation of the material as the wave passes through it, but

not volume change. The particle motion is perpendicular to the direction of the propagation of the wave.

Consider the equation of motion for a homogeneous isotropic medium without body forces:

$$(\lambda+\mu)\nabla\nabla\cdot\vec{u}+\mu\nabla^2\vec{u}=\rho\frac{\partial^2\vec{u}}{\partial t^2},$$

where λ and μ are the Lamé coefficients, and ρ is the density (coefficient μ is the shear modulus). Assume that the displacement vector field $\vec{u}=\vec{u}(u,v,w)$ is continuous with its first derivates. For the Helmholtz theorem this vector can be decomposed into irrotational and solenoidal parts (Graff, 1975):

$$\vec{u}=\vec{\nabla}\varphi+\vec{\nabla}\times\vec{\psi},$$

In previous expression φ is the *scalar potential*, and $\vec{\psi}$ is the *vector potential*. By inserting this expression into the equation of motion and interchanging the order of some operation, we obtain

$$\nabla\left[(\lambda+2\mu)\nabla^2\varphi-\rho\frac{1}{\alpha^2}\frac{\partial^2\varphi}{\partial t^2}\right]+\nabla\times\left[\mu\nabla^2\vec{\psi}-\rho\frac{1}{\beta^2}\frac{\partial^2\vec{\psi}}{\partial t^2}\right]$$

The above equation will be satisfied if the expressions in the square brackets are constants. In a special case, when these constants are zero, we arrive at the wave equations

$$\nabla^2\varphi=\frac{1}{\alpha^2}\frac{\partial^2\varphi}{\partial t^2},\quad \nabla^2\vec{\psi}=\frac{1}{\beta^2}\frac{\partial^2\vec{\psi}}{\partial t^2},$$

where

$$\alpha=\sqrt{\frac{\lambda+2\mu}{\rho}},\quad \beta=\sqrt{\frac{\mu}{\rho}}$$

are the longitudinal and transverse wave velocities, respectively. This means that the scalar equation describes longitudinal waves, and the vector wave equation describes transverse waves.

Both longitudinal and transverse waves can propagate in solid media. However, only longitudinal waves can propagate in fluids, cause for this state of matter μ=0, consequently, β=0.

Assume now that the displacement vector is independent of the y-coordinate; this means that, at a given time, the wave parameters are constant along any line which is parallel to the y-axes. This situation occurs, for example, if a plane wave with a constant amplitude propagates in a arbitrary direction in the (x,z)-plane. Following Novotny (1999), the wave field can be decomposed into two parts; thus, we can express vector potential $\vec{\psi}$ as a sum of two vectors,

$$\vec{\psi} = \vec{\psi}_{SV} + \vec{\psi}_{SH}$$

where

$$\vec{\psi}_{SV} = \left(0, \psi_y, 0\right), \quad \vec{\psi}_{SH}\left(\psi_x, 0, \psi_z\right)$$

the displacement vector can be expressed as

$$\vec{u} = \vec{u}_{P-SV} + \vec{u}_{SH}$$

where

$$\vec{u}_{P-SV} = (u, 0, w) = \vec{\nabla}\varphi + \vec{\nabla} \times \vec{\psi}_{SV}$$
$$\vec{u}_{SH} = (0, v, 0) = \vec{\nabla} \times \vec{\psi}_{SV}.$$

Vector $\vec{u}_{P-SV}$ represent a wave motion polarized in the (x,z)-plane and consisting of a longitudinal wave (P wave, described by potential φ) and a transverse wave polarized in this vertical plane (SV wave, described by potential ψ_y).

Vector $\vec{u}_{SH}$ represents a transverse wave polarized in the horizontal plane parallel to the y-axis.

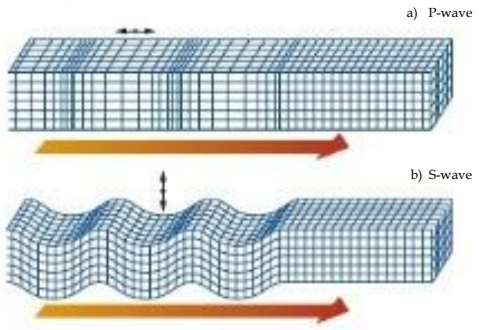

Figure 3.1 The particle motion for body waves: a) P-waves and b) S-waves.

3.2 *Surface Waves*

As suggested by the name, surface waves propagate along the surface of a medium. They are very important in seismology because they represent the principal phase of seismograms. There are two different types of surface waves:

1. *Rayleigh waves*. These waves are elliptically polarized in the plane which is formed by the normal to the surface and by the direction of propagation (Rayleigh, 1985). Near the surface of a homogeneous half-space, the particle motion is a retrograde vertical ellipse (anticlockwise for a wave travelling to the right).

2. *Love waves*. The particle motion in these waves is transverse and parallel to the surface. As opposed to Rayleigh waves, Love waves cannot propagate in a homogeneous half-space. Love waves can propagate only if the *S*-waves velocity generally increases with the distance from the surface of the medium.

The simplest medium in which Rayleigh waves can propagate is a homogeneous isotropic half-space, whereas the simplest model in which Love waves can propagate is a homogeneous isotropic layer on a homogeneous isotropic half-space. Their amplitude decreases exponentially with the depth, and most of the energy propagates in a shallow zone, roughly equal to one wavelength. The solicited zone is so bounded in depth, and consequently the wave propagation is influenced by the properties of this limited portion of soil. Surface waves do not represent principally new types of waves, but only interference phenomena of body waves (Novotny, 1999). Considering their importance, a great detail will be given to this type of elastic waves.

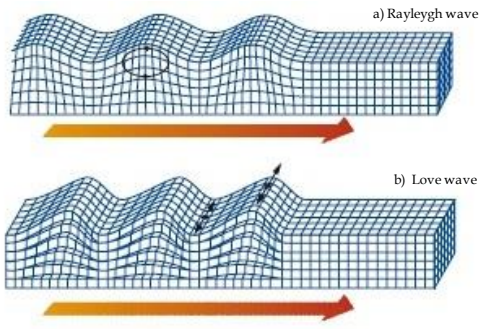

Figure 3.2 The particle motion for surface waves: a) Rayleigh waves and b) Love waves.

3.3 Dispersion of Surface Waves

As mentioned in the Introduction one of the main objective of this doctoral thesis is the derivation and the inversion of the dispersion curves of the Rayleigh waves recorded by ambient vibrations to get the shear-wave profile of the study site. In general terms we speak of the dispersion of waves if their velocity depends on frequency (Novotny, 1999; Foti, 2000). All surface waves, except Rayleigh waves in an isotropic half-space, exhibit dispersion, with the apparent velocity along the surface depending on frequency (Novotny, 1999).

Before explaining the dispersion of surface waves we have to introduce two important quantities for general propagating waves in a medium: the group velocity and phase velocity.

Consider two plane harmonic waves of angular frequencies ω_1 and ω_2 propagating along the Cartesian x-axis at velocity c_1 and c_2; for simplicity assume both waves to be of same amplitude A. Denote by u_1 and u_2 the displacements of these waves, so we have:

$$u_1 = A\sin\left[\omega_1\left(t - x/c_1\right)\right], \quad u_2 = A\sin\left[\omega_2\left(t - x/c_2\right)\right].$$

Introducing the wavenumbers $k_1 = \omega_1 / c_1$ and $k_2 = \omega_2 / c_2$ the individual waves can be expressed as

$$u_1 = A\sin\left(\omega_1 t - k_1 x\right), \quad u_2 = A\sin\left(\omega_2 t - k_2 x\right).$$

The superposition of the two waves can be expressed as

$$u = u_1 + u_2 = 2A\sin\left(\frac{\omega_1 + \omega_2}{2}t - \frac{k_1 + k_2}{2}x\right)\cos\left(\frac{\omega_1 - \omega_2}{2}t - \frac{k_1 - k_2}{2}x\right).$$

Assuming close frequencies and wavenumbers

$$\omega_1 = \omega + \Delta\omega, \quad k_1 = k + \Delta k,$$
$$\omega_2 = \omega - \Delta\omega, \quad k_2 = k - \Delta k,$$

we then obtain

$$u = 2A\sin\left(\omega t - kx\right)\cos\left(\Delta\omega t - \Delta k x\right) = \underbrace{2A\cos\left[\Delta\omega\left(t - \frac{\Delta k}{\Delta\omega}x\right)\right]}_{\text{envelope}}\sin\left(\omega t - kx\right).$$

The envelope propagates at velocity

$$U = \frac{\Delta\omega}{\Delta k}.$$

In the limiting case for small $\Delta\omega$ and Δk, we obtain the important formula

$$U = \frac{d\omega}{dk}.$$

Velocity U is called *group velocity*. In our case, this is the velocity of propagation of the envelope of the two harmonic waves. This velocity is generally different from velocity $c = \omega / k$ which is called the *phase velocity*. We can summarizes these results as follows: the individual peaks and troughs of the resulting wave (extending to a large or a finite number of propagating waves) propagate at the phase velocity, whereas their envelope propagates at the group velocity; generally the group velocity is the propagation of energy.

A transient wave (a wave of finite duration) do not change its shape during propagation in a dispersive medium because its individual spectral components (Fourier harmonics) propagate with the same phase velocities; in this case phase velocity and group velocity coincide. If the same transient wave propagates in a dispersive medium, its shape changes because its harmonics propagate with different phase velocities; in this case phase velocity and group velocity coincide. The distortion of waves causes some technical problems in the transmission of signals, and in the accurate measurements of their velocity. However, this phenomenon can be used to study the medium through which the waves have propagated.

There are two types of wave dispersion:

- Material dispersion;
- Geometrical dispersion.

The material dispersion is due to the internal structure of the substances. This type of dispersion is well known from optics, since the velocity of light in material media depends on frequency. This dispersion form the basis on spectroscopy. In the case of elastic waves, material dispersion is closely associated with their attenuation.

The geometrical dispersion is due to the interference of waves. We encounter this type of dispersion when waves propagate in thin layers, various waveguides, or

along the surface of a medium. We will study in detail such type of dispersion, such as the propagation of a wave-field in geological structures consisting in plane and parallel layers of different geotechnical properties.

Consider a surface wave. For the rest this work we shall assume a Cartesian coordinate system whose (x, y) - plane coincides with the surface of the medium, and the z-axis is positive downwards (Figure 3.3):

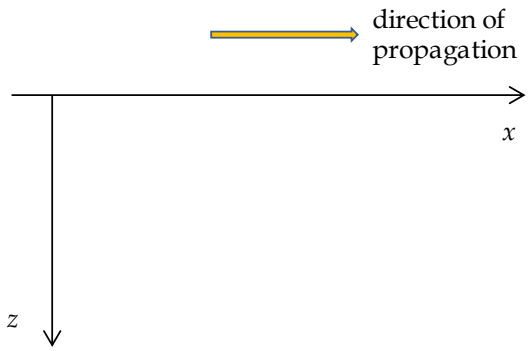

Figure 3.3 Coordinate system for the surface wave propagation.

A generic surface wave propagating in the x- direction can be expressed as it follows

$$\Psi = f(z)e^{i\omega(t-x/c)} = f(z)e^{i(\omega t-kx)},$$

with the condition

$$f(z) \to 0 \quad \text{for} \quad z \to \infty$$

The above condition describes the property of a surface wave to have an amplitude exponential decreasing with depth. We can define for this property the concept of *skin depth*, that is the depth at which the amplitude decreases by factor 1/e.

Rayleigh waves in a homogeneous, isotropic, linear elastic half-space are not dispersive; that is, their velocity of propagation is a function of the mechanical properties of the medium but not of the frequency. In vertical heterogeneous media, the phenomenon of the geometric dispersion arises, which results in the phase velocity of Rayleigh wave being frequency dependent.

Consider now the example shown in Figure 3.4, consisting in two layers overlaying a half space. On left the approximate vertical particle motion associated with low wavelength (i.e. high frequency) Rayleigh wave is shown. Most of the particle motion is confined to within about one wavelength from the free surface. In this

case, the vertical particle motion occurs almost exclusively in layer A. Hence, the material properties of layer A control the velocity of Rayleigh wave. The right side of the Figure illustrates the vertical particle motion associated with a long-wavelength (i.e. low-frequency) Rayleigh wave. In this case the particle motion extends to a greater depth, and there is significant particle motion in layer A and B, and less in layer C. The velocity of this long-wavelength Rayleigh wave is controlled by some combination of the material properties of all three layers, perhaps in rough proportion to the relative amount of particle motion occurring within each layer.

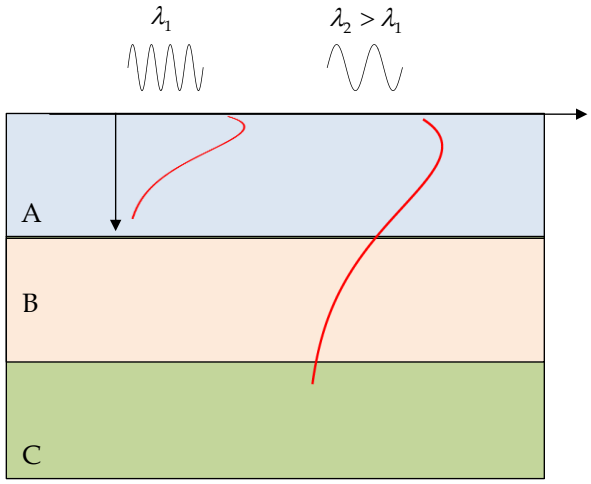

Figure 3.4 Dependence of skin depth from wavelength in a Rayleigh surface wave.

To summarize the concept behind the use of the geometric dispersion for site characterization, assume that the stratified medium in Figure 3.4 is characterized by increasing stiffness with depth, so that the shear wave velocity of the top layer is less than the velocity of the second layer, which in turn is less than the velocity of the half-space below. In this situation, a high-frequency Rayleigh wave, travelling in top layer, will have a velocity of propagation slightly lower than the shear wave velocity of the first layer. On the contrary, a low-frequency wave will travel at higher velocity because it is influenced by underlying stiffer materials as well. This concept can be extended to other frequency components. A plot of phase velocity versus wavelength will hence show an increasing trend for longer wavelengths. Considering the intimate relationship between wavelength and frequency, this information can also be represented in a plot of phase velocity versus frequency (Figure 3.5), which is commonly called *dispersion curve*.

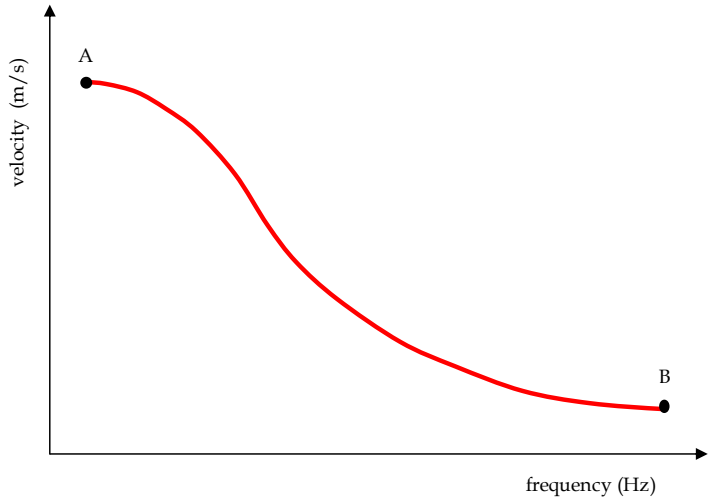

Figure 3.5 The dispersion curve describes the dispersion of surface waves: usually is depicted as phase velocity versus frequency.

The aforementioned example shows that, for vertically heterogeneous medium, the dispersion curve contains information about the variation of medium parameters with depth.

The dispersion curve can be experimentally measured and hence it is possible to interpret it in order to estimate the subsoil properties (Tokimatsu, 1995; Foti, 2000). It is a worthwhile effort to understand first which parameters actually influence the dispersion curve that can be measured.

The Rayleigh wave propagation in vertically heterogeneous media, is actually a multi-modal phenomenon: for a given stratigraphy, at each frequency different wavelength can exist. Hence different phase velocities are possible at each frequency, each of them corresponding to a mode of propagation, and the different modes can exhibit simultaneously. The different modes, except the first one, exist only above their cut-off frequency, which is for each mode the lower limit frequency at which the mode can exist: with a finite number of layers, in a finite frequency range, the number of modes is limited. At very low frequency, below the cut-off frequency of the second mode, only the first mode, known as the fundamental Rayleigh mode, exists.

Modes are not just theory or just mathematical possible solutions; they are often observed in experimental data, also in the frequency ranges of interest for a test for engineering purposes. The energy associated to the different modes depends on many factors, the stratigraphy at first, but also the depth and the kind of source.

The first mode is sometimes dominant in wide frequency ranges, but in many common situations higher modes play important roles and are actually dominant, and so they cannot be neglected. The different modes have different phase velocity, and so they separate at great distance from the source: otherwise they superimpose on to one another, and the mode identification can be impossible.

At the engineering scale the modal superposition is critical: the effective Rayleigh phase velocity deriving from the modal superposition is only an *apparent velocity*, also depending on the observation layout, on the source orientation and position.

3.4 General Setting

For the first part of this Thesis, we mainly focus on the inversion of the dispersion curves of seismic Rayleigh waves in order to obtain vertical shear stress profiles of the study area. A general scheme for this type of analysis is shown in Figure 3.6.

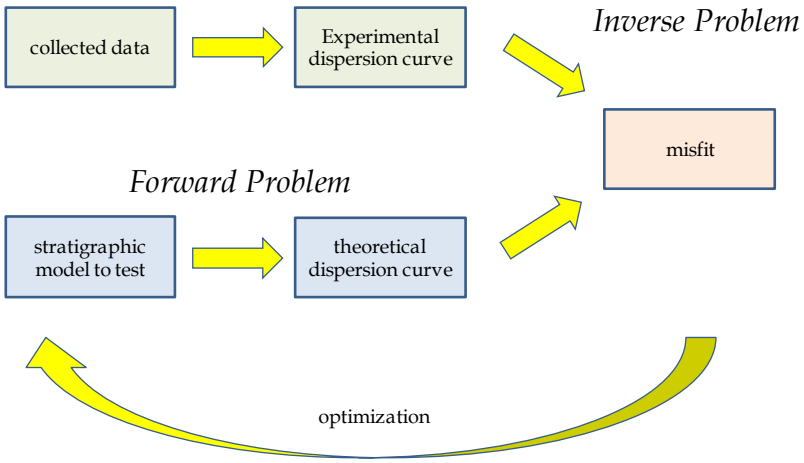

Figure 3.6 General scheme for the Thesis outline.

Surface wave methods are divided in two main categories based on the kind of sources that generate the observed signals, i.e. active and passive methods. The first ones record vibrations generated by an artificial source the frequency band of which is generally above 2 Hz (Tokimatsu, 1997). Their penetration depths are usually limited to a few tens of meters (Tokimatsu, 1997, Socco and Strobbia, 2004, Foti, 2000). On the contrary, ambient vibrations (microseisms or microtremors, if generated by nature or human activities, respectively) are produced with sources of much larger spectra, making both methods complementary for investigating deep geological structures (Wathelet et al., 2004). The determination of the

dispersion characteristics (dispersion curves) from passive recordings is first reviewed. Frequency wavenumber (*f*-k, Lacoss et al., 1969), of which conventional f-k, and high resolution frequency wavenumber (Capon, 1969) are the most popular ones.

The processing technique used in this Thesis for active experiment is a particular case of the general frequency wavenumber method. Additionally, the sensor layout deployed for the active surface wave method is the same as for refraction surveys (http://www.pasisrl.it/) and allows the measurement of Vp and Vs profiles on the first tens of meters, which brings valuable information for the inversion of the dispersion curve.

4. SITE EFFECTS

It is well known that earthquake damages strongly depend on many parameters typical of the local situation (Lanzo, 1999). Some of them concern the building vulnerability, while other ones strictly depend on the morphological configuration or shallow subsoil structure at the scale of tens to hundreds of meters; such critical phenomena are known in literature as *local* or *site seismic effects*. In particular, as an effect of the interaction between seismic input and local geomorphological/lithostratigraphical configuration, soil instabilities can be induced (soil liquefaction, landslides, etc.) or strong modification of the seismic ground motion can occur. The last effect, in particular, is responsible for most significant variations in seismic damage distribution after earthquake. Trapping of seismic waves within soft sedimentary covers overlaying a rigid bedrock (Figure 4.1) is responsible for most of this seismic amplification phenomena. Resulting resonance phenomena are able to concentrate seismic energy into a narrow frequency band (around the so called "subsoil *resonance frequencies*") producing dramatic enhancement of the relevant ground motion.

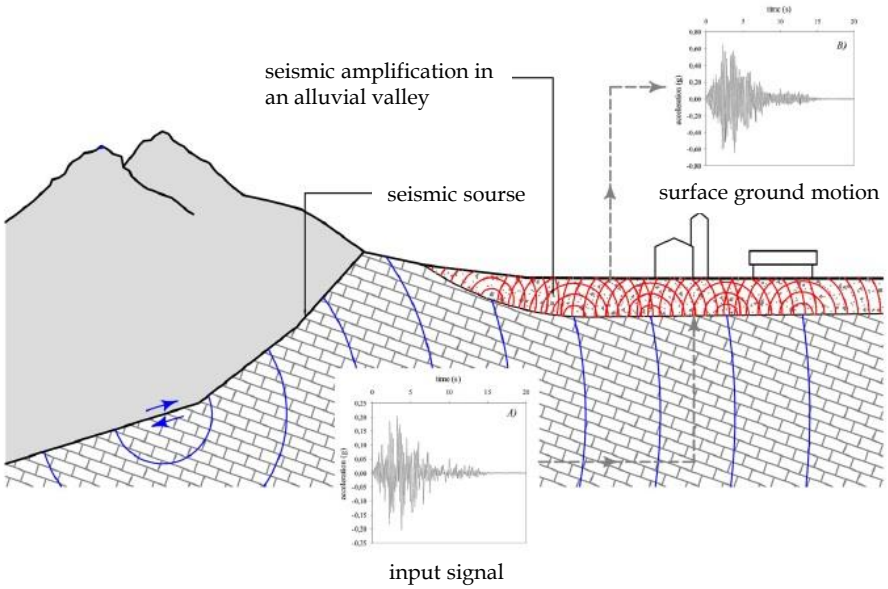

Figure 4.1 Amplification phenomena of a seismic input in shallow un-consolidated sediments overlaying a rigid bedrock (from Di Francesco, 2008, 2010).

The detection of seismic properties of the shallow subsoil responsible for dangerous amplification of the ground motion during earthquakes constitutes one of the basic goals for any seismic microzonation. In particular, detection of resonance phenomena requires the identification of major rigidity contrasts in the subsoil; in fact, seismic energy trapping ultimately depends on reflection/refraction phenomena that, on their turn, are mainly controlled by velocity variations of seismic phases in the shallow subsoil. Thus, defining depth distribution of P-wave and S-wave velocity (being these latter more important for potential damages), density and damping factors, is of paramount importance. Several survey techniques have been developed on purpose, that are characterized by different levels of accuracy and costs. This aspect is of great importance when extensive surveys (such as ones involved in seismic micro-zoning studies) are of concern. Due to their cost effectiveness, growing interest exists for the application of passive seismic surveys in microzonation studies and at least one international research project has been devoted to this topic (SESAME project, http://sesame.geopsy.org/). These techniques are based on the analysis of small amplitude ambient vibrations, both of natural and anthropic origin.

In the following Section a summary of all the aforementioned techniques is done; great emphasis is given to seismic noise analysis, especially single station and array analysis. A briefly description of the non-linear behavior of soils is presented, including the techniques used to evaluate them (resonance column and cyclic torsional shear tests), and liquefaction phenomenon.

4.1 Effects of Soft Surface Layers: the Amplification Function

The ground-shaking produced by an earthquake in a given site basically depends on the event magnitude, the source-to-site distance, and the local geologic conditions. When a fault ruptures below the Earth's surface, body waves travel away from the source in all directions. Since the earth's crust is not homogeneous, but it’s composed of a complex mixture of rocks and sediments of several types, as the waves reach the boundaries between different geologic materials, they are reflected and refracted. Near the ground surface, where the density and S-waves velocity are generally lower than in the materials beneath them, multiple refractions produce nearly vertical waves propagation. As mentioned before, one of the fundamental phenomenon responsible for the amplification of the motion in

soft soils is the trapping of seismic waves, attributable to the impedance contrast between sedimentary covers and the underlying more rigid bedrock. The impedance contrast Z is defined as the ratio between density ρ and S-wave velocity β of different geologic materials (for example A and B):

$$Z = \frac{\rho_A \cdot \beta_A}{\rho_B \cdot \beta_B}$$

The analysis of one-dimensional (1D) ground response are based on the assumption that the soil and bedrock surface is extended infinitely in the horizontal direction and that the soil deposit response is predominantly caused by SH-waves vertically propagating from the underlying bedrock (*plane and parallel layers approximation*). Most methods commonly used to compute the response of systems with one-degree of freedom, are based on the use of *transfer functions*. Transfer functions can be used to express several response parameters, such as displacement, velocity, acceleration, from an input motion parameter such as bedrock acceleration.

The bedrock motion (seismic input) can be represented as a Fourier series (Aki, 1980). Each term in the Fourier series of the input is then multiplied by the transfer function to produce the Fourier series of the ground surface motion (output). Thus, the transfer function determines how each frequency in the bedrock motion is amplified, or de-amplified, by the soil deposit. In the hypothesis of a uniform layer of isotropic soil overlying a bedrock, the harmonic horizontal motion of the bedrock will produce shear waves traveling up and down in the surface layer (Figure 4.2).

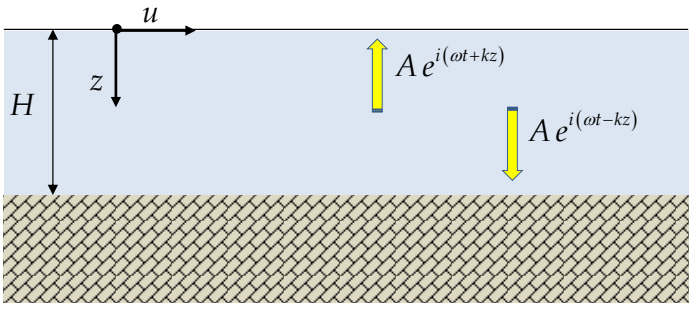

Figure 4.2 Linear elastic soil deposit of thickness H overlying a rigid bedrock.

The resulting horizontal displacement can be expressed as:

$$u(z,t) = A\,e^{i(\omega t+kz)} + B\,e^{i(\omega t-kz)}$$

where ω is the angular frequency of the ground shaking, *k* is the wave number, and *A* and *B* are the amplitudes of the waves traveling in the –z (upward) and +z (downward) directions, respectively. At the free surface ($z=0$), the shear stress, and consequently the shear strain, must vanish, and thus *A* must equal *B*.

The constructive interference of the upward and downward traveling waves produces *standing waves* of amplitude $2A\cos kz$, that have a fixed shape with respect to depth:

$$u(z,t) = 2A\cos(kz)e^{i\omega t}$$

The previous Equation can be used to define a *transfer function* that describes the ratio of the displacement amplitudes at any two points in the soil layer. Choosing these two points to be the top and bottom of the soil layer, the transfer function is given by:

$$F(\omega) = \frac{1}{\cos(\omega H / V_S)}$$

The transfer function is generally a complex quantity. The *amplification function* is the modulus of the transfer function which indicates that the surface displacement is always at least as large as the bedrock displacement and, at certain frequencies, is much larger. Thus is the ratio of the free surface motion amplitude to the bedrock motion amplitude.

As $\omega H / V_S$ approaches $\pi/2 + n\pi$, the denominator of $F(\omega)$ approaches zero, which implies infinite amplification, or *resonance*. Therefore, the response of soft soil is strongly dependent upon the frequency of the base motion, and the frequencies at which great amplification occurs are related to S-wave velocities and the thickness of the soil layer. At frequencies that approach the fundamental frequency of a soil deposit, the transfer function begins to take large values.

For one-layer 1D structures, the fundamental frequency is given by (fundamental)

$$f_0 = \frac{\beta}{4H}$$

The *n*-th natural frequency of the soil deposit is given by:

$$f_n = (2n+1)\cdot f_0$$

where β is the S-wave velocity in the surface layer, H is the thickness, and n is an integer number characterizing the harmonic order.

The period of vibration corresponding to the fundamental frequency is called the *characteristic site period*,

$$T_S = \frac{4H}{\beta}$$

The characteristic site period depends on the thickness (H) and S-wave velocity (β) of the soil. It is a very important parameter because provides a useful indication of the period of vibration at which the most significant amplification can be expected.

It's possible to compute the site amplification using the *quarter-wavelength approximation* described by Boore and Brown (1998). That method estimates the amplification for a specific frequency, by calculating the impedance contrast between near-surface materials at a depth corresponding to a quarter of the wavelength, and using the material properties of the underlying bedrock. The amplitude is also associated to the characteristics of the wavefield (type of waves, angle of incidence, etc.). In the case of waves with vertical incidence, the maximum amplification reduces to:

$$A(f) = \sqrt{\frac{\rho_r \beta_r}{\rho \beta}}$$

In equation ρ_r and β_r are the density and shear-wave velocity averaged from the surface to a depth corresponding to a quarter of the wavelength, and ρ, β are the density and velocity at the reference depth.

The Figure 4.3 represents the amplification function for a single layer of 80 m of thickness ($V_S = 300\ m/s$) overlaying a rigid bedrock ($V_S = 1200\ m/s$):

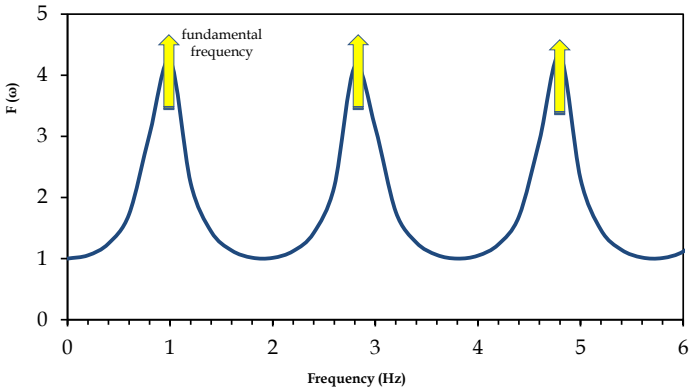

Figure 4.3 Example of amplification function for a single layer overlying a rigid bedrock.

4.2 *Seismic Noise Analysis*

For the majority of seismic prospecting methods, natural ambient vibrations constitute an undesired part of the signal, which has to be eliminated as much as possible. From a general point of view a generic sensor of the surface of the Earth records a great number of seismic phases, as illustrated in Figure 4.4:

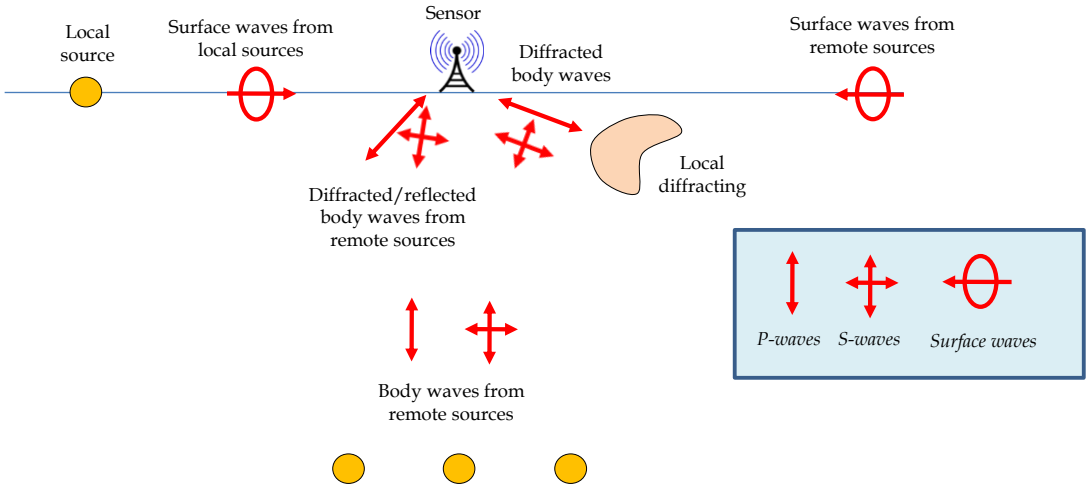

Figure 4.4 Seismic phases recorded by a generic sensor on the surface of the Earth.

Ambient vibrations are deeply studied to get information on both the near-surface geology as well as the inner Earth structure. In fact, the noise field is influenced by the subsurface structure, so it is possible to retrieve their information to derive the main properties of the soil.

In this introduction a summary of the present status of knowledge will be illustrated as far as those aspects necessary for this Thesis is concerned. For further insights see Bonnefoy-Claudet et al. (2004, 2006) and references therein; SESAME deliverable D13.08 for a comprehensive review, http://sesame-fp5.obs.ujf-grenoble.fr/SES_TechnicalDoc.htm, for a detailed discussion.

Understanding the physical nature and composition of the ambient seismic noise wavefield, especially in urban areas, is a very difficult problem. This review outlines that, while an overall agreement is reached concerning the origin and main characteristics of seismic noise, this is not the case for the composition of seismic noise wavefield, mainly because of the lack or scarcity of data. It seems well established now that the spatial and temporal characteristics of seismic noise are closely related with its natural or cultural origin: a basic classification can be made into low frequency *microseisms* or higher frequency *microtremors*,

respectively. The amplitude variations of microseisms are well correlated with oceanic and large-scale meteorological conditions; in contrast, the daily and weekly variations of microtremors amplitude are clearly correlated with human activities (machineries, traffic, etc.). The boundary between these two types of noise is close to 1 Hz, but may vary from site to site depending on the soil structure – and, may be, on the characteristics of human activity. More advanced investigations have to be carried out to precisely identify a site-specific frequency limit between microseisms and microtremors. For example, continuous seismic noise measurement should be performed in different urban areas presenting different soil fundamental resonance frequencies (i.e., lower than, equal to and higher than 1 Hz) and lead to a better definition of the role of noise sources and soil geology in noise spectral amplification.

Concerning the composition of the seismic noise wavefield, this overview also highlights the scarcity and variability of relevant data which results in the absence of any scientific consensus. It would be however of particular interest for array and H/VRS techniques to have reliable estimates of the average proportion of energy carried by Rayleigh waves, and more especially by the fundamental mode, in a given seismic noise recording. This is not possible today, nor even to determine whether it is legitimate to look for such average value. This variability may be due to differences from site to site (soil characteristics and/or source properties) as much as to methodological biases and/or author interpretation issues. Moreover this review outlines that in general higher modes of Rayleigh waves may exist in the noise wavefield at high frequency. Seismic noise based methods need to take this observation into account in order to reach the right interpretation, since, for instance, the interpretation of second or higher peaks observed on H/VSR curves may depend on the noise wavefield composition (body waves resonance or higher mode of Rayleigh waves). Until now this is still an open question. Following the literature studies of Bonnefoy et al. (2004) it has been shown the relative proportion of Love waves contained in the seismic noise is significant (at least 40%, probably higher than 50% in most cases). This result is important in view of the recent attempts to invert H/VSR curves interpreted as a proxy to ellipticity curves, and there is a clear need to use and/or develop array methods and inversion schemes able to take it into account. This study also provides indications as to possible ways to investigate the composition of seismic ambient noise wavefield.

It is worth however to conclude by emphasizing several facts: the hidden (or implicit) assumption according which seismic noise wavefield would consist only in pure fundamental mode Rayleigh waves (for the vertical component) is not supported by the data. The proportion of different waves (body/surface waves, Rayleigh/Love, fundamental/higher modes) is dependent on site conditions and source properties. However whatever the predominant type of waves, H/VSR curves always indicate the resonance frequency (Bonnefoy- Claudet, 2004; Bonnefoy-Claudet et al., 2006), at least for 1D structures with large enough impedance contrast.

	Natural	*Human*
Name	*microseism*	*Microtremor*
Origin	ocean	Traffic/Industry/Human activity
Frequency	0.1- f_{nh} (0.5 – 1 Hz)	f_{nh} (0.5 1 Hz) ? 10Hz
Incident wave-field	Surface waves	Surface + body waves
Amplitude Variability	Related to Ocean storms Incident wave-field	Day-night, week-week-end Comparable amplitude
Rayleigh/Love	predominantly Rayleigh	Slight indication that Love waves carry a little more energy
Fundamental –Higher Modes	Mainly fundamental	Possibly of higher modes at higher frequencies
Comments	Local wave-field may be different from incident wave-field	Some monochromatic waves related to machines and engines

Table 4.1 Remarks summarizing the status of the art concerning the present knowledge on the nature and composition of the noise field (from D23.12 WP12 of the SESAME project).

Because the main objective of this Thesis concerns studies related to site effects, a particular attention is paid to microtremor. In fact, studying site effects concerns the ability of a site to amplify the seismic wavefield in the range of frequencies between 0.5 – 15 Hz, i. e. frequencies potentially able to damage human buildings.

4.2.1 Single Station Measurements

The *H/V spectral ratio method*, also known as *Nakamura method* is an experimental technique to evaluate some characteristics of soft-sedimentary (soil) deposits. The technique originally proposed by Nogoshi and Igarashi (1971), based on the initial studies of Kanay and Tanaka (1961) and wide-spread by Nakamura (1989, 2000), consists in estimating the ratio between the Fourier amplitude spectra of the horizontal (H) to vertical (V) components of the ambient noise vibrations recorded at one single station. Due to its low-cost both for the survey and analysis, the H/V technique has been frequently adopted in seismic microzonation investigations. However, it should be pointed out that the H/V technique alone is not sufficient to characterize the complexity of site effects and in particular the absolute values of seismic amplification. The method has proven to be useful to estimate the *fundamental resonance frequency* of soil deposits given by the following formula:

$$f_0 = \frac{\langle \beta \rangle}{4 \cdot H}$$

where $\langle \beta \rangle$ is the average shear–wave velocity, and H is the thickness of an equivalent dynamic layer corresponding to the maximum seismic impedance contrast. If considering higher modes the precedent formula becomes:

$$f_n = (2n-1)\frac{\langle \beta \rangle}{4 \cdot H}$$

However, measurements and the analysis should be performed with caution. The main recommended application of the H/V technique in microzonation studies is to map the fundamental frequency of the site and help constrain the geological and geotechnical models used for numerical computations. In addition, this technique is also useful in calibrating site response studies at specific locations.

The computation of the H/V ratio follows different steps:

- record a 3-component ambient noise signal
- select of the most stationary time windows (e.g., using an anti-triggering algorithm) in order to avoid transient noise
- compute and smoothing of the Fourier amplitude spectra for each time windows
- Average the two horizontal component (using a quadractic mean)

- compute the H/V ratio for each window
- compute the average H/V ratio

The steps described above are illustrated in the next Figure:

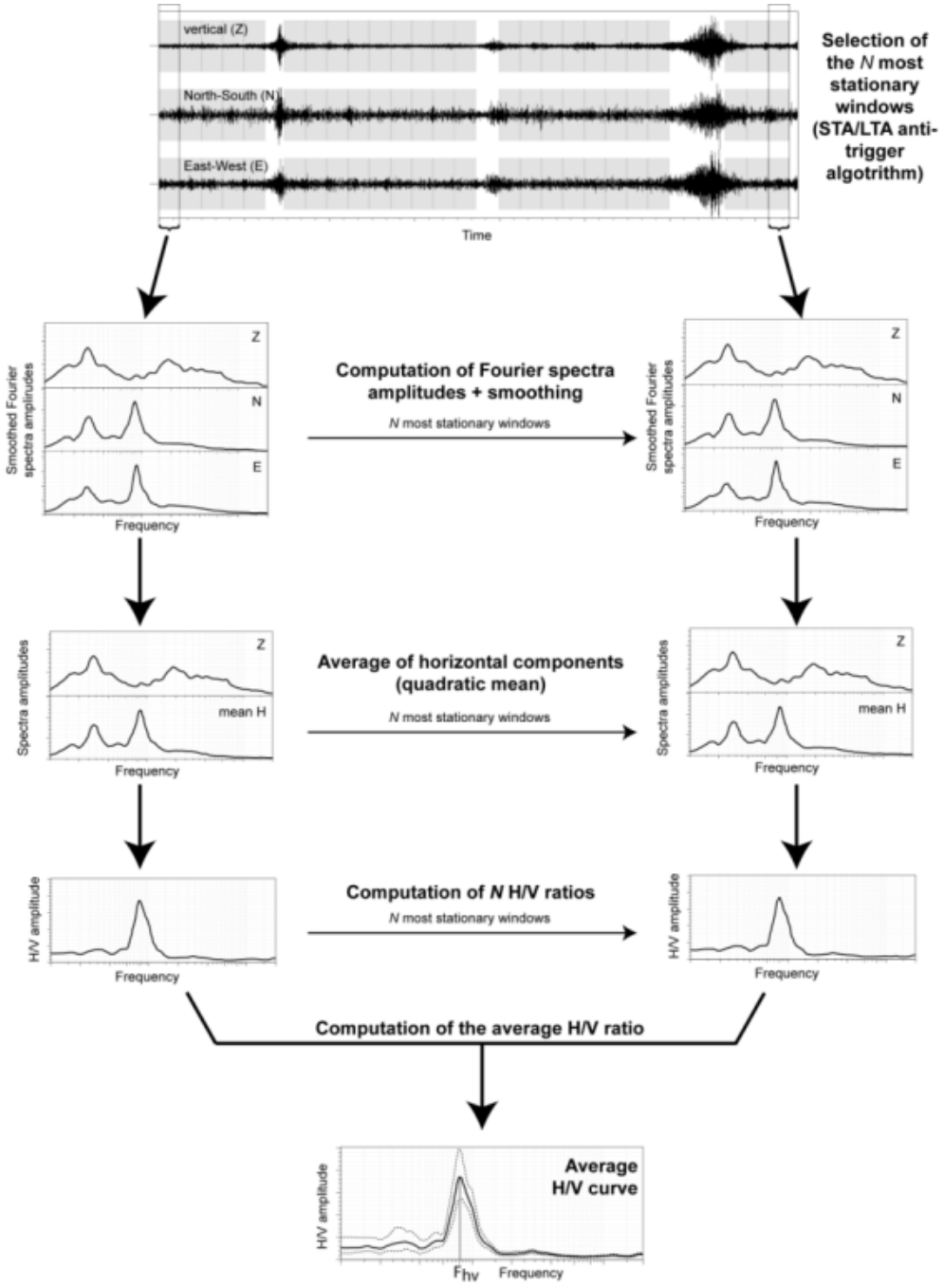

Figure 4.5 Description of the computation of the H/V (from GEOPSY.ORG).

4.2.1.1 H/V Spectral Ratio and Body Waves

As site amplifications occurring during actual earthquakes essentially involve incoming body waves, it is obvious that the horizontal and vertical components of body waves are both highly sensitive to site conditions. The main question to remark here is the relation of the H/V ratio and site conditions for body waves; a side question concerns the differences or similarities between H/V ratios derived from earthquake recordings and H/V ratios derived from ambient vibration recordings.

When considering, once again, a simple horizontally layered structure with one soft layer over a half-space, and its response to obliquely incident plane waves, a striking result is the fact that, whatever the incident wave type (P or SV or SH), the horizontal components systematically exhibit resonant peaks at the S-wave resonance frequencies (even for P wave incidence), while the vertical component always exhibits resonant peaks at the P-wave resonance frequencies (even for S wave incidence). This result is valid when the impedance contrast is large both for S and P waves, and comes from the conversion from P and SV waves at the bedrock/layer interface, and their relatively small incidence angles within the surface lower velocity layer.

This fact has very interesting consequences for the fundamental mode, since the S-wave fundamental frequency is always significantly smaller than the P-wave fundamental frequency (ratio equal to the S-P velocity ratio within the surface layer):

- As the fundamental frequency is only weakly dependent on subsurface topography - for usual configurations-, this explain why the H/V ratio for a body wavefield should always exhibit peak around the fundamental S-wave frequency, for high impedance contrast sites.
- In the case of horizontally stratified media, the H/V ratio should also exhibit peaks at the S-wave harmonics, at least for all peaks that do not coincide with a lower order harmonic of P-wave resonance.
- Finally, again for high impedance contrast, horizontally stratified media, the amplitude of the first H/V peak is also expected to be somewhat correlated with the S wave amplification.

These latter two items constitute the main differences from the surface wave case, where it is not generally expected to have eithers harmonics, or any correlation between H/V peak amplitude and actual amplification values. The presence or absence of harmonics at least for a large impedance contrast, 1D structure, may thus be a good indicator of the composition of the wavefield.

One should remain very cautious however in interpreting H/V ratios derived from earthquake recordings beyond the fundamental S frequency, since this ratio is highly influenced by the amplification of the vertical component, which cannot be neglected, especially in sites with pronounced subsurface topography.

4.2.1.2 H/V Spectral Ratio and Ellipticity

As mentioned in Section 3 Rayleigh waves are characterized by an elliptical particle motion in the radial plane, and their phase velocity. In horizontally stratified media where velocity varies with depth, both characteristics exhibit frequency dependence. Stratification also gives rise to the existence of distinct Rayleigh waves mode: while the fundamental mode exists at all frequencies, higher modes appear only beyond some cut-off frequencies, the values of which increases with the mode order. The H/V ratio of all modes of Rayleigh waves, which is a measure of the ellipticity, exhibits therefore a frequency dependence in stratified media

There exist a rich literature on that topic, a list of which may be found in Bard (1998), Malischewsky and Scherbaum (2004) and Bonnefoy-Claudet (2004). The main relevant results may be summarized as follows, considering first simple one layer over half-space structures:

- For intermediate to high S-wave impedance contrasts (i.e., larger than about 3), the H/V ellipticity ratios of Rayleigh waves exhibit infinite peaks and/or zeros corresponding to the vanishing of the vertical (respectively horizontal) component, and inversion of rotation sense (from retrograde to prograde, or inversely). For low contrasts, because of the rotation sense does not change with frequency, the ellipticity ratio only exhibits maxima at some frequencies and minima at other frequencies with no zeroes or infinities.

- Focusing first on the fundamental mode, the vanishing of the vertical component occurs at a frequency Fr which is very close (i.e., less than 5% different) to the fundamental resonance frequency for S waves only if the S-wave impedance contrast exceed a value of 4. For intermediate velocity contrasts (2.6 to 4), the ellipticity peak is still infinite and occurs at a frequency that may be up to 50% higher than the S-wave fundamental resonance frequency. For lower impedance contrast, the infinite peak is replaced by a broad maximum that has only low amplitude (less than 2-3), and occurs at a frequency that may range between 0.5 to 1.5 times the S-wave fundamental resonance frequency.

- The ellipticity ratio H/V of the fundamental mode may also exhibit not only a peak at Fr, but also a minimum (zero) at higher frequency Fz, corresponding to the vanishing of the horizontal components, and a second rotation sense inversion (from prograde to retrograde). A few studies have been performed to investigate the variability of the ratio Fz/Fr; while Konno and Ohmachi (1998) report a value of 2 for a limited set velocity profiles, Stephenson (2003) concludes that peak/trough structures with a frequency ratio around 2 witness both a high Poisson ratio in the surface soil, and a high impedance contrast to the substrate. Some other studies for more complex velocity profiles report a dependence of the ratio on the velocity gradient in the soft sediments.

- Higher modes exhibit also H/V peaks at higher frequencies corresponding to a vanishing vertical component; some of these peaks, especially for high contrasts structures, coincide with the higher harmonics of S-wave resonance. However, for single layer structures, no case is known, for which all existing Rayleigh wave modes exhibit simultaneously a peak at the same frequency. In other words, for all frequencies for which several modes exist simultaneously (i.e., generally beyond the S-wave fundamental frequency), there always exist one Rayleigh wave mode (often the fundamental one) which may carry some energy on vertical component.

- These results may generally be extrapolated to more complex horizontally layered structures involving several layers or velocity gradients; one major difference however concerns the third item and the number of ellipticity peaks. Some sites may present a large velocity contrast (i.e., exceeding 2.5)

at different depths Zk (however, given the minimum threshold of 2.5, the number of such depths rarely exceeds 2...). In such case, the S-wave response will exhibit major amplifications at frequencies Fk corresponding to the fundamental frequencies of the layering located above theses depths with major discontinuity. In such cases, the available results show that all Rayleigh wave modes existing at frequency Fk do exhibit a common ellipticity peak (in other words, the vertical component of all existing Rayleigh wave modes vanish at frequencies Fk). In such sites, a H/V curve with several peaks is therefore consistent with the surface waves interpretation. An example of this situation is a shallow very soft layer resting on a thick, stiff unit underlain by very hard bedrock.

- No relation could be established between the S-wave amplification at the resonance frequency, and the characteristics of the H/V infinite peak (for instance its width) or maximum amplitude.

4.2.1.3 H/V Spectral Ratio and Love Waves

Love waves carry energy only on horizontal component. Their influence on the frequency dependence of the H/V ratio can therefore come only from the frequency dependence of the horizontal component. Different studies (see for instance Konno and Ohmachi (1998)), have shown that, at least for high impedance contrast cases, Love waves do strengthen the H/V peak: all surface waves carry their maximum energy for frequencies corresponding to group velocity minima (Airy phase). For high impedance contrast layering, the group velocity minimum of the fundamental Love mode occurs, like the vanishing of the Rayleigh vertical component, at a frequency Fl which is very close to the fundamental S-wave resonance frequency.

Higher modes of Love waves may also have group velocity minima and associated Airy phase at higher frequencies: this may result in other maxima if higher modes carry a significant amount of energy.

4.2.1.4 H/V Spectral Ratio and Complex Wavefield: Results from Numerical Simulation

Since the actual composition of the seismic noise wavefield is mostly unknown, a series of numerical simulations have been performed to investigate the origin of an H/V peak. A wide variety of subsurface structures have been studied (1D, 2D and 3D), but only 'local' sources have been considered (i.e., less than 10km away from the receiver): the 'microseism' case has not yet been investigated (incoming crustal surface waves generated by oceanic waves). These comprehensive analyses are presented and discussed in various reports (SESAME deliverables D12.09 and D17.10, Bonnefoy-Claudet (2004), Bonnefoy-Claudet et al. (2006)), and only the main conclusions are summarized below:

- For 1D structures, a single H/V peak is obtained only when the predominant noise sources are located within the surface layer and within limited distances from the sites (less than around 20-30 times the layer thickness); the wavefield then consists of a mixture of Rayleigh, Love and body waves. For more distant predominant noise sources (a case not often met in urban sites, but possible in the countryside), and/or deep sources (i.e., located at depth below the interface associated with the main impedance contrast), the wavefield includes a large proportion of body or head waves, especially at high frequencies, and H/V exhibit several peaks associated with fundamental and harmonics of S-wave resonance. In all cases, the frequency of the H/V peak exhibits a very good agreement (within +/- 20% at most) with the actual fundamental S-wave frequency of the layered structure.

- For laterally varying structures, the wavefield associated with 'local' noise sources is more complex, since it also includes additional waves diffracted from the lateral heterogeneities. the composition of this diffracted wavefield depends on the location of the site of interest with respect to the lateral heterogeneities: away from them (for instance, in the flat central parts of valleys and basins), it mainly consists of surface waves (fundamental or higher mode depending on the frequency); close to them is also includes a significant portion of body waves. For all the investigated simulation cases (all with a large impedance contrast), H/V curves exhibit clear (sharp) peaks in the 'flat' parts (i.e., those with only gentle

underground interface slopes), and broader and generally lower maxima at sites with rapidly varying thickness (for instance valley edges).

All the above discussion and results implicitly addressed mainly sedimentary/alluvial sites within valleys or plains, and are therefore valid only for horizontal free surfaces. As frequency dependent site amplification has been repeatedly observed also on top of rocky hills, several attempts have been performed to investigate whether H/V ratios from ambient vibrations also exhibit a peak in the same frequency range. These attempts have generally been successful, but no theoretical interpretation and no numerical simulation have been proposed to explain this apparent success.

4.2.2 Array Analysis

A *seismic array* is a spatially distributed set of seismological sensors (geophones, seismometers, accelerometers) sufficiently close to each other in space recording with a common time base. Obviously we can talk about 1-D or 2-D array if the sensors are dislocated on a plane or along a specific direction, respectively.

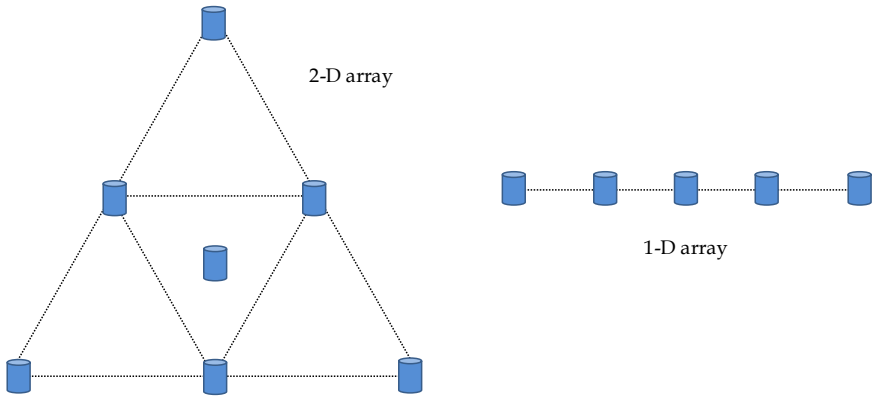

Figure 4.6 Two generic seismic arrays: on left, 2D array, on right 1D array.

Recording ambient vibrations with a seismic array is an attractive tool for in situ measurements of shear wave velocity (V_S) (Asten and Henstridge, 1984, Goldstein and Archuleta, 1987). This success among scientists comes from the easiness to use passive sources as well as possibility of investigating deep sedimentary structures at a very low cost if compared to classical geological surveys (such as cross-hole and down-hole techniques). Good references for techniques using arrays are explained in Johnson and Dudgeon.

4.2.2.1 *The frequency-wavenumber Power Spectrum (f-k Spectrum)*

Consider an array of N sensors at positions $\vec{r}_n$, $(n=1,\ldots N)$ recording a set of q, $q<N$ uncorrelated plane waves $s_j(t)$, $j=1,\ldots,q$ propagating in a homogeneous medium.

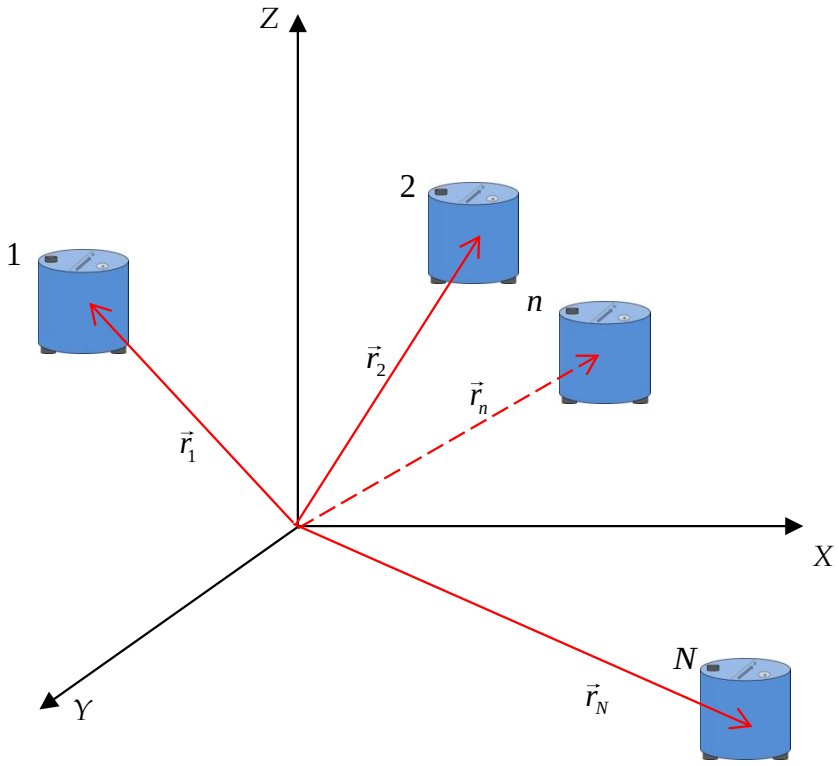

Figure 4.7 Geometry of a general seismic array.

The time signal $x(t)$ recorded at n station ay position $\vec{r}_n$ is obtained by the superposition of the individual plane waves:

$$x(\vec{r}_n,t)=\sum_{j=1}^{q} s_j\left(t-\tau_j\right)+\eta(\vec{r}_n,t),$$

where τ_j is the time delay for each sensor respect to the arrival time of a reference sensor, and $\eta(\vec{r}_n,t)$ stands for the uncorrelated part of the wavefield. In the domain of the frequency the previous Equation can be written as:

$$X(\vec{r}_n,\omega)=\sum_{j=1}^{q} S_j(\omega)e^{j(\omega\tau_j)}+\eta(\vec{r}_n,\omega),$$

where $\omega=2\pi f$ is the angular frequency. For a plane wave we can write $\omega\tau_j=\vec{k}_j\vec{r}_n$, where $\vec{k}_j$ represent the wave-number of the plane wave s_j.

The array output is defined as a multi-channel delay and sum filter operation, written in the domain of the time as:

$$y(t) = \sum_{n=1}^{N} w_n(t)\, x(\vec{r}_n, t - \tau_n)$$

where $\omega\tau_n = \vec{k}_j \vec{r}_n$.

Combining the two previous Equations, and writing the delay times as function of wavenumber $\vec{k}$, the output of the array in the domain of frequency-wavenumber can be expressed as:

$$Y(\vec{k},\omega) = \sum_{n=1}^{N}\sum_{j=1}^{q} W_n(\omega) S_j(\omega) e^{i(\vec{k}_j - \vec{k})\vec{r}_n} + \sum_{n=1}^{N} \eta(\vec{r}_n, \omega)$$

An estimate of the wave propagation parameters $(\vec{k},\omega)$ is thus obtained by maximizing the modulus $Y(\vec{k},\omega)$ within the frequency-wavenumber plane, that is $\vec{k}_j - \vec{k} = 0$.

The cross-spectrum of the recorded signals in frequency-wavenumber domain, usually called the *f-k cross-spectrum*, is defined as:

$$P(\vec{k},\omega) = \sum_{\ell=1}^{N}\sum_{n=1}^{N}\sum_{j=1}^{q} W_n(\omega) W_\ell(\omega) S_{jn}(\omega) S_{j\ell}^{*}(\omega) e^{i(\vec{k}_j - \vec{k})(\vec{r}_n - \vec{r}_\ell)} + \sum_{\ell=1}^{N}\sum_{n=1}^{N} \eta(\vec{r}_n,\omega)\eta^{*}(\vec{r}_\ell,\omega)$$

where $S_{jn}(\omega)$, $S_{j\ell}(\omega)$ denote the Fourier spectra of the wave s_j at receivers $\vec{r}_n$ and $\vec{r}_\ell$ and * symbolizes the conjugate complex.

Letting $S_{jn}(\omega) = S_{j\ell}(\omega) = 1$ and neglecting the uncorrelated noise, one can define the normalized beam-pattern $B(\vec{k},\omega)$ of the array for a single wave plane incident from below by setting $\vec{k}_j = 0$ in the previous:

$$B(\vec{k},\omega) = \frac{1}{N^2} \sum_{\ell=1}^{N}\sum_{n=1}^{N} W_n(\omega)\, W_\ell(\omega) e^{i\vec{k}(\vec{r}_n - \vec{r}_\ell)}$$

In matrix notation, the previous Equation can be rewritten as:

$$\underline{Y} = \underline{A}\underline{W}\underline{X}$$

where

$$\underline{W} = \begin{bmatrix} W_1(\omega) & 0 & \ddots & 0 \\ 0 & W_2(\omega) & 0 & \ddots \\ \ddots & 0 & \ddots & \ddots \\ 0 & \ddots & \ddots & W_N(\omega) \end{bmatrix}$$

$$\underline{A} = \left[e^{-i\vec{k}\vec{r}_1}, e^{-i\vec{k}\vec{r}_2}, \ldots, e^{-i\vec{k}\vec{r}_N} \right]$$

$$\underline{X} = \left[X_1(\omega), X_2(\omega), \ldots X_n(\omega) \right]^{\mathrm{T}}$$

The frequency-wavenumber (*f-k*) cross-spectrum expressed in Matrix notation is then:

$$\underline{P} = \underline{A}\underline{W}\underline{R}\underline{W}^H\underline{A}^H$$

where $\underline{R} = E\left\{\underline{X}\underline{X}^H\right\}$ is the $N \times N$ *cross spectral matrix* (*CSM*) and ^{H} denote the Hermitian conjugate operator. The cross spectral matrix is evaluated using frequency or spatial smoothing.

The CSM matrix is the root of any *f-k* based array technique: the CSM carries indeed all the information about the propagation parameters of the waves propagating across the array; $\underline{W}$ is composed of the filter weights that can be designed in order to minimize the energy leakage from regions outside the actual signal wavenumber and $\underline{A}$ is the steering vector that is used for sweeping the wavenumber domain.

In practice one seeks the maxima of the CSM by performing a grid search in the wavenumber domain for a frequency *f* of interest. From the wavenumbers $\vec{k}_n$ of local maxima in wavenumber map, the direction θ_n and the apparent velocity $c_n(\omega)$ (or slowness $s_n(\omega)$) can be determinate by:

$$\theta_n = \tan^{-1}\left(\frac{k_x}{k_y}\right)_n, \quad \text{and} \quad c_n(\omega) = \frac{\omega}{\left|\vec{k}_n\right|}$$

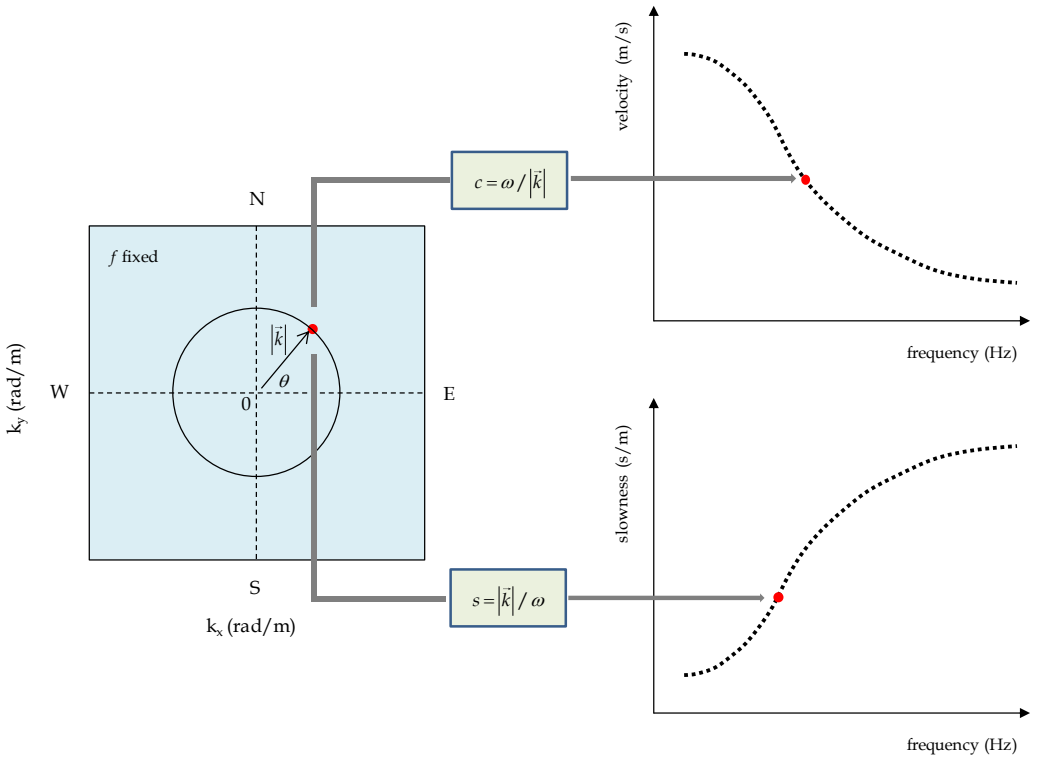

Figure 4.8 Contouring of the coherence estimator function in the plane (k_x, k_y) (grid search map), at fixed frequency ω. Red spot is the relative maximum of the power spectrum estimator (from Tokimatsu, 1995).

4.2.2.2 *Conventional f-k Analysis (CVFK)*

For the conventional f-k analysis (CVFK) the weighting functions are set to $W_n(\omega) = 1$ and thus the f-k density cross-spectrum reduces to

$$P(\vec{k}, \omega) = \sum_{\ell=1}^{N}\sum_{n=1}^{N}\sum_{j=1}^{q} S_{jn}(\omega) S_{j\ell}^{*}(\omega) e^{i(\vec{k}_j - \vec{k})(\vec{r}_n - \vec{r}_\ell)} + \sum_{\ell=1}^{N}\sum_{n=1}^{N} \eta_\ell^H(\vec{r}_i, \omega)\eta_n(\vec{r}_i, \omega).$$

The conventional estimator is then written in matrix notation

$$\underline{P}_{CV} = \underline{A}\underline{R}\underline{A}^H$$

Since the weightings are constants, the performance of the CVFK analysis is completely governed by the shape of the array beampattern at a given frequency, i.e. mainly by the array geometry. The array performance is restricted to the following wavenumber range $|\vec{k}| \in [2\pi / D_{\max}, 2\pi / D_{\min}]$, where $D_{\max}$ is the aperture of the array and $D_{\min}$ is the minimum distance between two neighboring sensors. $2\pi / D_{\max}$ is the Rayleigh limit of the array that defines the capability of

the array to resolve two waves propagating at close wavenumbers and $2\pi / D_{\min}$ is the Nyquist wavenumber.

4.2.2.3 Capon's Analysis (HRFK)

Capon (1969) modified the weighting functions $W_n(\omega)$ in order to minimize the f-k cross-spectrum energy carried by wavenumbers differing from the true signal wavenumber. Expressed in other words, $W_n(\omega)$ are optimized by minimizing the signal power $\underline{W}\underline{R}\underline{W}^H$ except at the actual wavenumber. This last constraint is such as the array output at a given receiver is identical to the signal actually recorded at this sensor location:

$$Y_n(\omega) = W_n(\omega) X(\vec{r}_n, \omega) e^{-i\vec{k}\vec{r}_n} = X(\vec{r}_n, \omega)$$

Resulting into the constraint

$$W_n(\omega) e^{-i\vec{k}\vec{r}_n} = \underline{W}\underline{A} = 1$$

Minimizing the expression $\underline{W}\underline{R}\underline{W}^H$ under the constraint $\underline{W}\underline{A}^H$ is performed using the Lagrangian operator and leads to (Capon, 1969)

$$\underline{W} = \frac{\underline{R}^{-1}\underline{A}}{\underline{A}^H \underline{R}^{-1} \underline{A}}$$

The "Capon estimator" is then

$$\underline{P}_{\text{Capon}} = \frac{1}{\underline{A}^H \underline{R}^{-1} \underline{A}}$$

The Capon estimator allows a higher angular resolution than the conventional estimator and the Rayleigh limit of the array is pushed away to lower wavenumber values allowing thus the characterization of waves propagating at close wavenumbers.

The f-k algorithm has been implemented in C++ by Marc Wathelet (2005) as a plug-in module of the seismic signal database GEOPSY2. The Fourier transform is calculated with the FFTW package (Frigo and Steven, 2005) which allows any arbitrary number of samples, not restricted to powers of two.

4.2.2.4 Array Geometry, Resolution and Aliasing

An important issue in any array measurement is the question of optimal geometry (size, shape, number of sensors, etc.) regarding the resolution limits and spatial aliasing effects. This topic has been treated both for large aperture arrays in the context of earthquake/explosion monitoring (Haubrich 1968) as well as in the field of small aperture array for ambient vibration processing (Woods and Lintz (1973); Asten and Henstridge (1984); Kind (2002)). The main differences between these different fields of application can be attributed to the signal components of interest that are to be analyzed. Whereas in the field of earthquake detection, arrays are usually optimized for undispersed broadband transient signal arrivals (body wave detection) from relatively distant sources (plane wave-front), for ambient vibration surveys we have to consider a mostly random wave-field caused by nearby superficial sources which has to be analyzed within narrow frequency bands.

Due to the aim of investigation, i.e., the determination of frequency dependent phase velocity curves, array methods have to be employed for a narrowband analysis of the ambient vibration wave-field. Compared to broadband processing, the resolution of narrowband array responses is significantly reduced and aliasing peaks are fully developed (Kind, 2002); SESAME deliverable no. D24 Wp13 http://sesame-fp5.obs.ujf-grenoble.- fr/SES TechnicalDoc.htm).

Unfortunately, the use of broader frequency bands is prohibitive for the determination of dispersion characteristics (Wathelet et al., 2008). Thus, an enhancement of the resolution/aliasing capabilities for narrowband analysis can only be achieved by improving the spatial sampling of the wavefield. In turn, this requires the use of a large number of stations in field experiments. Clearly, viewed from the economical perspective, this option is prohibitive in most cases considering the initial equipment cost, the increased logistical effort and additional man power required for field experiments. Given the economical and logistical constraints, there is little one can do with respect to the resolution/aliasing issue for dispersion curves, except choosing an appropriate array size and array geometry, suitable for the analysis of a narrow wavelength range.

Unfortunately, at the present time there is no global agreement about the capabilities of an array designed at recording ambient vibrations. Asten and Henstridge (1984) recommended that the array diameter should be at least as large as the longest wavelength of interest and that the station spacing for any direction

should be less than half the shortest wave-length of interest so as to avoid aliasing in the wave-number domain. Asten and Henstridge (1984) proposed the following relationships between the minimum and maximum sensor spacing (D_{min} and D_{max}) and the minimum and maximum wave-lengths (k_{min} and k_{max}) necessary to achieve reasonable results

$$\begin{cases} \lambda_{\max} = 3D_{\max} \\ \lambda_{\min} = 2D_{\min} \end{cases}$$

First relation comes from active source methods for linear arrays and it allows reasonable results to be obtained for ambient vibration arrays as well Tokimatsu (1995). The second one is derived theoretically from Nyquist wave-number. Considering a penetration of the order of half $k_{\max}$ (Xia et al., 2000) for surface waves, the maximum depth for which Vs can be computed is about 1.5 D_{max}. Accordingly, Satoh et al. (2001) proposed the maximum wave-length to be two to four times the maximum sensor separation. Gaffet (1998) stressed out that the _min limit obtained from the minimum sensor spacing is not well adapted to an irregular array grid, as a minimum of 2 points per wavelength is not guaranteed over the entire array. More recently, Kind et al. (2005) used the common rules of thumb to quantify the low frequency limit of the deduced dispersion curve, and a manual interpretation to identify the aliasing limits. In terms of wavenumber, the dimensions of the array can be expressed as (Scherbaum et al, 2003; Tokimatsu (1995)):

$$\begin{cases} k_{\max} = \dfrac{2\pi}{D_{\min}} \\ k_{\min} = \dfrac{2\pi}{D_{\max}} \end{cases}$$

The dispersion curve obtained from array processing is considered to be reliable within these two boundaries; this holds for every processing technique and defines a limit over which spatial aliasing is very likely to occur. The actual numerical values of $k_{\min}$ and $k_{\max}$ depend not only on the array size but also on its geometry. An estimate can be done, on theoretical ground, using the so called array transfer function or theoretical beam pattern. This is the topic of the next paragraph.

4.2.2.5 Array Transfer Function

The theoretical frequency-wavenumber response of an array is a semblance map that would have been obtained for a single vertically incident plane wave. It is also called *Array Transfer Function* R_{th} (*ATF*), or theoretical beam pattern, because the array output is the convolution of the wavefield and of the theoretical frequency-wavenumber response. Following Woods and Lintz (1973), Asten ed Henstridge (1984), the normalized theoretical array response in the (k_x, k_y) plane is given by:

$$R_{th}\left(k_x,k_y\right)=\frac{1}{n^2}\left|\sum_{i=1}^{n}e^{-j\left(k_x x_i+k_y y_i\right)}\right|^2$$

where n is the number of the sensors and $\left(x_i,y_i\right)$ their coordinates. Supposing a single plane wave crossing the array recorded at sensor *i*:

$$S_i\left(f\right)=A\left(f\right)e^{i\left(x_i k_x^1+y_i k_y^1-2\pi ft+\phi\right)}$$

where $A\left(f\right)$, $\left(k_x^1,k_y^1\right)$ and ϕ are its spectrum amplitude, its wavenumber and its phase, respectively. In this particular case the array output is:

$$\mathrm{R_{th}\left(k_x,k_y,f\right)}=\left|\sum_{i=1}^{n}\mathrm{S_i\left(f\right)e^{-i\left(k_x x_j+k_y y_j\right)}}\right|^2=\mathrm{n^2A^2\left(f\right)R_{th}\left(k_x-k_x^1,k_y-k_y^1\right)}$$

The array output is equal to the theoretical response translated by vector $\left(k_x^1,k_y^1\right)$ and multiplied by the square of the amplitude.

For multiple plane waves travelling across the array, from S^1 to S^m, the array output is

$$\mathrm{R_{th}\left(k_x,k_y,f\right)}=\left|\sum_{i=1}^{n}\left(\sum_{\ell=1}^{m}\mathrm{S_i^{\ell}\left(f\right)}\right)\mathrm{e^{-i\left(k_x x_i+k_y y_i\right)}}\right|^2\le\mathrm{n^2}\sum_{\ell=1}^{m}\mathrm{R^{\ell}\left(k_x,k_y,f\right)}$$

where $\mathrm{R^{\ell}}$ is the array output for the single plane wave ℓ, and $\mathrm{S_i^{\ell}}$ the wave ℓ recorded at the station *i*. In this case, the array output is always lower than the sum of translated theoretical responses, and it cannot be simply interpreted as the summation of the individual shifted theoretical array responses.

From the Equation above, R_{th} always exhibits a central peak the value of which is one ($k_x=k_y=0$) and lateral aliasing peaks the amplitude of which is less than one. Beyond a certain limit which is called the *theoretical aliasing wavenumber*, this pattern is repeated due to the periodic nature of e^{ix}. Below this theoretical limit, R_{th} shows that the position of the highest peak of the array output is directly linked to the apparent velocity and the azimuth of the propagating wave

For a complex wavefield and assuming that all contributing waves are in phase to get equality, aliasing is likely to occur for lower wavenumbers due to the summation of the lateral peaks of R_{th}. Hence, R_{th} is of prime importance to define the potential aliasing limits ($k_{\max}$) of the chosen array geometry. On the other hand, it is obvious that the thinner the central peak is, the more capable is the array to distinguish two waves travelling at close wavenumbers. The resolution limit ($k_{\min}$) is controlled by the width of the central peak. For simple array geometries, for instance a Cartesian grid, $k_{\min}$ and $k_{\max}$ are linked to the minimum and maximum distance between sensors. For usual irregular array geometries, R_{th} is necessary for the definition of objective wavenumber limits.

Following Woods and Lintz (1973), Asten and Henstridge (1984), we define practical rules for the aliasing and resolution limits from R_{th}, setting $k_{\max}$ at the first peak exceeding 0.5 (or -3 dB) and $k_{\min}$ being measured at the mid-height of the central peak. If the aliasing peaks are less than the central peak, and if a single source is acting, $k_{\max}$ does not effectively limit the power of the array. However for multiple sources, even if the aliasing peaks are less than the central peak, the superposition may create artefacts leading to the confusion of aliasing peaks with the main one. If the aliasing peaks are of the same order of magnitude as the main peak, the wavenumber limit is always $k_{\max}/2$. In a safe approach, it is better to limit the valid array output to $k_{\max}/2$ in all cases. As example the theoretical array response is calculated for various array geometries in Figure 4.9.

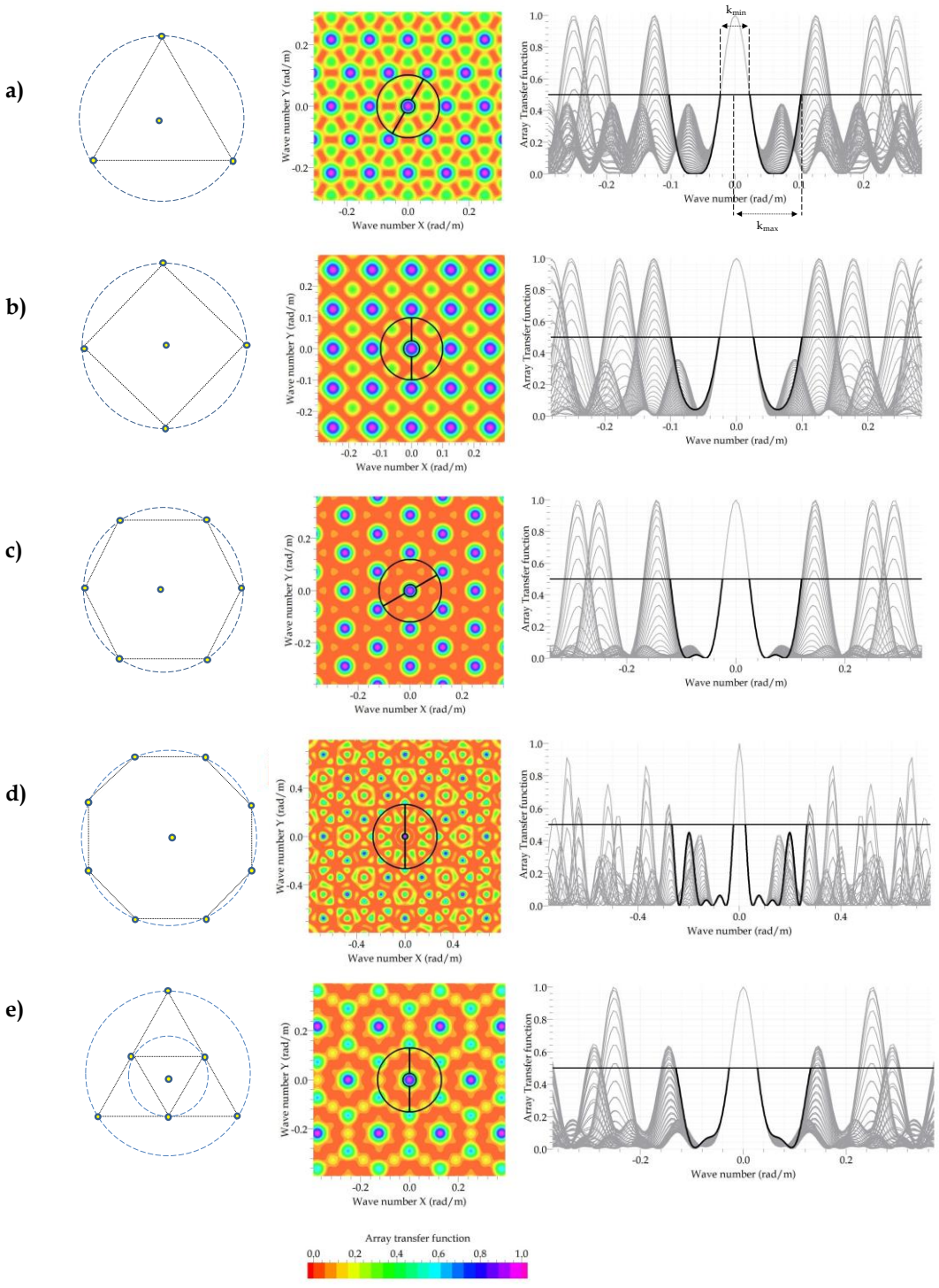

Figure 4.9 ATF for different array geometries. The ATF have been evaluated using WARANGPS in the GEOPSY package (www.geopsy.org).

4.2.2.6 *Multichannel Analysis of Surface Waves (MASW)*

First introduced by Al-Husseini et al. (1981), Mari (1984), Gabriels et al. (1987), the ***M***ultichannel ***A***nalysis of ***S***urface ***W***aves was popularized by Park et al. (1999). This technique relies on the recording along a 1D linear profile of seismic signals produced by a controlled source (hammer, vibrator, explosion, etc.) and analysis of surface wave dispersion properties after applying slant-stack or FK transform to the recorded seismic section. The use of a controlled source generates high-frequency components, so the use of this technique is a useful tool to obtain a detailed description of surface soil layers.

Considering the previous description about seismic noise it is possible to combine different surface waves methods; the aim of this is to obtain a detailed dispersion curve in a broader range of frequencies, as shown in Figure 4.10.

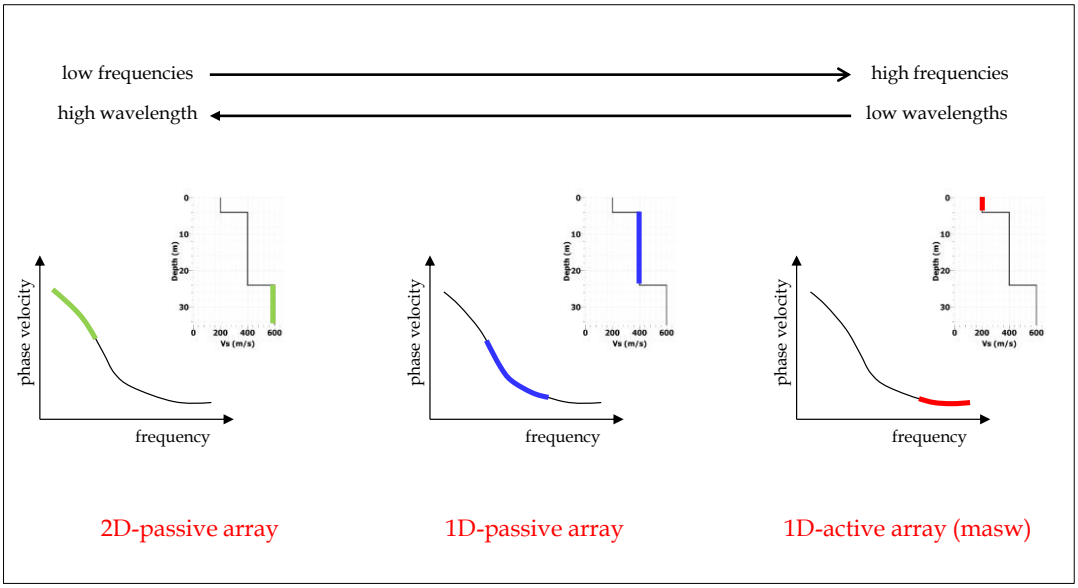

Figure 4.10 Relationships between surface-wave methods techniques and sampled depth.

4.3 *Soil Behavior under Cyclic Stress*

The dynamic behaviour of soils is very important for different problems belonging to the classes of foundation vibrations and earthquake engineering. The need of specific characterization tools has brought to many different procedures for experimental soil mechanics both in laboratory and in situ. The case of soils is particularly complex if compared to other materials because of the inherent characteristic of being a natural material, in comparison to man-made materials. As for many other materials the mechanical behaviour of soil is strongly dependent on the magnitude of strains that are developed for each type of problem. A linear model can be appropriate at very small strains but as deformation increases the behaviour becomes strongly non-linear. Usually many dynamic problems, such as vibrations, imply small strains and this can be really of great help for modelling, since simple models can work quite well. Quite often, to simplify the modelling process in presence of large strains, equivalent linear models are considered. In this case the mechanical properties can be derived by the small strain ones using appropriate *decaying laws*. For dynamic problems, the response of soils to an external perturbation is not only related to its stiffness, but also to its *damping* properties, so that a viscous component is usually introduced to account for dissipation mechanisms.

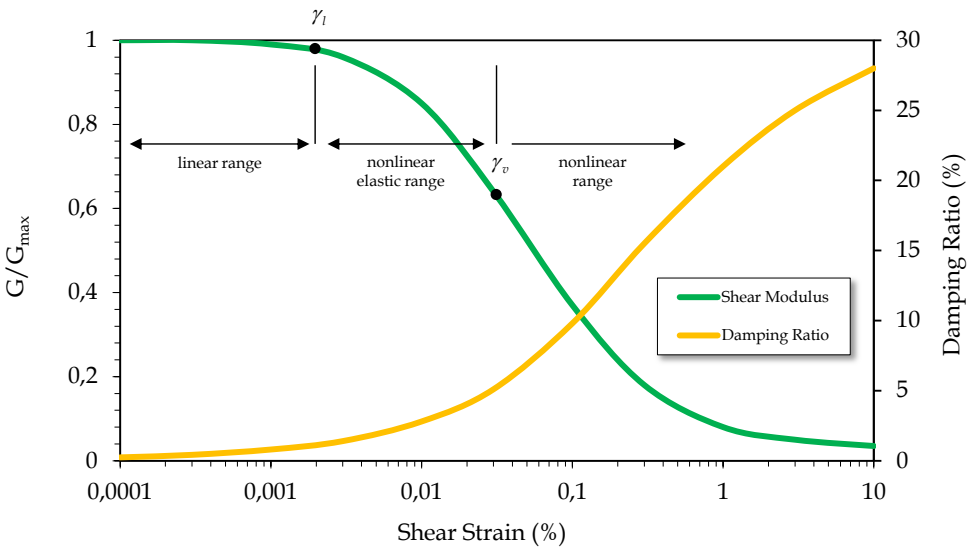

Figure 4.11 Effects of the shear-strain on the soil parameters.

As mentioned before soil behaviour is influenced by many factors. Most of them have been extensively studied using several kinds of laboratory and in situ tests. They can be roughly divided in external factors and specific soil properties. One of the most important external factors is the strain magnitude. The behaviour of soils at different strain levels has been the object of many experimental investigations, especially in laboratory where the testing condition can be fully controlled. Based on these results, some conventional threshold values have been set: they separate strain ranges for which a different phenomenological behaviour can be assigned to the soil. The main interest in this respect is obviously related to the choice of an appropriate model to predict soil behaviour at different strain levels.

For static loads, the soil behaviour can be modelled for increasing strain magnitude respectively as linear elastic, non-linear elastic, non-linear elasto-plastic or perfectly plastic medium (Figure 4.11).

For the description of soil dynamic behaviour, the dissipative phenomena that take place also at very low cyclic shear strains in soils must be taken in consideration. By its definition, an elastic model is not able to describe energy dissipation and hence different models, as for example a visco-elastic one must be used. Some important features of soil behaviour are reported in the following for the different intervals of cyclic shear strains (Vucetic, 1994). For very small shear strains the soil behaves essentially as a linear medium. Usually the associated threshold shear strain is defined with respect to the decay of the shear stiffness modulus G. Indeed, if a secant modulus is defined for each shear strain considering an equivalent linear elastic model, a decaying curve can be obtained for the ratio between the secant modulus and the initial (tangent) one. The *linear threshold strain* γ_l is conventionally defined as the shear strain such that the ratio G / G_0 is equal to 0.95 (Crespellani, 2012). Clearly for this first zone there is no decaying of the stiffness and a linear elastic model would appropriately model the soil response.

Nevertheless it must be noted that energy dissipation take place: in fact hysteretic loops at very small strains for which the area is not null and hence there is dissipation is encountered. Thus a linear-viscoelastic model is more appropriate for cases where energy dissipation is of interest (basically dynamic excitations). The small strain range is comprised between γ_l and the volumetric threshold shear strain γ_v. In this range the stiffness degradation is not very large and the soil behaviour is non-linear, but permanent changes in the microstructure are absent or

negligible. Also in this case an elastic or viscoelastic model, depending on the applications, can give a good approximation of the material response to cyclic loads.

The name volumetric threshold shear strain indicates that above this strain level the permanent change in the soil microstructure under cyclic loads cause a permanent variation of volume in drained conditions or an increase of excess pore water pressure in undrained conditions. Clearly such conditions are far from the ones of elastic models and hence a plastic component need to be introduced, switching to elasto-plastic or visco-elasto-plastic models. Then the degradation of material properties continues up to reach the failure condition, at which level residual values of stiffness are present and the material behaves as perfectly plastic.

The increase of strains produces not only stiffness degradation, but also an increase of the internal disorder in the material and hence an increase of the dissipative properties in terms of *material damping*. This last quantity is defined in relation to the area included in a hysteretic loop as:

$$D(\omega) = \frac{1}{4\pi} \cdot \frac{\Delta W(\omega)}{W(\omega)}$$

For the definition of the above quantities see Figure 4.12:

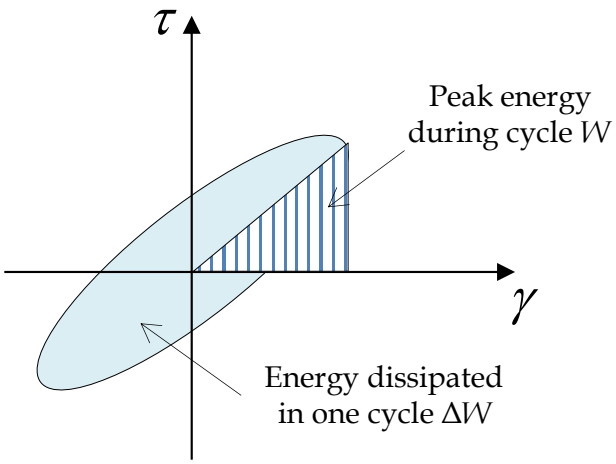

Figure 4.12 Definition of damping ratio from hysteric loop.

Also seismologists use a dimensionless definition of energy dissipation, the *quality factor Q* (Aki and Richards 1980), that is related to the damping ratio by the relationship:

$$Q(\omega) \approx \frac{1}{2D(\omega)}$$

A complete relationship between stiffness and strain, as those shown in Figure 4.11, can be obtained only through laboratory testing. An interesting possibility for modelling soil non-linearity is constituted by the association of a direct measurement of the initial shear stiffness, for example through in situ seismic techniques, and the use of decaying curves to get the equivalent linear parameters for the whole range of strains

One of the critical factor responsible for site effects are the non-linear stress-linear behaviour of soils. Such behaviours can be estimated from in-situ and laboratory tests. Several in-situ test methods are employed to determine the maximum shear modulus G_0 (from the shear wave velocity, *Vs*): Down-Hole (DH) and Cross-Hole (CH) seismic methods, Seismic Dilatometer Test (SDMT) and Seismic Cone Penetration Tests (SCPT), Spectral Analysis of Surface Waves (SASW) and Multichannel Analysis of Surface Waves (MASW). The maximum shear modulus G_0 and the shear stiffness-shear strain (G-γ) degradation curve can be determined using a variety of laboratory testing procedures. In the following Sections two of the most used laboratory tests are briefly described, the resonant column test (RC), and the cyclic torsional test (CTS).

4.3.1 Resonant Column Test (RCT)

In the Resonant Column Test, one of the most used laboratory test, a cylindrical soil specimen is subjected to an imposed ambient stress condition. Once equilibrium at the imposed stress condition is achieved, torsional or longitudinal, or both, sinusoidal vibrations are applied to the soil specimen and the specimen motions (strains) resulting from the imposed vibrations are measured. The frequency of excitation is varied until resonance is achieved. Given the geometry, mass and system parameters, the shear and longitudinal moduli and material (hysteretic) damping may be determined at a measured strain value. The amplitude of vibration is typically varied to measure the variation of moduli and damping as a function of strain. Since the test is usually conducted at strain levels between 0.00001 and 0.5% strain leaving the specimen relatively intact, the test is often conducted at several different sets of ambient stress conditions to measure

the variation of moduli and damping with ambient stress. The test follows the Standard ASTM D 4015-07 (2007).

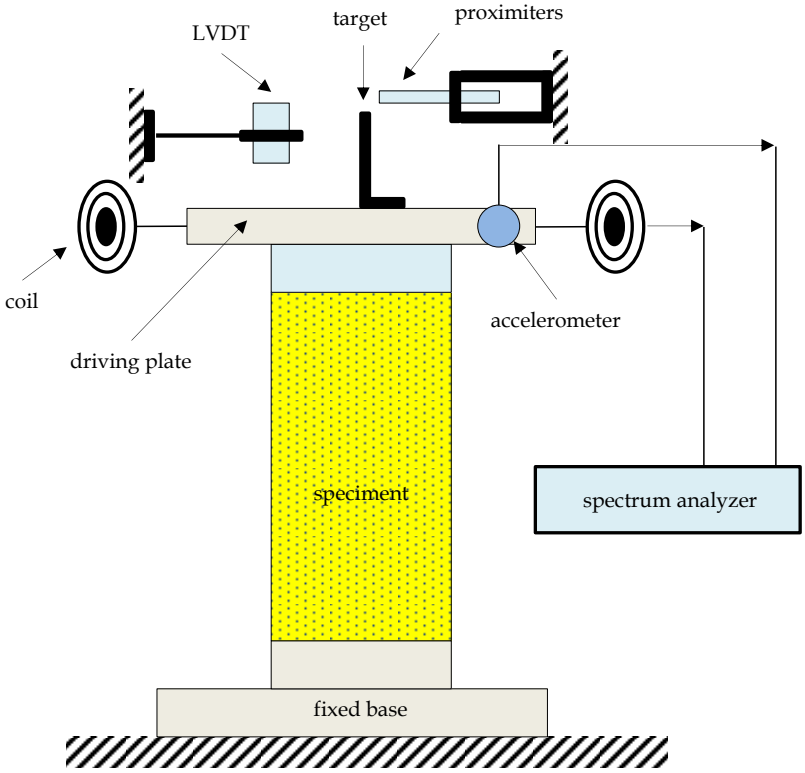

Figure 4.13 Typical instrumentation for low frequency resonant column measurements.

The main purposes of the RC test are:

- Determination of G_0 and D_0 for $\gamma < \gamma_l$;
- Determination of $G(\gamma)$ and $D(\gamma)$ for $\gamma < \gamma_v$;
- Identification of γ_l and γ_v.

The execution of the RC test can be resumed into the following steps:

1. The sample (after saturation) is consolidated;

2. In undrained conditions, a torque of predetermined amplitude is applied to the head of the sample by varying the frequency up to locate one of resonance and determines G. By leaving unchanged the amplitude of the forcing and the frequency, D is determined in conditions of free oscillations or conditions, forced oscillations. Then, the amplitude of the stress is changed and the process is repeated;

3. The test sample is reconsolidated to allow the dissipation the possible excess pore pressure accumulated in the second phase;

4. The sample is again subjected to a series of load cycles (similarly the second phase) to study the effects of pre-straining.

4.3.2 Cyclic Torsional Shear Test (CTS)

For the Cyclic Torsional Shear Test use is made by the same instrumentation for the Resonant Column test (appropriately integrated). The aims of the test are:

- Determination of $G(\gamma)$ and $D(\gamma)$ for $\gamma < \gamma_v$;
- Identification of γ_l and γ_v

It is applied to a cylindrical specimen, bound to the base and free in head, previously saturated and consolidated, a cyclic torque at predetermined frequency, measuring the deformation for different values of solicitation The frequencies used are much lower than the resonance frequencies, and vary generally of between 0.01 and 1Hz (generally the frequency range of seismic input).

The results of the RC and TTC tests are similar and are usually shown in two distinct graphics: in the first one the decay curve of the shear-modulus normalized to its initial value versus shear strain $G/G_0 - \gamma$, and in the other one the damping ratio versus shear strain $D - \gamma$. In the aforementioned graphics it is usually shown also the normalized excess pore water pressure versus shear strain, in order to identify the volumetric threshold γ_v. In the Figure below a typical result for RC test is shown.

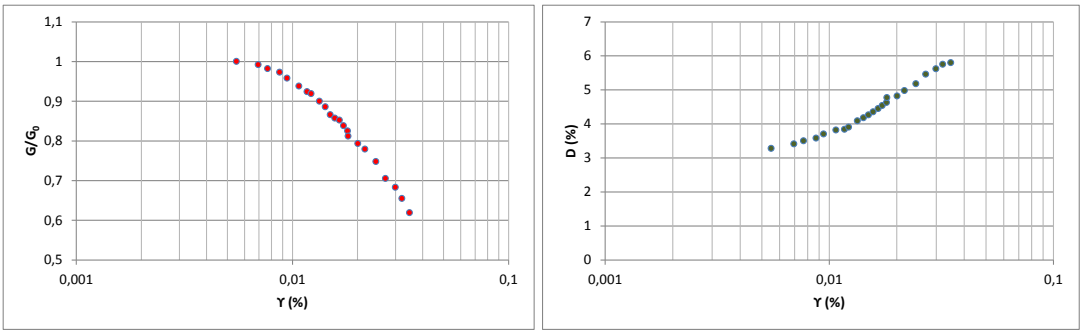

Figure 4.14 Typical results for RC (TTC) tests.

4.4 Soil Liquefaction

Liquefaction is a phenomenon in which the strength and stiffness of a soil is reduced by earthquake shaking or other rapid loading. Liquefaction and related phenomena have been responsible for tremendous amounts of damage in historical earthquakes around the world (Alaska - USA, 1964; Niigata - Japan, 1964; Loma Prieta - USA, 1981; Kobe - Japan, 1995). Liquefaction essentially occurs in saturated soils, that is, soils in which the space between individual particles is completely filled with water. This water exerts a pressure on the soil particles that influences how tightly the particles themselves are pressed together. Prior to an earthquake, the water pressure is relatively low. However, earthquake shaking can cause the water pressure to increase to the point where the soil particles can readily move with respect to each other.

To understand liquefaction, it is important to recognize the conditions that exist in a soil deposit before an earthquake. A soil deposit consists of an assemblage of individual soil particles. Such structure can be described by the Mohr-Coulomb relation:

$$\tau = (\sigma - u)\, tg\varphi$$

where τ and σ are the shear and vertical stresses, respectively, u is the water pressure and φ is the angle of repose.

If we look closely at these particles, we can see that each particle is in contact with a number of neighboring particles (Figure 4.15a). The weight of the overlying soil particles produce contact forces between the particles - these forces hold individual particles in place and give the soil its strength. Liquefaction occurs when the structure of a loose, saturated sand breaks down due to some rapidly or cyclic applied loading (Figure 4.15b). As the structure breaks down, the loosely-packed individual soil particles attempt to move into a denser configuration. In an earthquake, however, there is not enough time for the water in the pores of the soil to be squeezed out. Instead, the water is "trapped" and prevents the soil particles from moving closer together. This is accompanied by an increase in water pressure which reduces the contact forces between the individual soil particles, thereby softening and weakening the soil deposit.

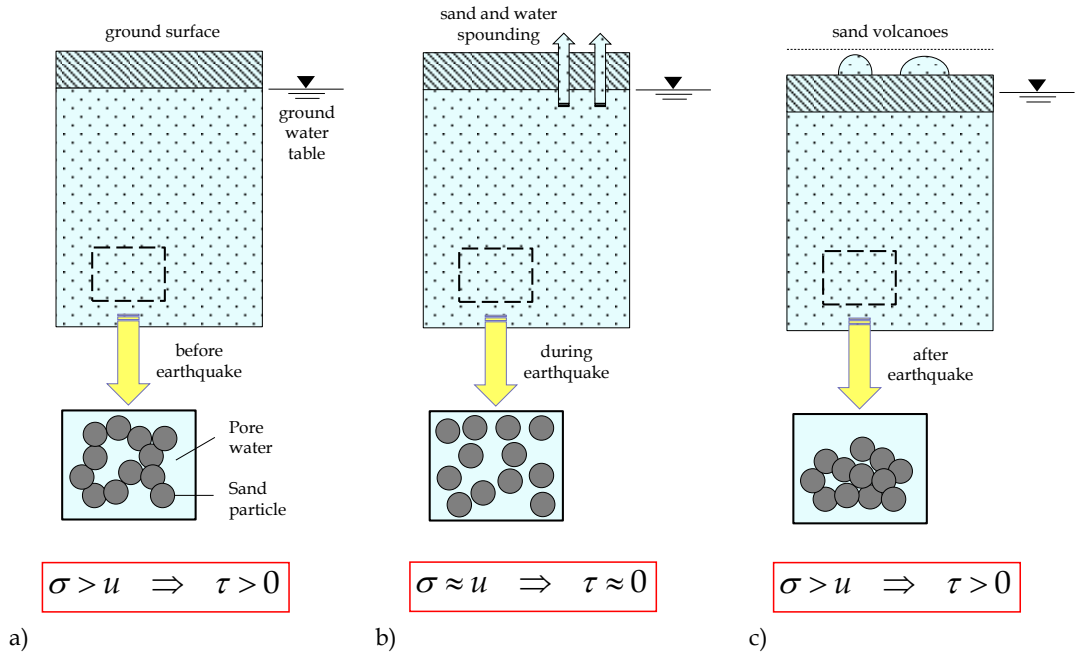

Figure 4.15 Physical behaviour of a saturated soil: a) soil condition before earthquake; b) during earthquake; c) after earthquake.

4.4.1 Testing Liquefaction Risk: Simplified Procedures

Evaluation of the liquefaction resistance of soils is an important step in many geotechnical investigations in earthquake-prone regions. The procedure widely used throughout much of the world for evaluating soil liquefaction resistance is termed the *simplified procedure*. This simplified procedure was originally developed by Seed and Idriss (1971) using blow counts from the Standard Penetration Test (SPT) correlated with a parameter called the *cyclic stress ratio* that represents the cyclic loading on the soil. Since 1971, this procedure has been revised and updated (Seed 1979; Seed and Idriss 1982; Seed et al. 1983, 1985; Youd et al. 1997). In the mid-1980s, a parallel procedure based on the Cone Penetration Test (CPT) was introduced by Robertson and Campanella (1985), which also has been revised and updated (Seed and de Alba 1986; Stark and Olson 1995; Olsen 1997; Robertson and Wride 1998).

A promising alternative, or supplement, to the penetration based approaches is provided by *in situ* measurements of small-strain shear-wave velocity *Vs*. The use of *Vs* as an index of liquefaction resistance is soundly based because both *Vs* and liquefaction resistance are similarly influenced by many of the same factors (e.g.,

void ratio, state of stress, stress history, and geologic age). Some advantages of using *Vs* (Dobry et al. 1981; Seed et al. 1983; Stokoe et al. 1988a; Tokimatsu and Uchida 1990) are that:

1. measurements are possible in soils that are hard to sample, such as gravelly soils where penetration tests may be unreliable;

2. measurements can also be performed on small laboratory specimens, allowing direct comparisons between laboratory and field behaviour;

3. *Vs* is a basic mechanical property of soil materials, directly related to small-strain shear modulus $G_{\max}$ by:

$$G_{\max} = \rho \cdot V_S^2$$

   where ρ is represents the mass density of the soil;

4. *Vs* can be measured by down-hole tests, or by *MASW* (*M*ultichannel *A*nalysis of *S*urface *W*aves).

The evaluation procedure requires the calculation of three parameters: (1) The level of cyclic loading on the soil caused by the earthquake, expressed as a cyclic stress ratio; (2) stiffness of the soil, expressed as an overburden stress-corrected shear-wave velocity; and (3) resistance of the soil to liquefaction, expressed as a cyclic resistance ratio. Each parameter is discussed below.

- ***Cyclic Stress Ratio* (*CSR*)**: the cyclic stress ratio at a particular depth in a level soil deposit can be expressed (Seed and Idriss, 1971) as:

$$CSR = \frac{\tau_{av}}{\sigma'_v} = 0.65 \cdot \left(\frac{a_{\max}}{g} \right) \cdot \left(\frac{\sigma_v}{\sigma'} \right) \cdot r_d$$

where τ_{av} is the average equivalent uniform cyclic shear stress caused by the earthquake and is assumed to be 0.65 of the maximum induced stress; $a_{\max}$ is the peak horizontal ground surface acceleration; g is the acceleration of gravity; σ'_v is the initial effective vertical (overburden) stress at the depth in question; σ_v is the total overburden stress at the same depth; and r_d shear stress reduction coefficient to adjust for the flexibility of the soil profile.

- ***Cyclic Resistance Ratio* (*CRR*)**: the cyclic resistance ratio at a particular depth can be expressed in the modified form of Andrus and Stokoe as:

$$CRR = \left\{ a \cdot \left(\frac{V_{S1}}{100} \right)^2 + b \cdot \left(\frac{1}{V_{S1}^* - V_{S1}} - \frac{1}{V_{S1}^*} \right) \right\} \cdot MFS$$

where V_{S1}^* is the limiting upper value of V_{S1} for cyclic liquefaction occurrence, *a* and *b* represent curve fitting parameters and *MSF* is a scaling factor to account for the effect of earthquake magnitude.

- **Stress corrected shear-wave velocity:** Following the traditional procedures for correcting SPT blow count and CPT resistances to account for overburden stress, one can correct V_S to a reference overburden stress (Sykora, 1987; Robertson et al., 1992):

$$V_{S1} = V_S \cdot C_V = V_S \cdot \left(\frac{P_a}{\sigma_v'} \right)^{0.25}$$

where V_{S1} is the overburden stress-corrected shear-wave velocity, C_V is the factor to correct measured shear-wave velocity for overburden pressure, P_a is the reference stress of 100 kPa or about atmospheric pressure; and σ_v' is the initial effective overburden stress (kPa). A maximum *CV* value of 1.4 is generally applied to V_S data at shallow depths, similar to the SPT and CPT procedures.

A common way to quantify the potential for liquefaction is in terms of a *factor of safety*. The factor of safety *FS* against liquefaction can be defined by

$$FS = \frac{CRR}{CRS}$$

Liquefaction is predicted to occur when $FS \le 1$, and liquefaction is predicted not to occur when $FS > 1$. The acceptable value of *FS* will depend on several factors, including the acceptable level of risk for the project, potential for ground deformation, extent and accuracy of seismic measurements, availability of other site information, and conservatism in determining the design earthquake magnitude and expected value of $a_{\max}$.

5. DATA ANALYSIS AND RESULTS

In this Section the results of the measurements conducted on the study area are presented; such results include seismic noise measurements (single stations and seismic arrays), geognostic drillings and laboratory tests. The aforementioned techniques are finalized to reconstruct the trend of the top of the metamorphic bedrock in the study area, assess the dynamic behavior of soils, and to perform preliminary analysis on liquefaction risk and 1D modelling.

5.1 Seismic Noise Measurements: Single Station Analysis

In the first part of this Doctoral Thesis a long campaign of seismic noise measurements has been conducted on the study area; such measurements include single station analysis (H/V - Nakamura technique), and seismic noise array analysis. The Figure below illustrates the position of the Test Site of S. Agostino Church and the Bretti&Enotrii Museum in relation to its regional context of the Crati Valley.

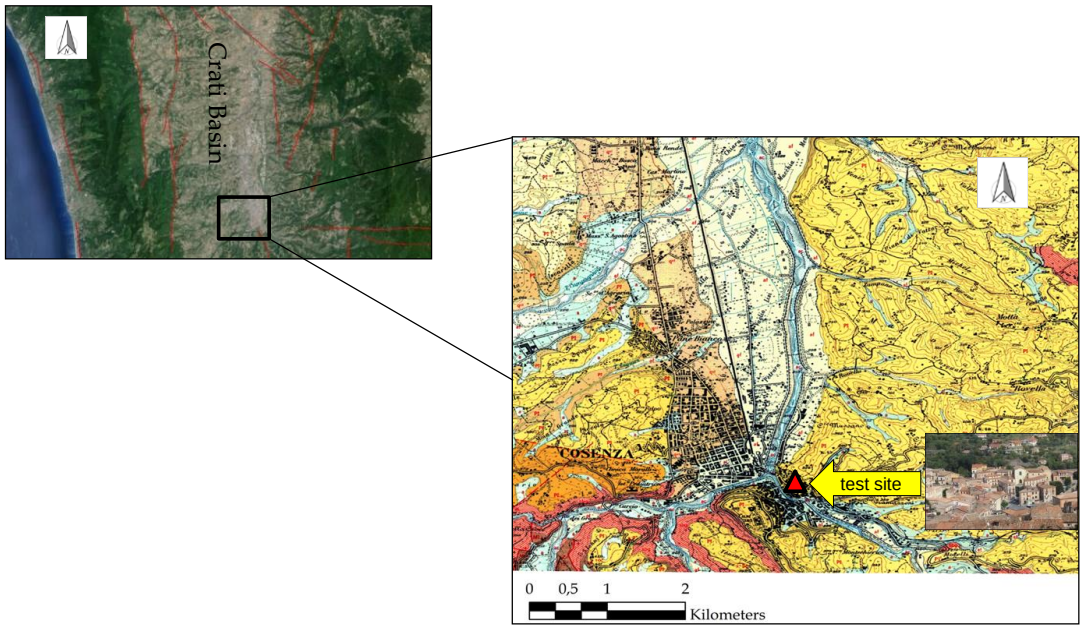

Figure 5.1 Position of the Test Site of S. Agostino Church and Bretti&Enotrii Museum in the geological context of the Crati Basin.

As shown in the previous Figure, the Test Site of San Agostino is located in the historical center of the city of Cosenza, in an complex area due to its high urbanization degree and its particular geo-morphologic conditions; in fact, considering the geological map in Figure 5.1, the area of the Test Site is located at the beginning of the Crati Valley, more in detail in the zone of confluence between Crati and Busento rivers; the area is characterized by the presence of alluvial and marine sediments (essentially sands, clays and gravels) overlying a metamorphic bedrock forming the basement of all the Crati Basin; such bedrock in partially outcropping in the South-West Test Site area (see Figure 5.1).

At the beginning of the project, in order to assess the dynamic response to an hypothetical seismic input in the study area, it was necessary to evaluate the dynamic response of the regional geological context in which it is locate, namely the Southern part of the Crati Basin (High Crati Valley). As mentioned in Section 4, the H/V technique is a simple estimation tool for local site effects as not only the predominant frequency, but also the amplification factor. For this reason, besides the Test Site area, 4 study sites were chosen in the city of Cosenza; such sites are shown in the Figure 5.2 below:

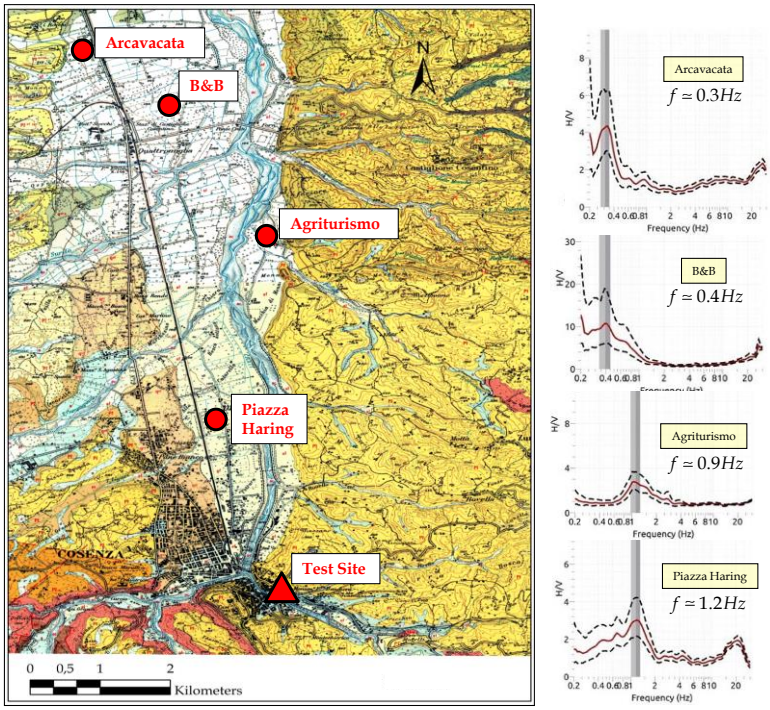

Figure 5.2 Left: Selected sites for preliminary study in the Crati Basin; Right: H/V curves (in red) ± standard deviations (dashed lines in black) obtained by single station measurements in different point for each study site.

The chosen sites for the identification of resonance frequencies, moving from South to North, are piazza Haring, Agriturismo, B&B and Arcavacata. For the study use was made of resolution digitizer stations (Reftek-130) connected to a three-component sensors (Lennartz Le3D; eigen-frequency of 0.2 Hz) recording seismic noise; the sampling rate in data acquisition was fixed to 500 samples/s. For each site H/V curves were estimated in different positions and using different acquisition times; the same value of the resonance frequencies identified in different positions for each site validated a local near-surface geology consisting in plane and parallel layers. All H/V curves were computed through an anti-trigger software implemented within the SESAME project (SESAME deliverable no.D09.03). Also according to the SESAME deliverable D23.12, all the peaks of the H/V spectral ratio may be considered as representative.

The same analysis were performed in different positions in the Test Site area; in this case, considering the high degree of urbanization and morphology complexity, such technique was the only one to be performed. The results in this case is shown in the Figure 5.3.

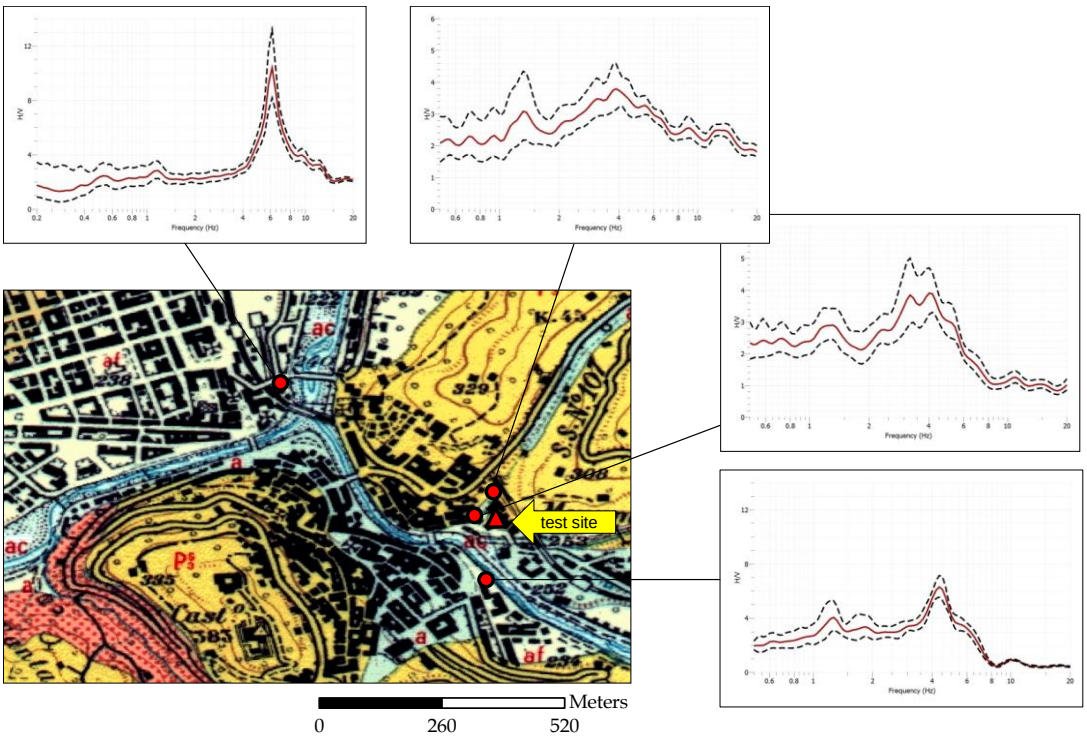

Figure 5.3 H/V curves (in red) ± standard deviations (dashed lines in black) obtained by single station measurements in the Test Site area.

As shown in Figure 5.3, the area of the Test Site is characterized by different resonance frequencies (from 1.2 Hz to 6 Hz) in very low distances of order of 100-200 m and different amplification factors (from 4 to 10); the resonance frequency in the other sites (Figure 5.2) tends to lower values moving from South to North (from 1.2 Hz for piazza Haring, 0.9 Hz for Agriturismo, 0.4 Hz for B&B, and 0.3 Hz for site Arcavacata). Considering these results it can be assumed a high heterogeneity for the near-surface geology characterizing the Test Site area, far away from an ideal model consisting in plane and parallel layers. Recalling the relationship between resonance frequency f_0 identified in the H/V curve and thickness h of soft covers overlaying a more rigid bedrock ($f_0 = \langle Vs \rangle / 4h$), it can be assumed a great deepening of this contact from the test Site area to site Arcavacata. Considering the available data in literature for the geology of the Crati Basin (Spina et al., 2011), the aforementioned contact is assumed to be between sedimentary covers (alluvial and marine sediments) and the metamorphic bedrock forming the basement of the Crati Basin.

Considering the previous preliminary, in order to evaluate the dynamic response for the Test Site area, located at the beginning of the Crati Basin, the study can be limited to the area of piazza Haring site, where resonance frequency of 1.2 Hz was encountered; in fact, observing more in detail the Figure 5.3, such resonance frequencies was identified in some measurements point in the surroundings of the Test Site, probably referred to the same deep interface.

As final remark it must be underlined that the study of the resonance frequencies is of fundamental importance not only because it provides information on the average shear-wave velocity $\langle Vs \rangle$ of soft covers and its dynamic equivalent thickness *h* respect to a more rigid bedrock, but especially to the dynamic response of the civil infrastructure insisting in the area invested by a seismic wave field; in fact, in the case in which such resonance frequency f_0 coincides with one proper oscillation modes of a built all the energy carried by the resonance frequency of the ground is transferred to the structure with easily imaginable consequences. In a recent paper (Gaudiosi et al., 2015) results of H/V performed in the Test Site are explained more in detail, revealing different dynamic responses to the Test Site.

5.2 Geognostic Drillings

As explained in the previous Section, the results of single noise-station measurements in the area of the Test Site revealed the presence of different resonance frequencies. More in detail, the 1.2 Hz peak was also encountered in the piazza Haring site, and for this the study of the dynamic response to the area of the Test Site was limited to that Site. Considering the particular geo-morphologic condition of the area, these results can be justified as representative of a high near-surface geology complexity probably due to different bedrock depths or different shear-wave velocities of the layers.

In order to investigate more in detail the validity of these results and compare them to the actual stratigraphy in the study area (from Test Site area to piazza Haring) a series of five boreholes were drilled in Summer 2014. The drillings, conducted by Laboratorio Geotecnico C.N.G. (Rome), was finalized to:

1. Obtain the actual stratigraphy of the study area;
2. Collect soil samples to perform laboratory tests;
3. Obtain a dynamic characterization of the soils encountered by means of down-hole test.

The positions of the boreholes, shown in the Figure 5.4, and named from S1 to S5, were chosen taking into account the positions were the high variability in the resonance frequencies were observed by seismic-noise single station, and also considering logistic criteria.

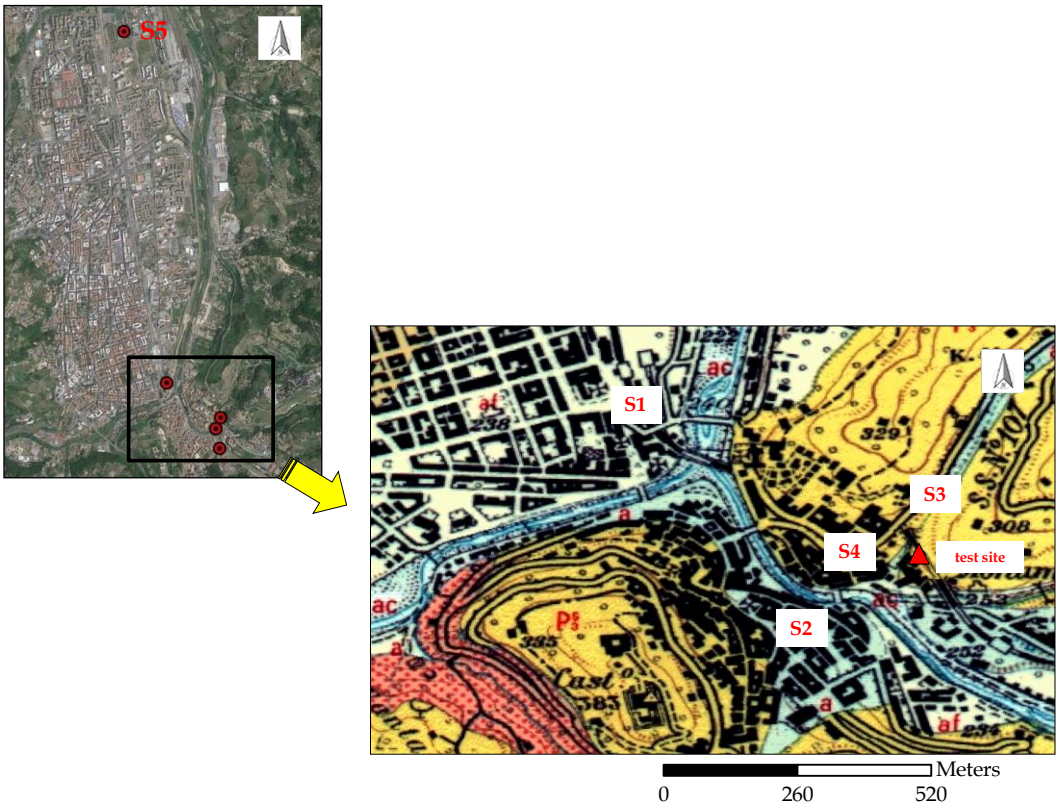

Figure 5.4 Location the boreholes; the dark box shows the detailed positions for the boreholes in the Test Site area.

The boreholes were so performed:

- Boreholes S2, S3, S4: Positions were chosen taking into account the results of single station measurements in the Test Site area, in order to obtain a geological section with the S. Agostino Church at the center.
- Borehole S1: Position was chosen inside a private property, in order to investigate geological lateral continuity with the Test Site area. In this case, position was also chosen for logistics for the installation of the permanent borehole sensor down to the drilling depth.
- Borehole S5: Position, located about 3 km northern away from the Test Site area, and about 1 km northern away from piazza Haring site, was chosen in order to obtain a reference stratigraphy of the High Crati Valley, far away from the erosive action due to the Crati and the Busento rivers. The choice of this specific position was exclusively due to logistics

For all the boreholes, the drilling depth was reached until the contact between the sedimentary covers and the metamorphic bedrock was encountered; the exception was for borehole S5 where the aforementioned contact was not founded.

During drilling operations many disturbed and undisturbed soil samples were collected for a detailed description of the lithologies encountered, and to perform laboratory tests where possible. In the Figure below synthetic stratigraphies encountered in study sites are presented.

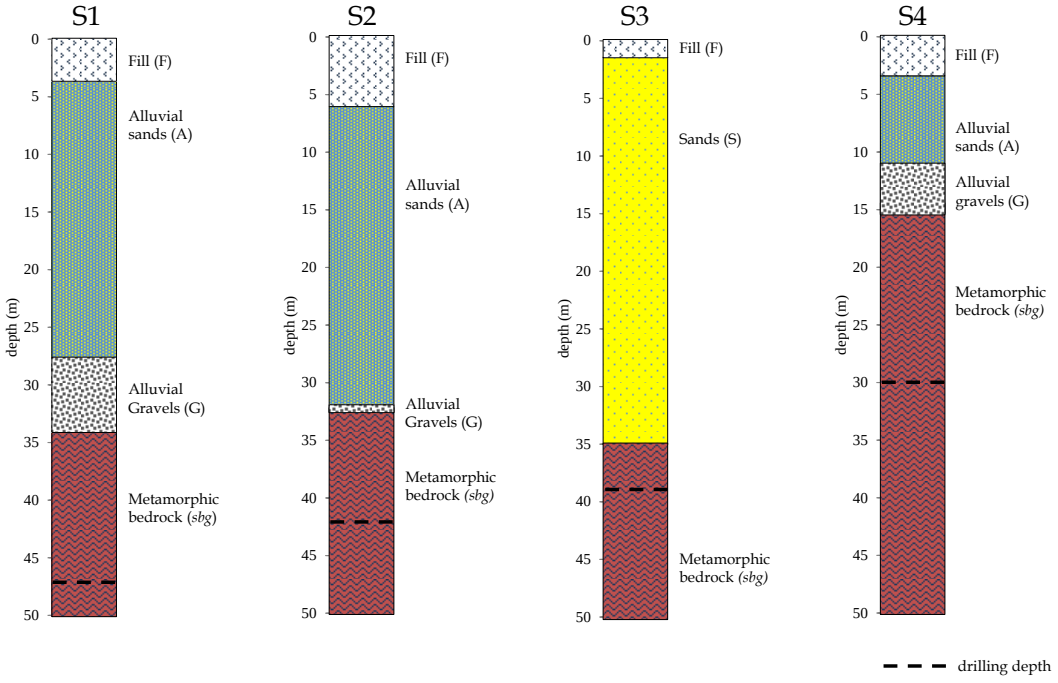

Figure 5.5 Synthetic stratigraphies obtained by drillings for sites S1, S2, S3 and S4.

Considering the geological characteristics of the drilled lithologies, the reconstructed stratigraphies can be divided into three groups:

- **S1, S2, S4**: The stratigraphies consist of a surface layer of variable thickness of man-made fill (layer F in Figure 5.5), and a second layer of variable thickness of alluvial materials (layer A), i.e. sands, gradually evolving locally into gravelly sands downwards (layer G). The above described alluvial succession is in erosional contact with metamorphic rocks, mainly consisting in granitic and biotitic-schists (*scisti biotitici e granatiferi - sbg*). The metamorphic bedrock is variously altered and poorly sampled for intense fracturing probably due to the erosive action of the Busento river.

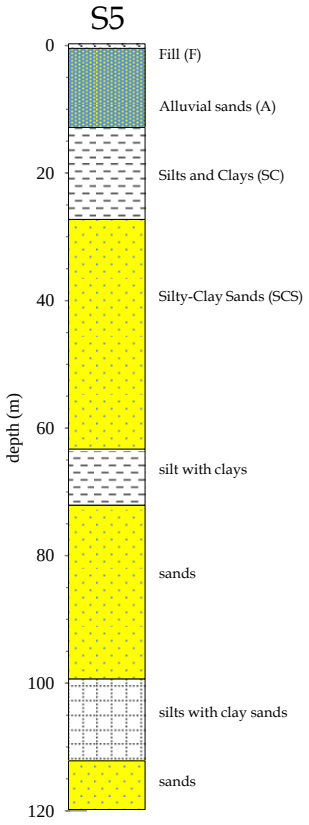

Figure 5.6 Synthetic stratigraphy obtained by drilling for site S5.

- **S3**: The stratigraphy consists of a surface layer of about 3.40 m of man-made fill (layer F), and a second layer of marine sands (layer S) gradually passing to gravelly sands downwards; these terrains are probably referred to the terraced Calabrian transgressive depositional sequence of Pleistocene forming the backbone of the reliefs surrounding the borehole (*sabbie bruno-chiare* - P_3^S). Also in this case the above described alluvial succession is in erosional contact with metamorphic rocks, mainly consisting in granitic and biotitic-schists (*scisti biotitici e granatiferi - sbg*).
- **S5**: The stratigraphy (Figure 5.6), about 3 km northern away from the Test site area, in the central part of the High Crati Valley, consists of a surface layer of 1.10 m of man-made fill (layer F), a second layer of about 12 m of alluvial sediments (sands and gravels, layer A), 15 m of silts and clays (level SC), 35 m of silty-clay sands (level SCS), 9 m of silts with clays, about 27 m of sands, about 9 m of silts with clay sands, and about 11 m of sands. The borehole was drilled down to 120 m below ground level, in correspondence of which the metamorphic bedrock (layer *sbg*) was not encountered.

5.3 *Down-Hole Test*

Boreholes drilled in each site allowed to obtain the actual stratigraphies of the sites. Down-hole test were performed down to the drilling depth in order to obtain a vertical shear-wave and compressional wave profile for each site under study. The tests were performed according to ASTM D7400-08. The sampled soils exhibit a high Vs variability, from 200 m/s for layer F (filling material), 400-800 m/s for layer A (alluvial sands), 800 m/s for layer S (marine sands), 700-900 m/s for layer G (alluvial gravels), and 800-1300 m/s for layer *sbg* (metamorphic bedrock).

Discontinuities identified in vertical shear-wave and compressional wave profiles are often related to different dynamic behaviour inside the same lithology (level A in S1 and S2, level S in S3), whereas only in some case are related to stratigraphic contacts between different lithologies (level F and *sbg* for all the sites).

The different dynamic behaviour for the metamorphic bedrock (layer *sbg*) is related both to the different petrographic nature of the same, from granitic schists for site S1 and S3, to biotitic schists for site S2 and S4, both to its geotechnical characteristics, more or less fractured; as previously mentioned this is probably due to high erosive action of the Crati and Busento rivers.

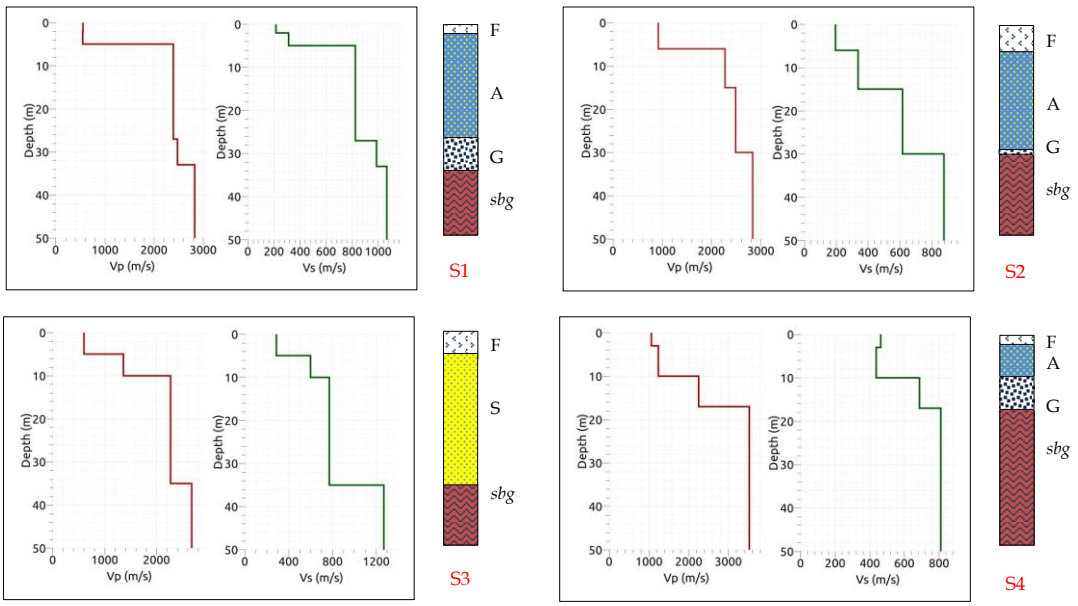

Figure 5.7 Velocity profiles obtained by down-hole test for sites S1 – S4.

For Site S5 down-hole tests will be shown in detail in Section 5.4.1.

5.4 Seismic Noise Measurements; Array Analysis

Boreholes drilled in the Test Site area (S1 – S4) and S5, and down-hole tests performed provided a static and a dynamic characterization for the soils encountered during the drilling operations. As previously mentioned for site S5, located in the central part of the High Crati Valley, the metamorphic bedrock, forming the basement of the Crati Basin, was not encountered. In order to obtain a complete dynamic characterization for all the geological layers in this area, two seismic arrays were performed in two different sites: the S5 site and the piazza Haring site previously described. The study was finalized to obtain a complete shear-wave velocity profile for the two sites, and inferring from it the hypothetic location of the top of the metamorphic bedrock.

In the two following Sections the aforementioned study will be described more in detail, including the results of the inversion process.

5.4.1 Site S5

A 2D array of seismic noise recording stations was designed for validating the shear-wave velocities obtained from down-hole test in the area of site S5. This analysis was performed to compare the experimental vertical velocity with the one obtained from down-hole test, and also to reach the hypothetic contact between sedimentary covers and metamorphic bedrock. The analysis was made of thirteen CENTAUR stations, equipped with Trillium Compact 120 s; the sampling rate was 250 samples/s.

The 2D array was realized around the position of borehole S5, in a central position of the High Crati Valley (Figure 5.8). The array has a triple equilateral triangle geometry with the central station located near borehole S5 (Figure 5.8). The external triangle (side of about 400 m) was used to reach higher depths and to sample smaller wave-numbers, while the internal triangles were used to prevent spatial aliasing due to high wavenumbers otherwise sampled as low (Wathelet et al., 2004). Considering that, in a circular array, the depth of investigation is 2-6 times the array's radius (Tokimatsu, 1995), the designed array made it possible to analyse higher depth than the one investigated by borehole and down-hole test, about 120 m below ground level.

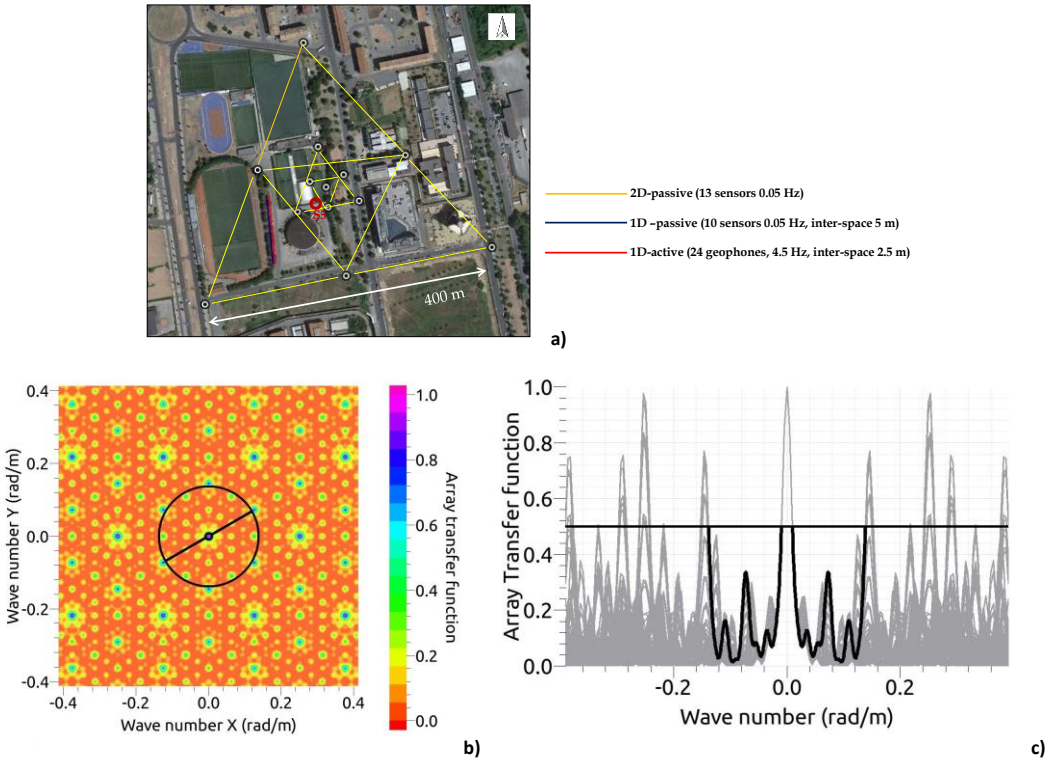

Figure 5.8 a) Arrays geometry for site S5; b) b) Array Transfer Function (ATF); the black circle and the black lines in the wave-number plane show the alias-lobe position. c) The ATF amplitude reaches the value of 0.5 ($k_{min/2}$) along the direction shown in the wave-number plane.

In order to quantify, in the wave number domain, the dependence of the spatial aliasing on the azimuth, the theoretical array transfer function (ATF) was computed for the array geometry, in order to estimate the array performance (Woods and Lintz, 1973; Asten and Henstridge, 1984). Following Di Giulio et al. (2006), and Bozzano et al (2008), $k_{\max}$ is defined as the distance in the wave-number domain between the main peak and the closest side lobe exceeding 50% of main lobe amplitude (Figure 5.8c). The maximum wave number resolution of the array was chosen as $k_{\max}/2$, while the radius of the main peak taken at its mid provides the lowest wave number $k_{\min}$ that can be resolved (Di Giulio et al., 2006). The so defined $k_{\max}/2$ and $k_{\min}$ were within the range of the empirical indication given by Tokimatsu (1995). For the analysis GEOPSY software package was used, which was developed as part of the European SESAME project (Site Effects Assessment using Ambient Excitations; see www.geopsy.org). In order to obtain a dispersion curve in a broader range of frequency, and to increase the level of detail close to ground surface, a 1D passive array and a 1D active array (Xia et al., 1999, Park et

al., 1999) were performed in the same area of the site S5 (Figure 5.8a); use was made of ten CENTAUR stations, equipped with Trillium Compact 120s, with interspace of 5m, for the 1D passive array, and 24 geophones 4.5Hz, with interspace of 2.5m, for the 1D active array

At first, the spectral ratios of the horizontal and vertical components of the noise field (H/V ratio, Nogoshi and Igarashi, 1971; Nakamura 1989, 2000) were computed for all the stations of 2D and 1D passive array, in order to identify the fundamental frequencies in which the energy is concentrated (Lermo and Chavez Garcia, 1993). The graph in Figure 5.9b shows the H/V curve for one station. All H/V curves were computed through an anti-trigger software implemented within the SESAME project (SESAME deliverable no.D09.03). According to the deliverables D18.06-Wp, D19.06-Wp and D24.13-Wp, the peaks of the H/V spectral ratio may be considered as representative, since spectral ratios are in the range of 3-4 and equal for all the 2D and 1D passive array. In addition, the standard deviation is less than 3 for all the stations. Taking into account this results, it can be assumed that the near surface geology for the study area of borehole S5 can be modelled as plane and parallel layers. Supposing that ambient vibrations are mainly composed by surface waves, and Rayleigh waves are predominant (compared to body waves) in the vertical motion (Tokimatsu, 1995), the Rayleigh wave dispersion curve was computed using 120 minutes of noise array recording of the vertical components.

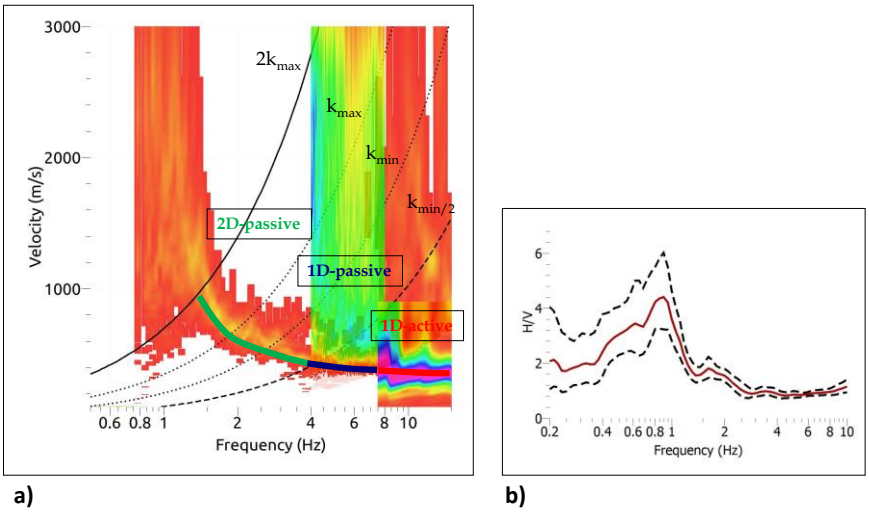

Figure 5.9 a) H/V spectral ratio ± standard deviation for one station of 2D and 1D passive array in the S5 site; experimental dispersion curve obtained combining active and passive measurements.

The Rayleigh dispersion curve obtained combining the three different array technique shows a good trend agreement, (Figure 5.9a). As shown in Figure 5.9a, the upper frequency limit was chosen as the intercept of the dispersion curve of the 2D passive array corresponding to $k_{max}/2$ defined from ATF (Scherbaum et al., 2003; Wathelet et al., 2004), while the lower frequency limit was chosen as the intercept of the dispersion curve with the aliasing curve corresponding to $k_{min}/2$. Combining the three different array technique it was possible to overcome the spatial resolution limit due to the single 2D array, and obtain a Rayleigh dispersion curve in a broader range of frequency, especially in the high frequencies range.

The Rayleigh dispersion curve was inverted through an inversion algorithm (Sambridge, 1999a; Wathelet et al., 2004, 2008) to obtain a shear-wave velocity profile for site. The inversion process was implemented using the surface shear-wave velocities evaluated during down-hole test for the first layers. In order to constrain the compressional wave values in the inversion process for the first two layers, a seismic refraction tomography was performed along the same direction on 1D-active and passive array (Figure 5.10, Foti et al., 2003). The analysis was performed using 24 geophones with inter-space of 3m, and eigen-frequency of 10 Hz.

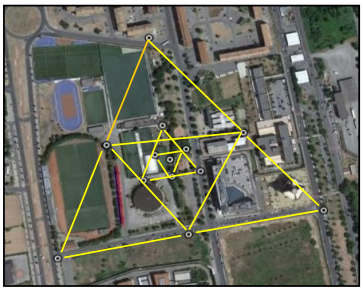

(24 geophones, 10 Hz, inter-space 3 m)

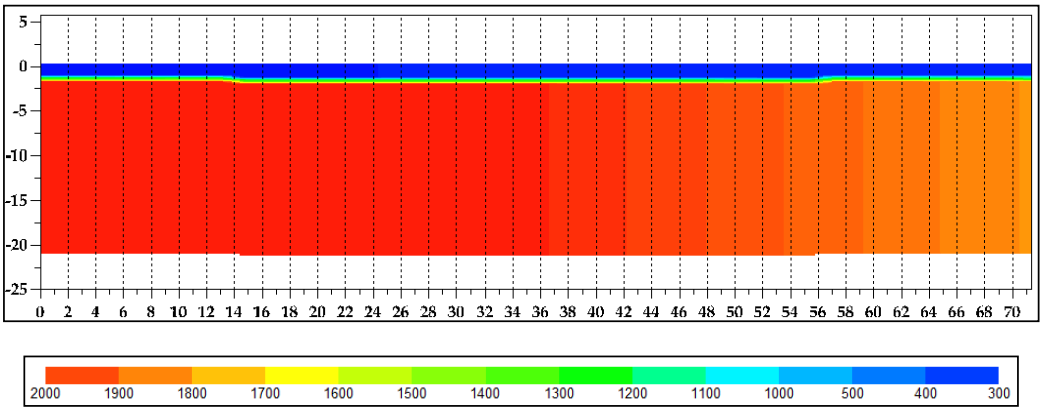

Figure 5.10 Seismic refraction tomography performed in the S5 site.

As shown in Figure 5.11, the inverted Vs profile exhibits a good agreement with the one obtained by borehole for the first three layers below ground level, around 60 m b.g.l., depth we can assume credible for such kind of test (filling material F, alluvial sands A, silts and clays SC); however, two high velocity contrasts are found at about 130 m and 210 m below ground level. Comparing the Vs value with bedrock velocity measured by boreholes in site S1 – S4, and taking into account geological criteria, it can be assumed that the first contrast is located between two different sand levels (level S1 and S2), while the second one is the position of the contact between sedimentary covers (alluvial and marine deposits) and the metamorphic bedrock (*sbg*). The low Vs values for the metamorphic bedrock, about 1200 - 1400 m/s, are probably referred to its low geotechnical properties due to the erosive contact with the sedimentary covers. It must be underlined that such dynamic model is in good agreement with the resonance frequency of 0.8 - 0.9 Hz observed by seismic noise measurements.

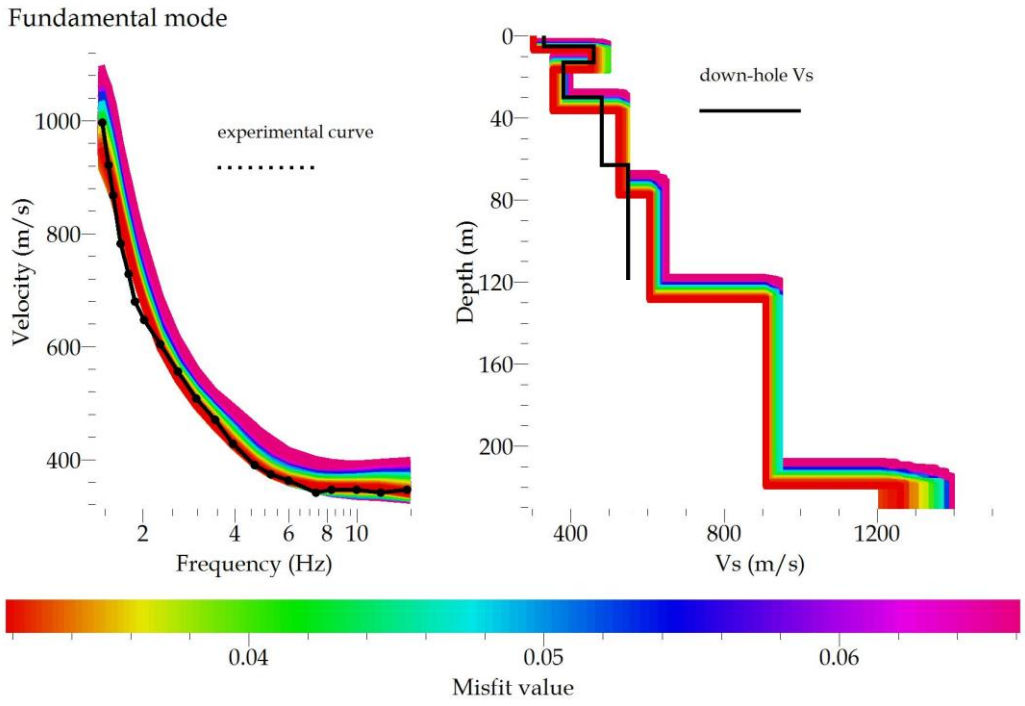

Figure 5.11 Left: Experimental dispersion curve (black dots) compared with dispersion curve obtained through inversion; the relative misfit is shown. Right: Vertical shear-wave velocity profile obtained through inversion, compared to down-hole test (black line).

Taking into account the inverted shear-wave velocity profile and the geology of the area, the new two seismic interfaces founded at 130 m and 210 m below ground

level, can be interpreted as two distinct sand layers. As shown in Figure 5.12 the aforementioned layers are indicated as layers S1 and S2, respectively.

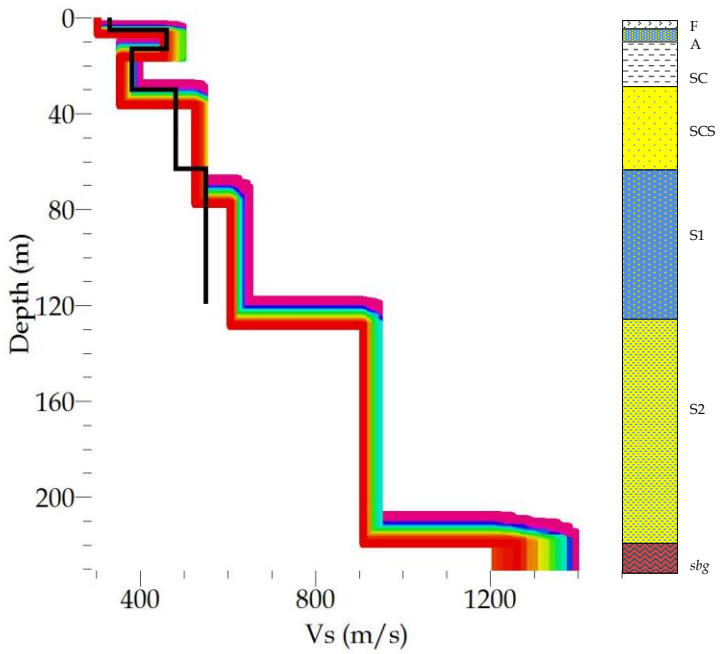

Figure 5.12 Shear-wave velocity profile obtained by inversion compared to down-hole test (dark line); right: geological interpretation of vertical profile.

5.4.2 Site Piazza Haring

As done for Site S5, a 2D array of seismic noise recording stations was designed in piazza Haring Site in order to obtain a shear-wave velocity profile. This analysis was performed to fill the gap of borehole and down-hole test for this site, and also to reach the hypothetic contact between sedimentary covers and metamorphic bedrock. In this case the analysis was made of ten REFTEK130 stations, equipped with Lennartz 3D 5s; the sampling rate was 500 samples/s. The array has a triple equilateral triangle geometry with a central station (Figure 5.13). The external triangle (side of 200 m) was used to reach higher depths and to sample smaller wave-numbers, while the internal triangles were used to prevent spatial aliasing due to high wavenumbers otherwise sampled as low (Wathelet et al., 2004).

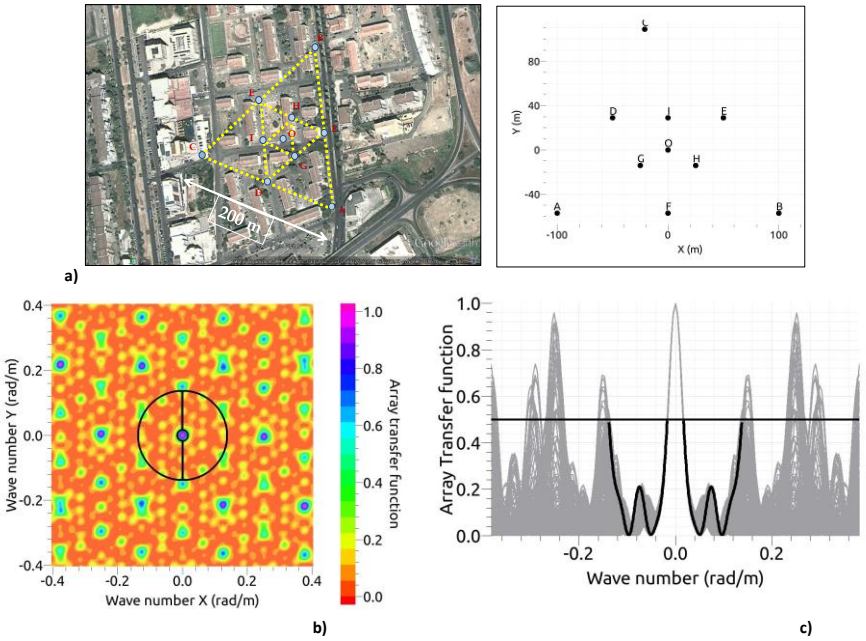

Figure 5.13 a) Array geometry for piazza Haring Site; b) b) Array Transfer Function (ATF); the black circle and the black lines in the wave-number plane show the alias-lobe position. c) The ATF amplitude reaches the value of 0.5 ($k_{min/2}$) along the direction shown in the wave-number plane.

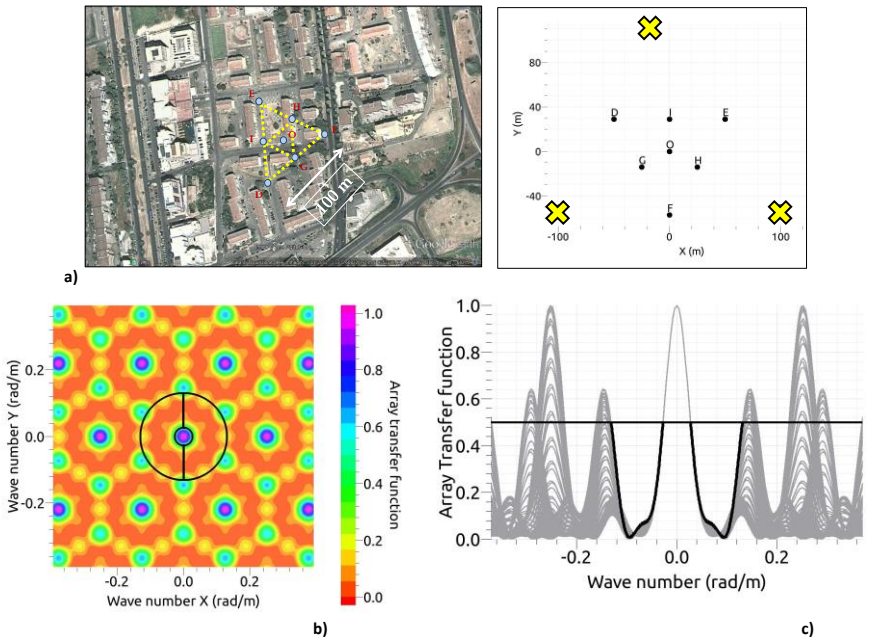

Figure 5.14 a) New array geometry for piazza Haring Site; b) b) Array Transfer Function (ATF); the black circle and the black lines in the wave-number plane show the alias-lobe position. c) The ATF amplitude reaches the value of 0.5 ($k_{min/2}$) along the direction shown in the wave-number plane.

At first, the spectral ratios of the horizontal and vertical components of the noise field (H/V ratio) were computed for all the stations. In this case stations A, B and C forming the external side, did not exhibit the main resonance frequency identified for all the other stations; taking into account previous considerations it can be assumed that locally the condition of plane and parallel layers was not satisfied. Considering this the aforementioned stations were removed from the analysis and the ATF was recalculated as shown in Figure 5.14. Supposing that ambient vibrations are mainly composed by surface waves, and Rayleigh waves are predominant (compared to body waves) in the vertical motion (Tokimatsu, 1995), the Rayleigh wave dispersion curve was computed using 100 minutes of noise array recording of the vertical components.

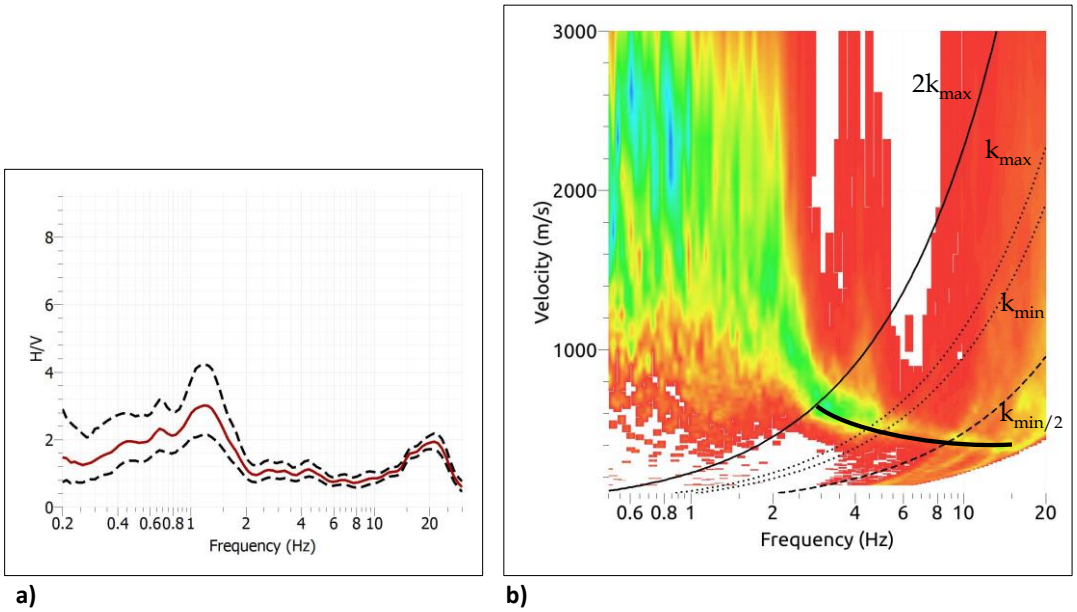

Figure 5.15 a) H/V spectral ratio ± standard deviation for one station of 2D array in piazza Haring site; experimental dispersion curve obtained seismic noise measurements.

The Rayleigh dispersion curve obtained is shown in the Figure 5.15b; as shown, the upper frequency limit was chosen as the intercept of the dispersion curve of the 2D passive array corresponding to $k_{\max}/2$ defined from ATF, while the lower frequency limit was chosen as the intercept of the dispersion curve with the aliasing curve corresponding to $k_{\min}/2$. In this case, considering the different array geometry for the 2D array respect the beginning (100 m of external side respect the original 200 m of external side), a combined inversion was performed using the H/V curve obtained by seismic noise measurements (Picozzi, 2005); such

analysis was performed in order to reach higher depth. The results of the inversion problem are shown in the Figure 5.16.

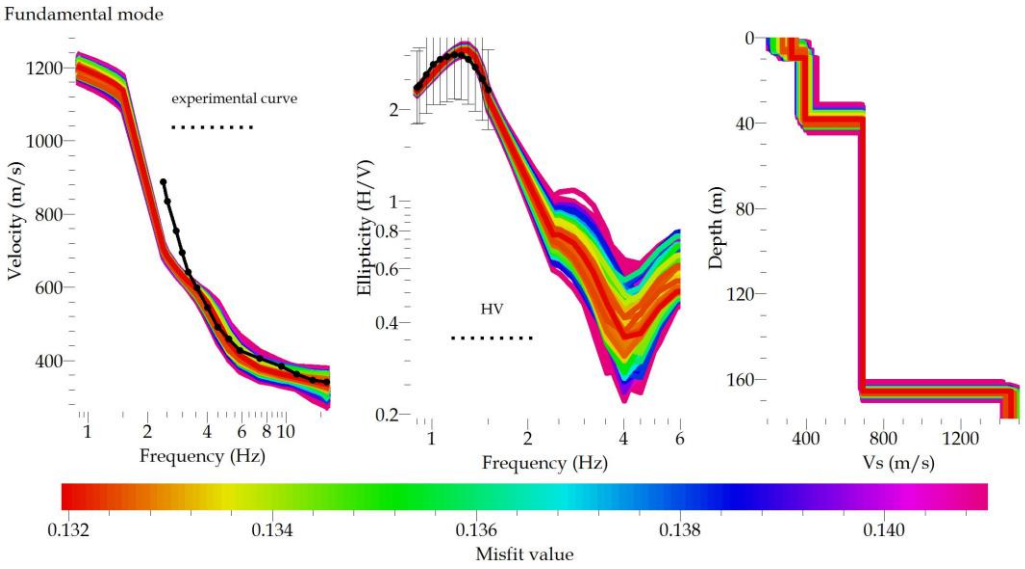

Figure 5.16 a) Experimental dispersion curve compared to that obtained through inverse problem; b) Experimental H/V curve compared to ellipticity curve of Rayleigh waves obtained through inverse problem; c) vertical shear-wave velocity profile obtained. For all results the relative misfit values are shown.

The result of the inverse problem reveals a good agreement between H/V curve and ellipticity (Figure 5.16b), while for the experimental dispersion curve a great mismatch is encountered for low frequencies (below 3 Hz). The vertical shear wave profile (Figure 5.16c) shows three different seismic interfaces: a first interface at about 10 m below ground level, a second interface at about 40 m below ground level and a deeper interface at about 170 m. Comparing the Vs velocity values with those obtained for Site S5 and geological criteria, we can assume: the first layer due to filling materials and/or alluvial sediments (layers F and A); the second layer due to silts and clays, or/and silty-clay sands (layers SC and SCS); the third layer due to marine sands (layer S1); the deepest layer due to the contact between marine sands and metamorphic bedrock (layer *sbg*). The aforementioned vertical dynamic model is shown in the Figure below (column H1).

In order to obtain a dynamic model in good agreement with the H/V peak at 1.2 Hz observed by seismic noise analysis, the model H1 was corrected reducing the thickness of the layer S1 (column H2 in Figure 5.17). Taking into account this new

dynamic model the contact between sedimentary covers and metamorphic bedrock is estimated at about 135 m below ground level.

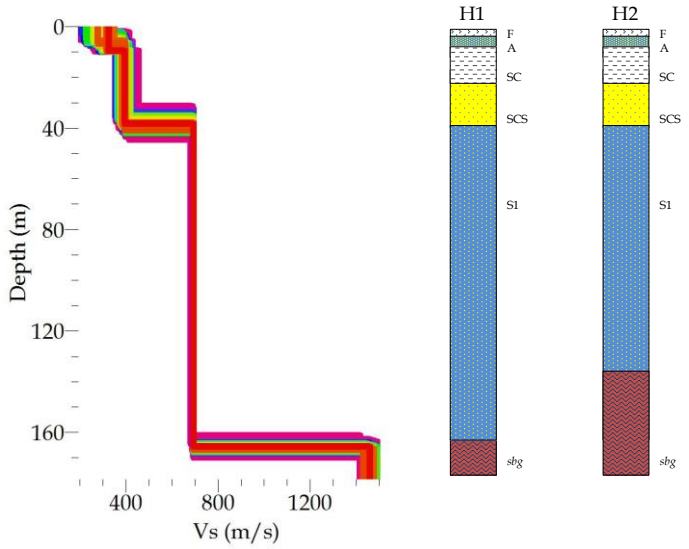

Figure 5.17 Left: vertical shear-wave velocity profile obtained through inverse problem; Right: column H1: vertical dynamic model interpreted by inverse problem; Right: column H2: corrected dynamic model in good agreement with the H/V peak at 1.2 Hz observed by seismic noise analysis.

5.5 Geological Reconstruction of the Study Area

As described in Section 5.2, the results of the drillings revealed two different geological areas:

1. The Test Site area;
2. The High Crati Valley area.

The Test Site area was statically and dynamically reconstructed with boreholes S1 - S5 and down-hole tests, thanks to which the contact between sedimentary covers and metamorphic bedrock was encountered. For the High Crati Valley area, reconstruction was done taking into account the partial stratigraphy of borehole S5 and seismic noise analysis performed in the aforementioned site and in piazza Haring; in this case, knowledge of the geology of the study linked to the results of the Test Site area, allowed to identify the possible position of the contact between soft-covers and bedrock.

5.5.1 *Test Site Area*

Considering the results obtained by boreholes S1-S4 a simplified geological section in Test Site area was realized, as shown in Figure 5.18:

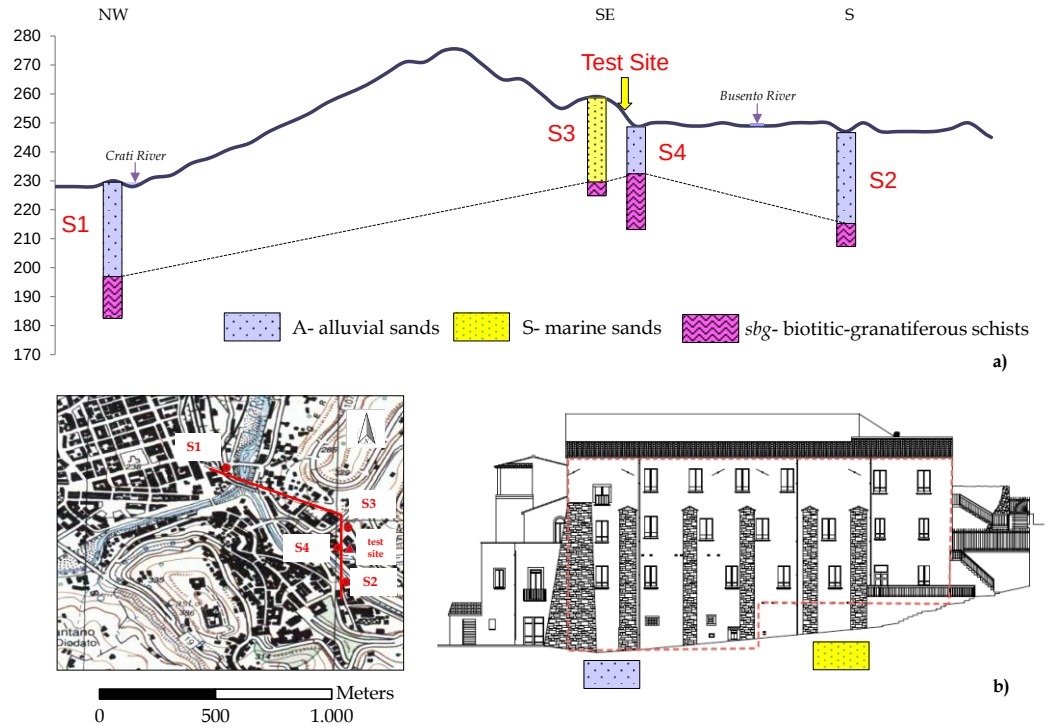

Figure 5.18 a) Simplified geological model of the Test Site area along the direction in red shown in the Figure in the box; b) Lateral view of the Test Site in relation to the subsoil nature.

As shown in the Figure above, the Test site area is essentially characterized by the presence of alluvial sediments (level A, sands and gravels) of the Crati and Busento rivers, and marine sands (level S) in the case of borehole S3; this exception is probably referred to the high topographic position where the borehole was drilled, far away from the erosive action of the Busento river. The most interesting result deduced from the simplified geological model is that the Test Site of S. Agostino Church was built in between two distinct lithologies: the aforementioned marine sands (level S) behind, and the alluvial sediments of the Busento river (level A) in front. This results was hypothesized at the beginning of the study, both from a general geological survey of the area, both from the different resonance frequencies observed in the single station measurements. This observation is a crucial factor for monitoring the building, considering the different geotechnical behavior of the aforementioned lithologies; for more detail see Gaudiosi et al., 2015.

5.5.2 *High Crati Valley Area*

For the geological reconstruction of the High Crati Valley, more in detail in the urban area of the city of Cosenza, the result was reached considering the partial stratigraphy obtained by borehole S5, down to 120 m below ground level, and vertical shear-wave profiles obtained through inversion of dispersive wave for site S5 and piazza Haring site. In this case, the stratigraphies were reconstructed using geological criteria and comparing Vs velocity with the ones obtained by down-hole tests in the Test Site area.

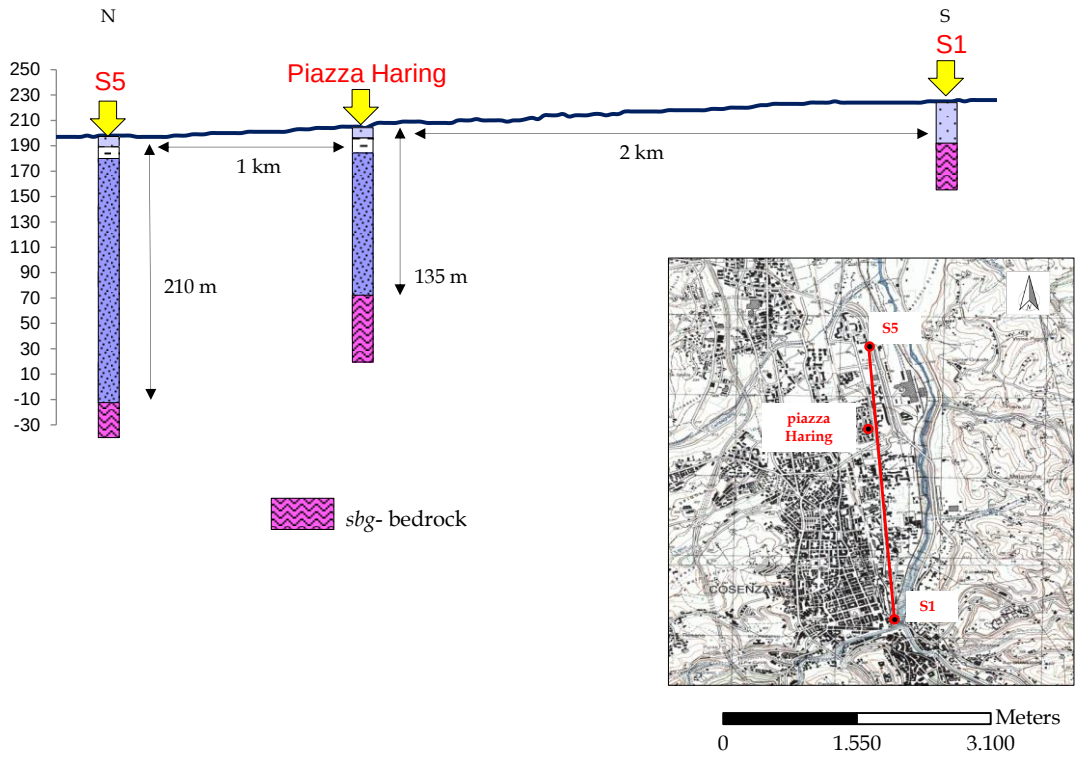

Figure 5.19 Simplified geological model of the High Crati Valley in the urban area of the city of Cosenza along the direction in red shown in the Figure in the box.

The most interesting result resumed from the proposed model in the Figure above, is a deepening of the contact between soft-covers (alluvial and marine deposits) and metamorphic bedrock of the Crati Valley (*sbg*) moving from Test Site area (more in detail from borehole S1 in the model) and borehole S5, approximatively from South to North direction. This result is completely in accord with the resonance frequencies identified by single station measurements, according to which a decreasing frequency peak in the H/V curve was observed along the same direction.

5.6 Laboratory Tests

As previously mentioned, many soil samples were collected during drillings; the main purpose was to obtain a detailed description of the lithologies encountered during the drilling operations and to perform, where possible, laboratory tests. In the following Table a summary of samples collected during boreholes is shown:

borehole	Disturbed sample	Undisturbed sample	SPT
S1	5	0	2
S2	6	0	4
S3	8	0	1
S4	3	0	1
S5	17	3	1

Table 5.1 Summary of sampled soil collected during boreholes

As shown in the Table above, the particular soil conditions allowed to collect undisturbed samples only for borehole S5; for this reason the analysis for these samples will be described more in detail.

All the samples collected during boreholes were classified through gradation curved following standard, ASTM D424, and ASTM D422. For the execution of Standard Penetration Test (SPT), standard ASTM - D1586-67(74) D1586-84 were followed.

The results of laboratory test are shown in the following Sections.

5.6.1 *Site S1*

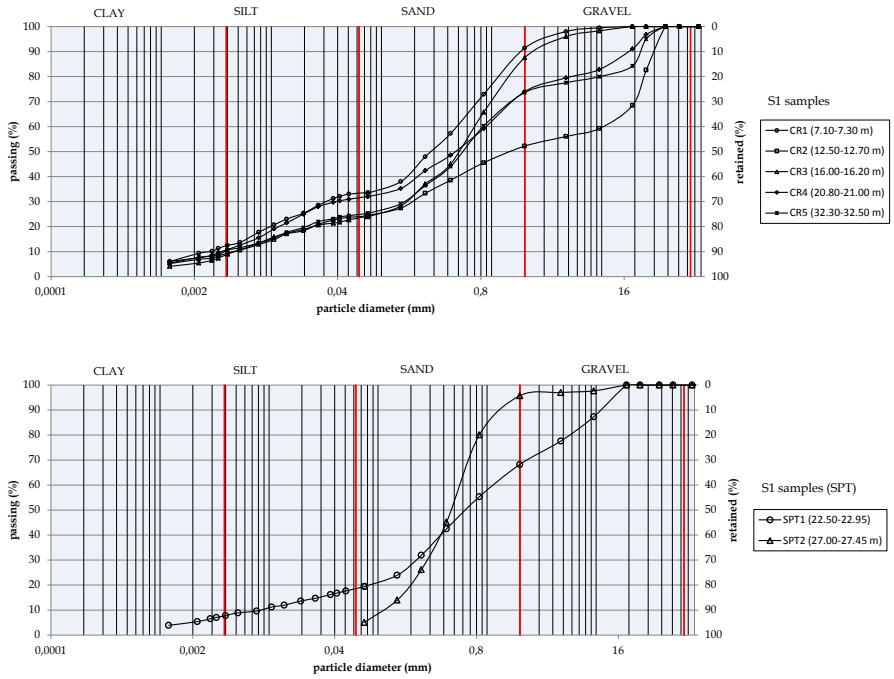

Figure 5.20 Gradation curves for samples collected during borehole S1.

Sample	CR1	CR2	CR3	CR4	SPT1	SPT2	CR5
depth (m)	7.10–7.30	12.50–12.70	16.00-16.20	20.80-21.00	22.50-22.95	27.00-27.45	32.30-32.50
γ_S (kN/m³)	27.22	28.20	26.95	27.28	26.52		26.55
D_{10} (mm)	0.003	0.005	0.005	0.004	0.009	0.110	0.004
D_{60} (mm)	0.48	10.092	0.7	0.889	1.155	0.570	0.840
AASHTO CNR-UNI 10006	N.D.	A-1-b	A-1-b	N.D.	A-1-b	A-1-b	A-1-b

Table 5.2 Physical parameters from laboratory tests for samples collected in borehole S4.

5.6.2 *Site S2*

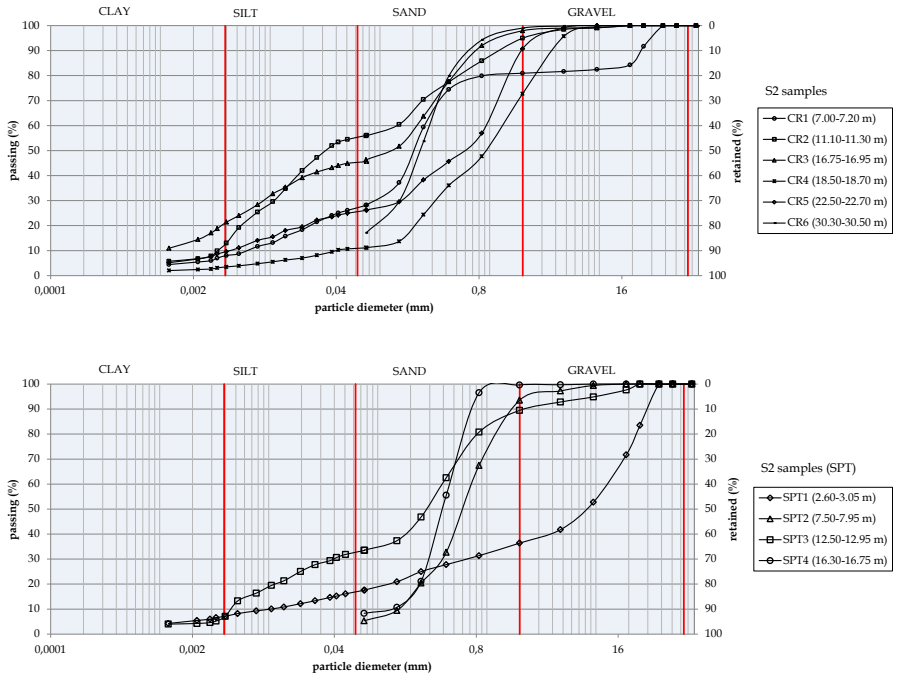

Figure 5.21 Gradation curves for samples collected during borehole S2.

sample	SPT1	CR1	SPT2	CR2	SPT3	SPT4
depth (m)	2.60-3.05	7.00-7.20	7.50-7.95	11.10-11.30	12.50-12.95	16.30-16.75
γ_S (kN/m³)	2.60-3.05	7.00-7.20	7.50-7.95	11.10-11.30	12.50-12.95	16.30-16.75
D_{10} (mm)	0.011	0.006	0.154	0.004	0.005	0.121
D_{60} (mm)	12.404	0.255	0.732	0.139	0.390	0.458
AASHTO CNR-UNI 10006	A-1-b	N.D.	A-1-b	N.D.	N.D.	A-3

Sample	CR3	CR4	CR5	CR6
depth (m)	16.75-16.95	18.50-18.70	22.50-22.70	30.30-30.50
γ_S (kN/m³)	26.58	26.20	26.22	
D_{10} (mm)		0.043	0.004	
D_{60} (mm)	0.213	1.293	0.917	0.284
AASHTO CNR-UNI 10006	N.D.	A-1-b	N.D.	N.D.

Tables 5.3 Physical parameters from laboratory tests for samples collected in borehole S2.

5.6.3 *Site S3*

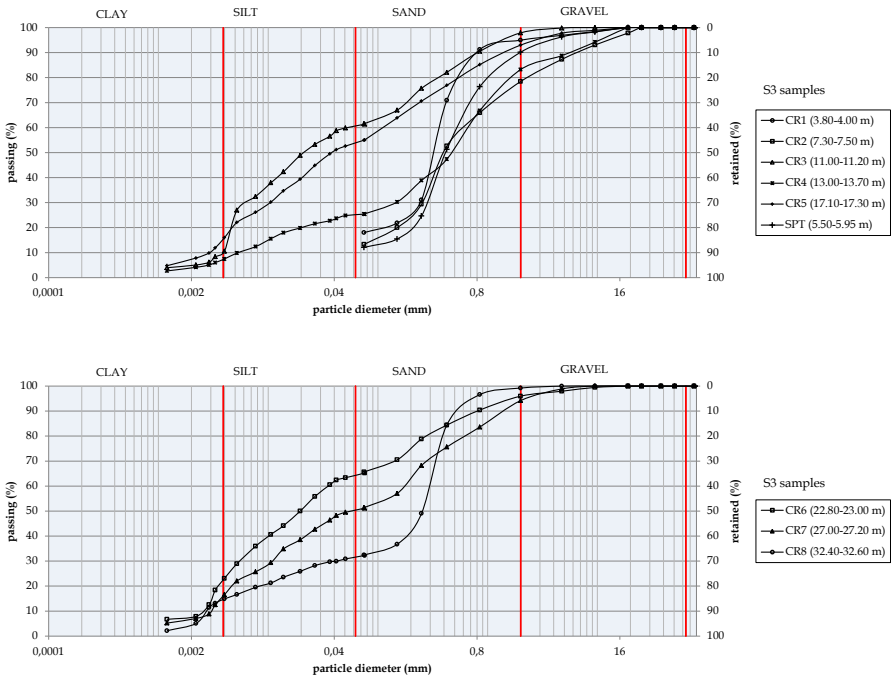

Figure 5.22 Gradation curves for samples collected during borehole S3.

sample	CR1	SPT1	CR2	CR3	CR4	CR5
depth (m)	3.80-4.00	5.50-5.95	7.30-7.50	11.00-11.20	13.00-13.70	17.10-17.30
γ_S (kN/m³)				26.84	26.69	27.09
D_{10} (mm)				0.004	0.006	0.003
D_{60} (mm)	0.367	0.541	0.623	0.054	0.666	0.110
AASHTO	N.D.	N.D.	N.D.	N.D.	A-1-b	N.D.
CNR-UNI 10006						

sample	CR6	CR7	CR8
depth (m)	22.80-23.00	27.00-27.20	32.40-32.60
γ_S (kN/m³)	26.96	26.86	26.61
D_{10} (mm)	0.003	0.003	0.003
D_{60} (mm)	0.036	0.172	0.296
AASHTO	N.D.	N.D.	N.D.
CNR-UNI 10006			

Tables 5.4 Physical parameters from laboratory tests for samples collected in borehole S2.

5.6.4 *Site S4*

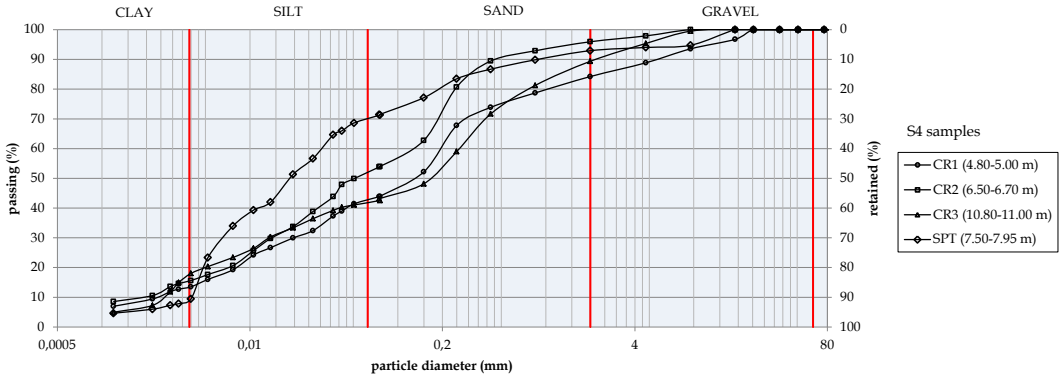

Figure 5.23 Gradation curves for samples collected during borehole S4.

Sample	CR1	CR2	SPT1	CR3
depth (m)	4.80-5.00	6.50-6.70	7.50-7.95	10.80-11.00
γ_S (kN/m³)	26.80	26.77	26.79	26.91
D_{10} (mm)	0.002	0.002	0.004	0.003
D_{60} (mm)	0.194	0.121	0.033	0.261
AASHTO CNR-UNI 10006	N.D.	N.D.	N.D.	N.D.

Table 5.5 Physical parameters from laboratory tests for samples collected in borehole S4.

5.6.5 *Site S5*

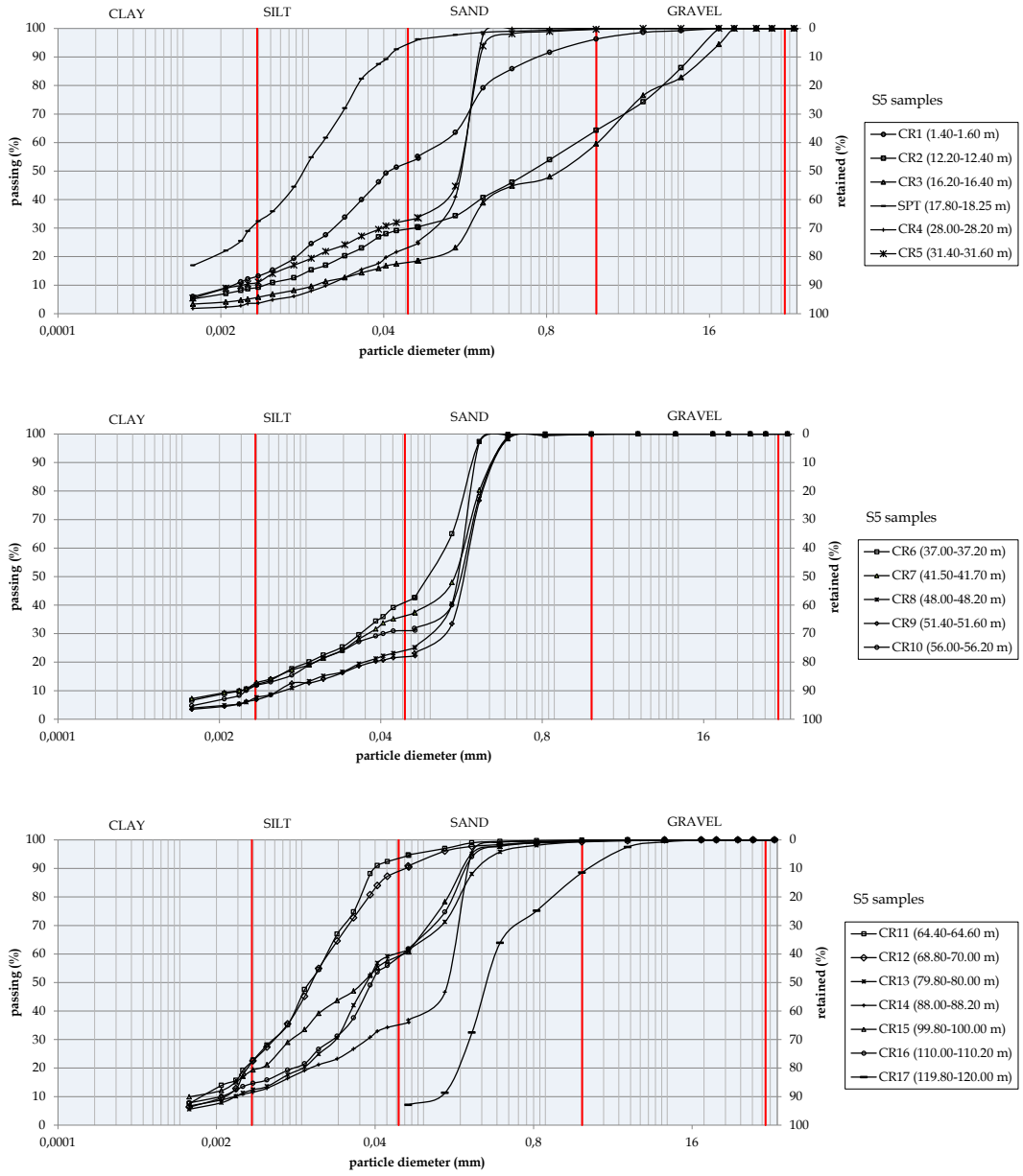

Figure 5.24 Gradation curves for samples collected during borehole S5.

Sample	CR1	CR2	CR3	SPT1	CR4	CR5	CR6
depth (m)	1.40-1.60	12.20-12.40	16.20-16.40	17.80-18.25	28.00-28.20	31.40-31.60	37.00-37.20
γ_S (kN/m³)	26.72	27.24	27.32	26.98	26.72	26.95	26.93
D_{10} (mm)	0.003	0.005	0.012		0.016	0.003	0.003
D_{60} (mm)	0.11	1.402	2.043	0.0013	0.178	0.176	0.128
AASHTO CNR-UNI 10006	N.D.	N.D.	A-1-b	N.D.	N.D.	N.D.	N.D.

Sample	CR7	CR8	CR9	CR10	CR11	CR12
depth (m)	41.50-41.70	48.00-48.20	51.40-51.60	56.00-56.20	64.40-64.60	68.80-70.00
γ_S (kN/m³)	26.85	27.06	27.03	26.79	26.91	26.87
D_{10} (mm)	0.003	0.007	0.007	0.003	0.002	0.003
D_{60} (mm)	0.182	0.179	0.205	0.196	0.017	0.017
AASHTO CNR-UNI 10006	N.D.	N.D.	N.D.	N.D.	N.D.	N.D.

Sample	CR13	CR14	CR15	CR16	CR17
depth (m)	79.80-80.00	88.00-88.20	99.80-100.00	110.00-110.20	119.00-120.00
γ_S (kN/m³)	27.08	26.86	27.07	27.02	
D_{10} (mm)	0.003	0.003	0.001	0.002	0.121
D_{60} (mm)	0.060	0.172	0.070	0.069	0.398
AASHTO CNR-UNI 10006	N.D.	N.D.	A-1-b	A-1-b	A-3

Tables 5.6 Physical parameters from laboratory tests for samples collected in borehole S5.

5.6.6 Resonant Column and Cyclic Torsional Tests

As previously mentioned, for site S5 the particular soil conditions encountered during the drilling operations, essentially marine sands and silty-clay sands, allowed to collect 3 undisturbed samples in the layers showed in Figure 5.25:

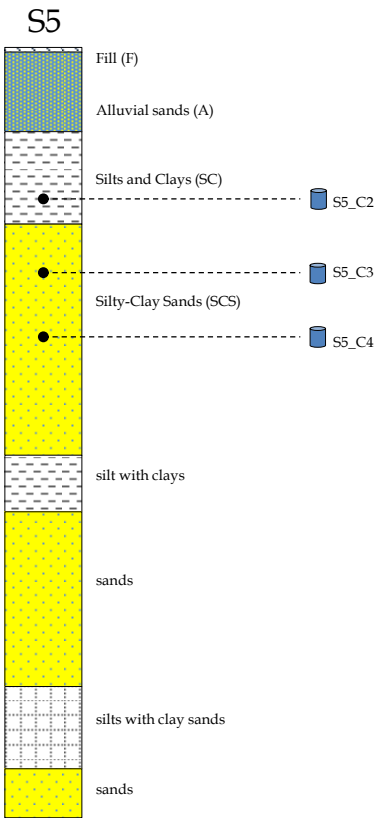

Figure 5.25 Undisturbed samples collected for site S5.

The three aforementioned samples were collected as follows: one from silts and clays (23.45 - 23.95 m from ground level, S5_C2), and two from silty-clay sands (35.00 – 35.55 m and 44.40 - 45.00 m from ground level, S5_C3 and S5_C4). The three undisturbed samples were tested at the Laboratorio Geotecnico (C.N.G. S.r.l, Roma) by resonant column (RC, ASTM D3999-91) and by cyclic torsional shear at 1 Hz (TTC_1 Hz) performed by applying 20 cycles for each strain level. The choice of 1 Hz was made taking into account the resonance frequency observed by seismic noise analysis, around 0.8 – 0.9 Hz observed from seismic noise analysis. The confining pressures were assumed taking into account approximately the vertical effective stresses of the site and considering the hypothetic level and the aquifer level; the so computed values are equal to 400, 350 and 450 kPa for sample S5_C2,

S5_C3 and S5_C4, respectively. The experimental decay curves obtained by laboratory tests are shown in Figure 5.26. The measurable linearity threshold evidences deformations in the range of 0.003%-0.005% for the marine silty-clay sands, and about 0.01% for the marine silts and clays. The measurable volumetric threshold for marine sands ranges from 0.003% to 0.009%, and about 0.005% for sits and clays. For all the three samples, relevant portions of decay curves for high deformation values cannot be measured owing to testing anomalies and samples conditions. In order to obtain a complete decay curve in a broader range of deformation values, an interpolation function was found. Among the various theoretical models available in literature, the Hardin and Drnevich (1972) relation for the silty-clay sands (layer SCS), in the modified form proposed by Yokota et al. (1981) was applied:

$$\frac{G(\gamma)}{G_0} = \frac{1}{1+\alpha\,\gamma\%^{\beta}}$$

The values of $\alpha = 14.184$, and $\beta = 0.967$ were obtained for this sample.

Always on the basis of Hardin and Drnevich (1972a, 1972 b), the damping of layer SCS may be expressed by the relation in the modified form proposed by *Yokota et al.* (1981) as:

$$D(\gamma)\% = \eta \exp\left[-\lambda \frac{G(\gamma)}{G_0}\right]$$

The values $\eta = 81.69$, and $\lambda = 4.214$ were obtained. The founded model for layer SCS is shown in the Figure 5.28.

sample	Depth (m)	Υ_n (kN/m³)	Υ_s (kN/m³)	W	W_{LL}	W_{PL}	PI	e_0	n	S (%)	USCS	AASHTO
S5_C2	23.45-23.95	20.41	26.97	21.22	42.3	27.7	14.7	0.6	37.6	96.2	ML	A-7-6
S5_C3	35.00–35.55	19.34	26.98	29.92	-	-	-	6.81	44.83	100	-	-
S5_C4	44.40–45.00	19.67	26.94	25.9	-	-	-	0.72	42.01	98.16	-	-

Table 5.7. Undisturbed Samples Collected from Borehole S5, Related Physical Characterization and Classification (W natural water content; w_{LL} liquidity limit; W_{PL}, plasticity limit; PI plasticity index; e_0 initial void ratio; n porosity; S percentage saturation).

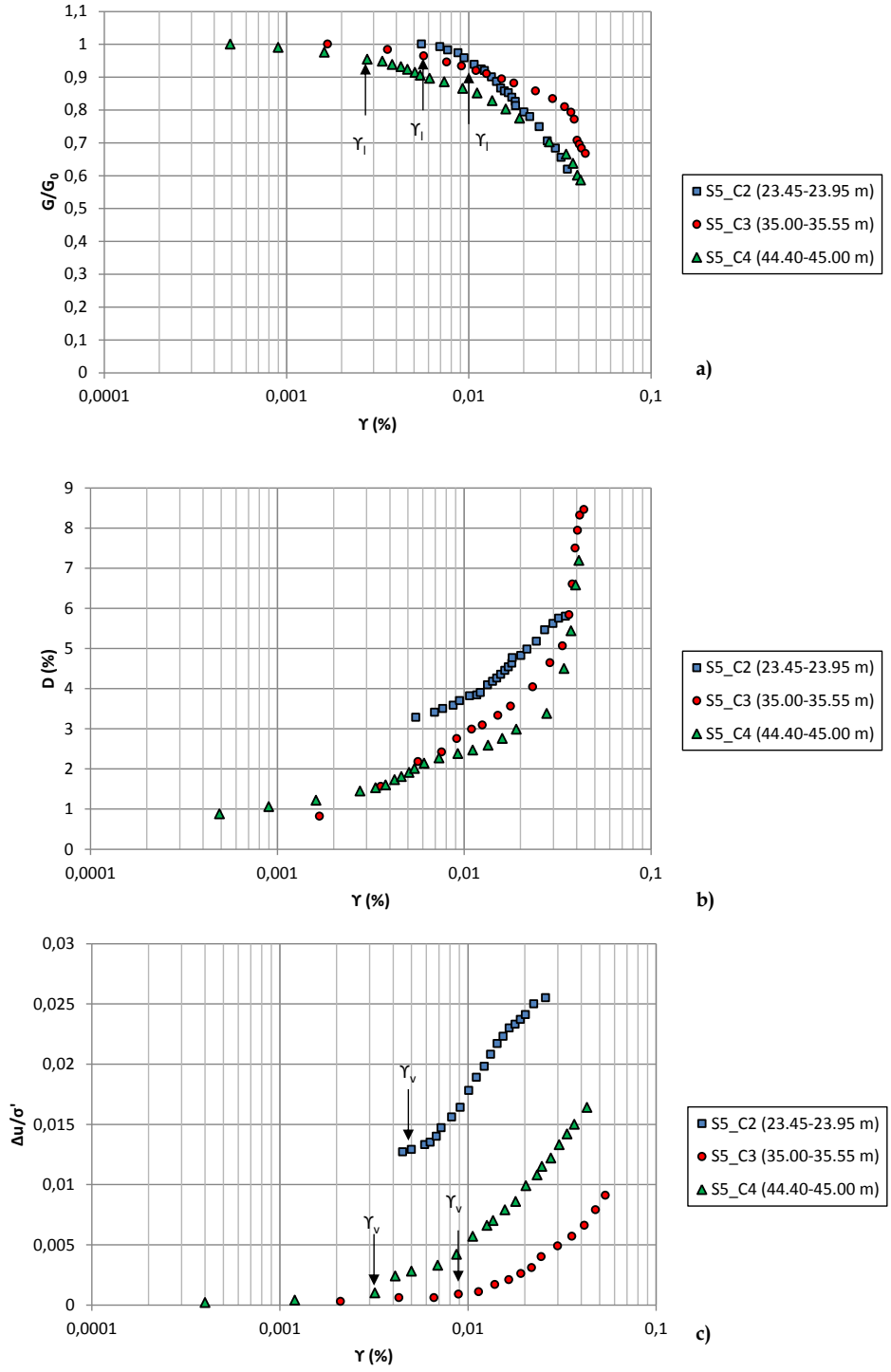

Figure 5.26 Normalized decay curves $G(\gamma)/G_0$ a) and damping curves $D(\gamma)$ b) obtained for undisturbed samples collected from the S5 boreholes undergoing resonant column (RC) tests and cyclic torsional shear (TTC) tests at 1 Hz; the position of the linear thresholds γ_l is shown. c) Normalized excess pore water pressure versus shear strain on samples; volumetric thresholds γ_v are shown.

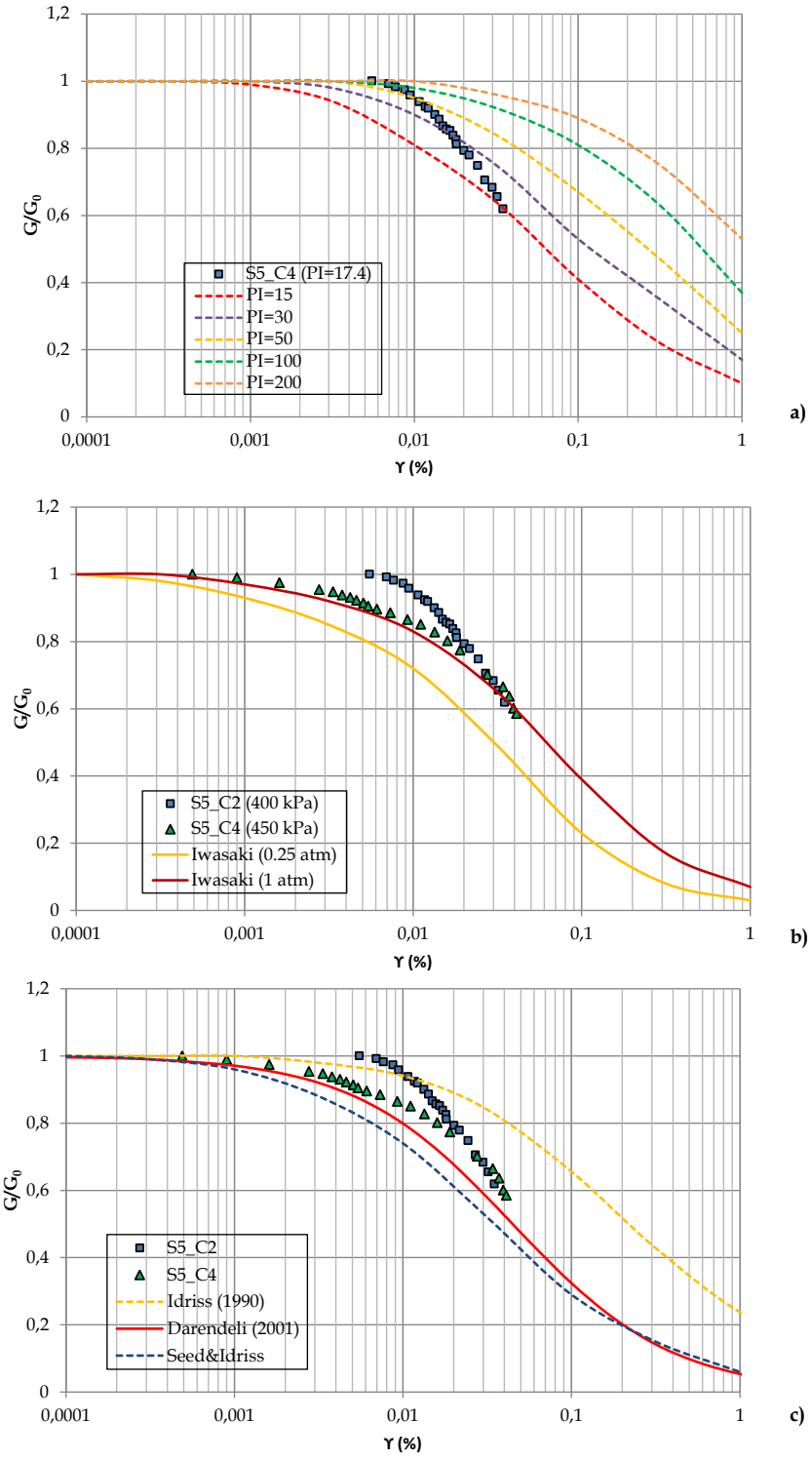

Figure 5.27 Normalized decay curves $G(\gamma)/G_0$ compared to a) Vucetic and Dobry (1991); b) Iwazaki et al. (1976); c) Idriss (1990), Seed and Idriss (1970), Darendeli (2001).

Generally the experimental decay curves $G(\gamma)/G_0$ (Figure 5.27) are not in agreement with the decay curves available in literature (Vucetic and Dobry, 1991; Idriss, 1990; Darendeli, 2001). The observed differences concern not only the shape of the curves, but also the values of the linearity threshold. In particular, a marked inconsistency (curve shape and threshold values, Figure 5.27a) is noted with respect to the curves proposed by Vucetic and Dobry [1991]. However, sample S5_C4 responded to dynamic tests with decay curve $G(\gamma)/G_0$ that is very similar to those reported by Iwasaki (1976).

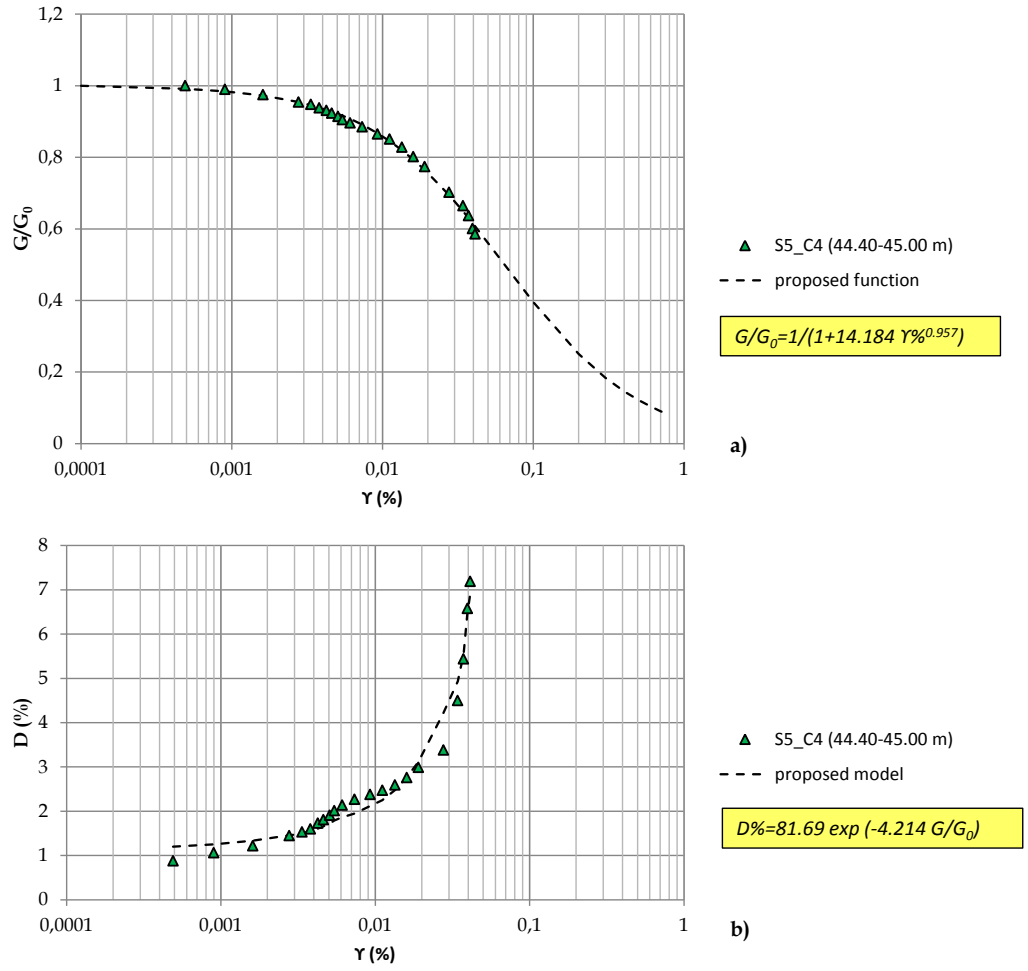

Figure 5.28 Comparison between decay curves $G(\gamma)/G_0$ a) and damping curves $D(\gamma)$ b) obtained from resonant column tests for sample S5_C4 and proposed models according the Hardin and Drevich [1972]. The proposed model has been evaluated through least squared method using software MATHEMATICA (www.wolfram.com/mathematica/).

5.7 Testing Liquefaction Risk

The evaluation of the liquefaction resistance of soils is an important step in many geotechnical investigations in earthquake prone regions. At the beginning of the MASSIMO Project the aforementioned evaluation was not one of the main purpose of the study. Besides Italian Regions Calabria region has been affected during last years by several liquefaction phenomena, especially in its Central and Southern part (see the new database from Galli, 2000). Considering geotechnical data collected during boreholes and laboratory tests, especially down-hole tests, a preliminary study for liquefaction resistance was made in the sites where boreholes were drilled.

In order to evaluate a preliminary test on the liquefaction risk use was made through the simplified procedure proposed by Andrus and Stokoe (2000), which gives as result the factor of safety vs depth. The evaluation procedure requires the calculation of three parameters:

(1) level of cyclic loading on the soil caused by the earthquake, expressed as a cyclic stress ratio *CSR*;

(2) stiffness of the soil, expressed as an overburden stress-corrected shear-wave velocity Vs;

(3) resistance of the soil to liquefaction, expressed as a cyclic resistance ratio *CRR*.

A typical way to quantify the potential for liquefaction is in terms of a factor of safety, defined by:

$$FS = \frac{CRR}{CSR}$$

As previously described liquefaction is predicted to occur when $FS < 1$, and liquefaction is predicted not to occur when $FS > 1$.

The choice to perform such preliminary study was motivated taking into account recommendations of D.M.14.01.2008; following these recommendations, the liquefaction can be excluded if is tested at least one of the following conditions:

1. *Earthquake magnitude* < *5*
2. *Maximum accelerations on the ground campaign in free-field conditions* < *0.1 g*

3. *Seasonal average depth of aquifer level more than 15 m from ground level campaign*

4. *Sands with $(N_1)_{60}$>30, or q_{c1}>180*

5. *Particle size distribution at fixed external limits (see Figure below):*

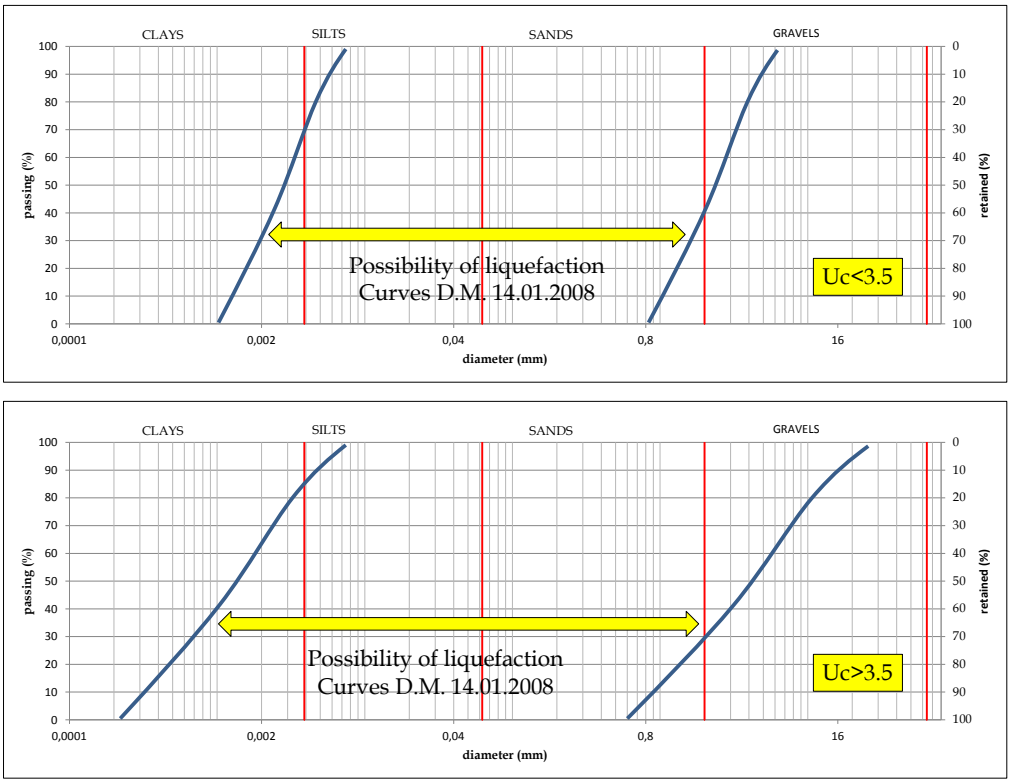

Figure 5.29 Limits in the gradation curves where liquefaction can occur.

For all the study sites magnitude Mw = 7.29 was chosen, introduced considering the 729 seismogenetic zone, valid for the city of Cosenza according to http://zonesismiche.mi.ingv.it/ (Meletti and Valensise, 2004). The ground peak acceleration PGA at ground surface used for each site are expressed in Table 5.8; every value was obtained by the product of the design peak ground acceleration a_g for stiff ground (type of soil) and a soil factor S, which depends on the subsoil stiffness, namely the stratigraphic amplification factor SS, and on the topography, defined by the topographic amplification factor ST, according to the Italian Building Code (NTC 2008).

The position of the aquifer level for sites S1-S4 was evaluated taking into account geological criteria, such as distance from Crati and Busento rivers, and particular conditions of the sampled soils. The evaluated aquifer levels depth are shown in the Table below.

site	soil type	PGA	aquifer level (b. g. l.)
S1	E	0.346	5
S2	C	0.354	5
S3	B	0.308	11
S4	B	0.308	3
S5	S2	0.354	11

Table 5.8. Data for testing liquefaction risk at study sites

In order to obtain the actual value of the aquifer level for site S5, an ERT (Electrical Resistivity Tomography) was performed in the area shown in the Figure 5.30 below, more in detail in the same direction where 1D-active and passive arrays were performed. The analysis was possible considering the logistic of the area.

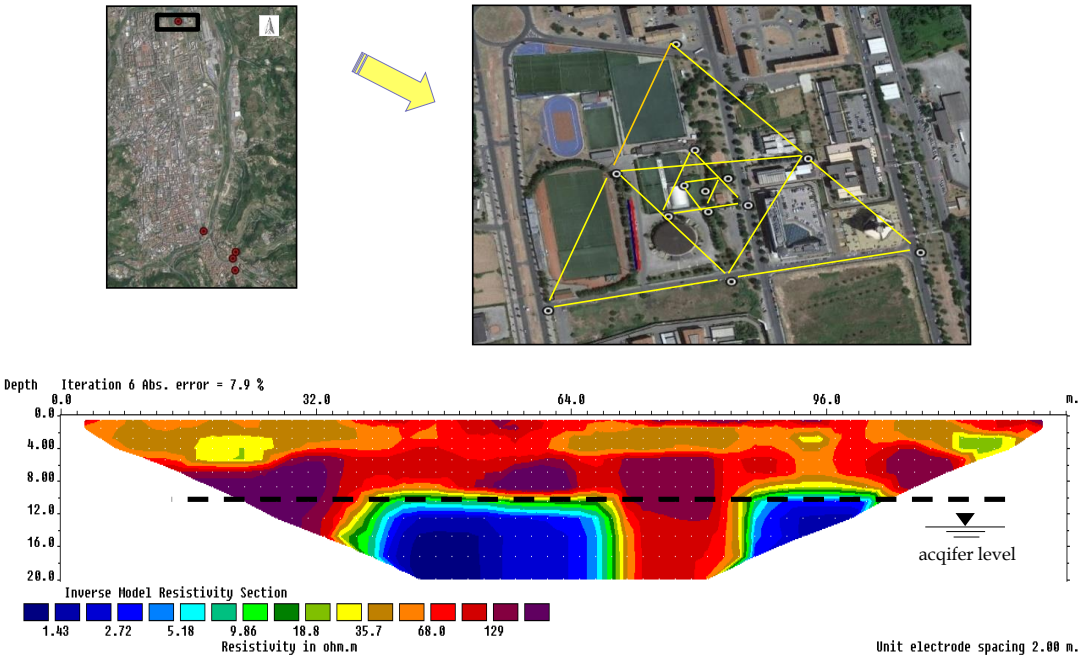

Figure 5.30 ERT performed in the area of site S5.

The ERT was realized using 64 electrodes with inter-space of 3m. Considering the result shown in the previous Figure, a low resistivity value was encountered at about 11 m below ground level. Taking also into account logistic considerations we the aforementioned depth was assumed for the aquifer level.

The gradation curves for samples collected during boreholes are shown in the Figures below for the first layers; for each sites limits curves in which liquefaction can occurs are shown:

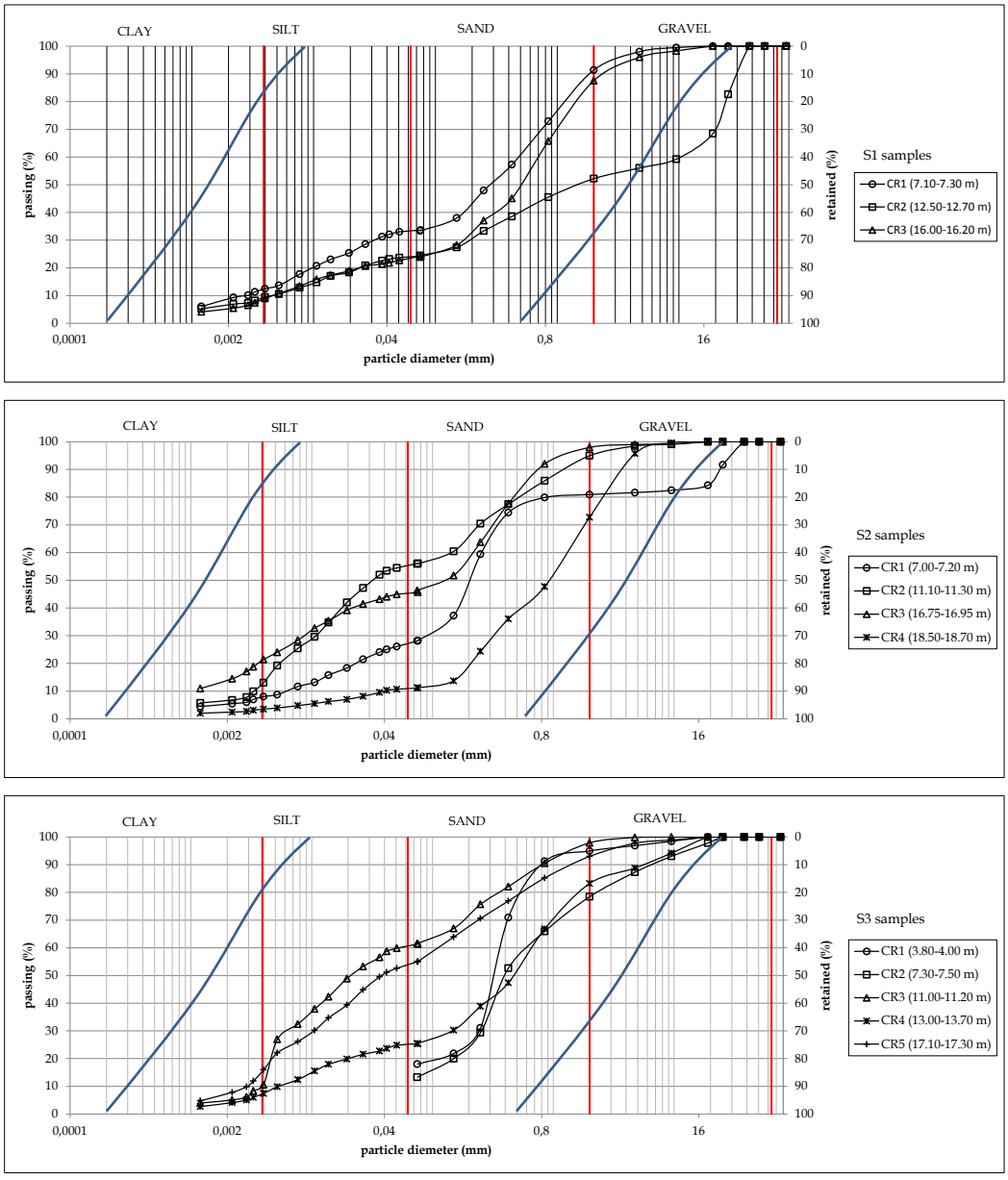

Figure 5.31 Gradation curves for samples collected during boreholes S1, S2 and S3 ($U_C > 3.5$ for all the samples); the continuous curves in blue represent the interval in which liquefaction can occur following D.M.14.01.2008.

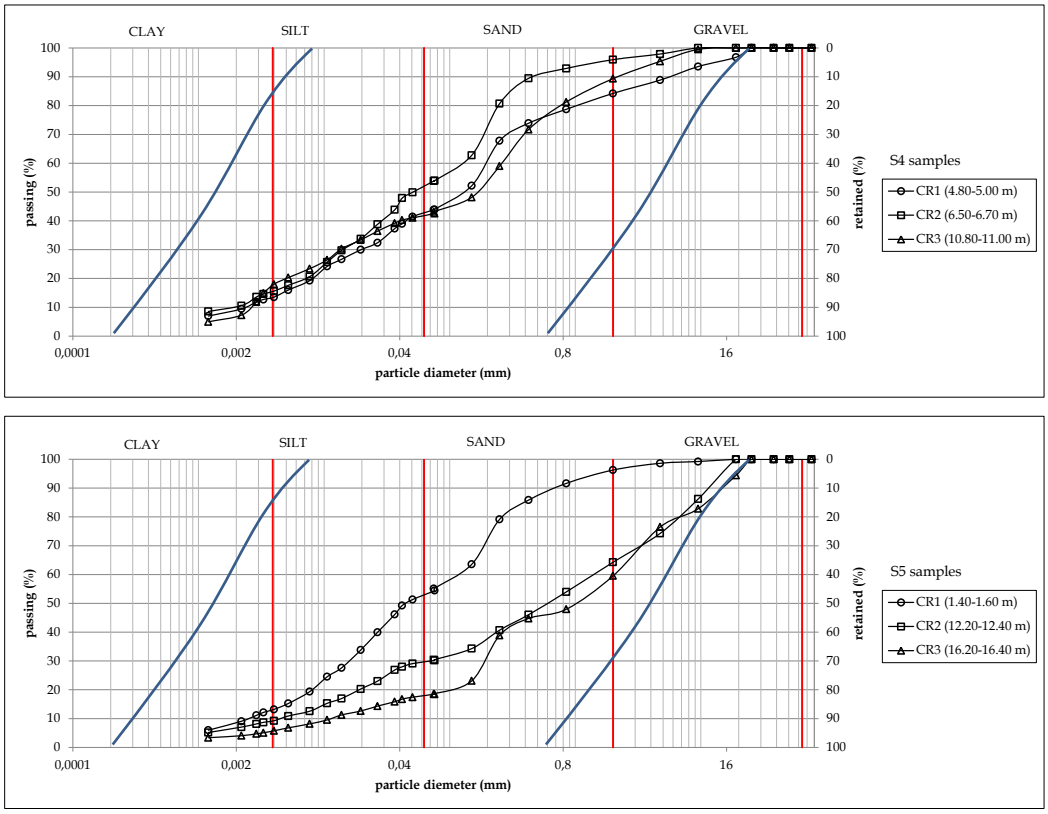

Figure 5.32 Gradation curves for samples collected during boreholes S4 and S5 ($U_C > 3.5$ for all the samples); the continuous curves in blue represent the interval in which liquefaction can occur following D.M.14.01.2008.

Though during drilling operations it was not possible to perform SPT tests for all the layers under analysis, due to the particular conditions of the soils, testing liquefaction risk was performed anyway. The results for the evaluation of the factor of safety are shown in Figure 5.33; factor of safety were evaluated starting from the position of the aquifer level, varying for each site, down to 20 m below ground level, depth beyond which liquefaction phenomena have not been historically observed; exception was for site S4 where the contact between sedimentary covers and the metamorphic bedrock was located at about 16 m below ground level.

Considering the results showed in the following Figures, all the study sites look to be save from liquefaction risk.

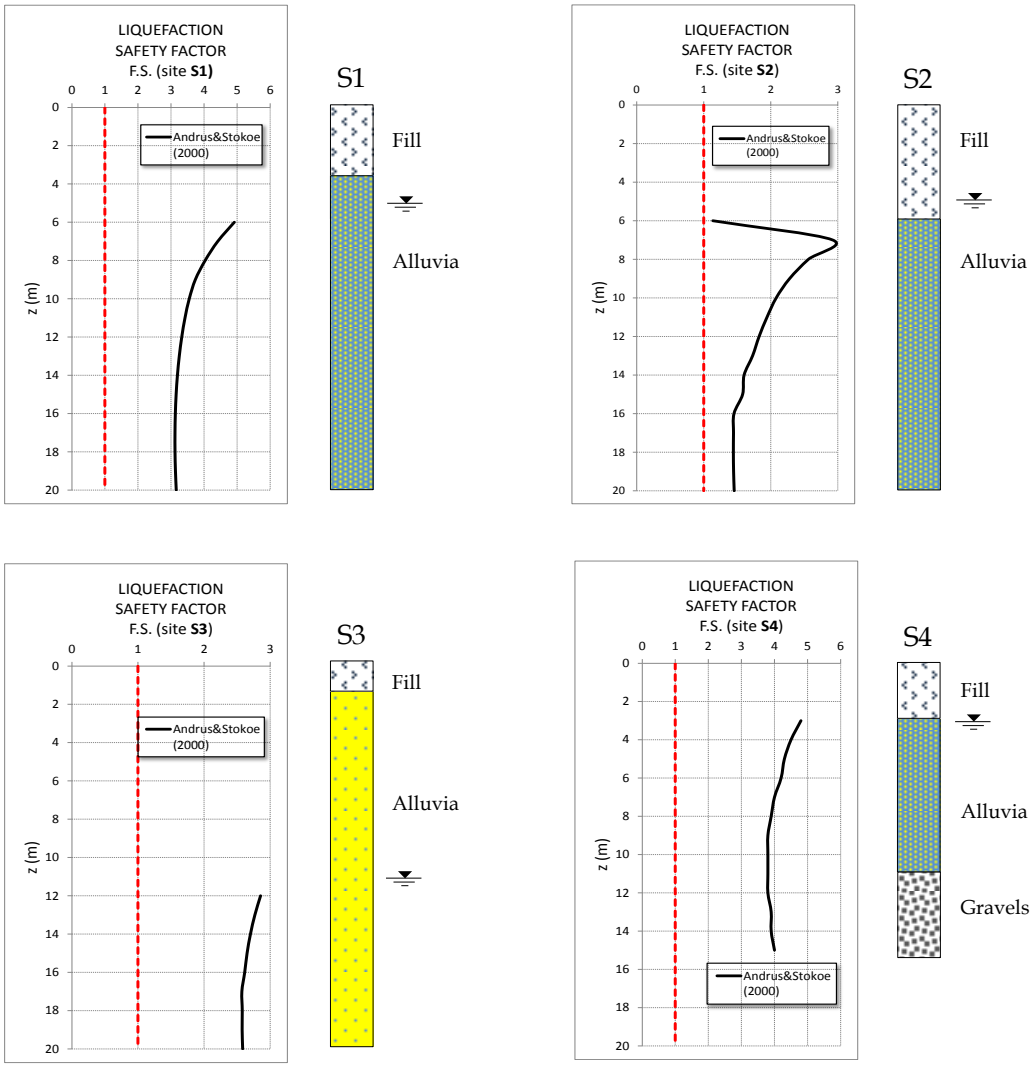

Figure 5.33 Factor of safety vs depth for sites S1-S5.

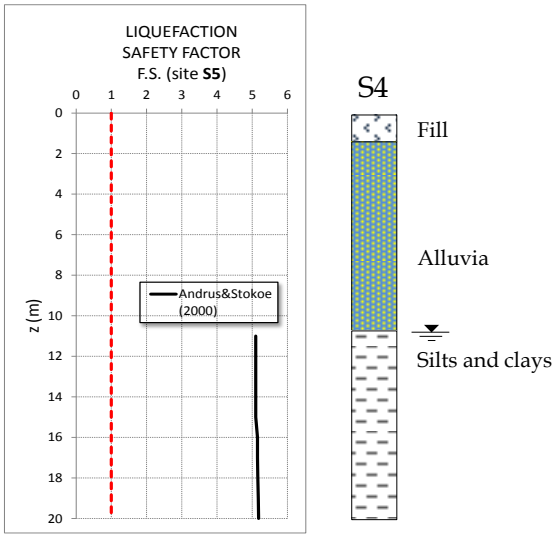

Figure 5.34 Factor of safety vs depth for site S5.

5.8 1D Model of Seismic Local Response at Site S5

A 1D modelling was performed using the software EERA (free download at http://www.ce.memphis.edu/7137/eera.htm) in order to evaluate the seismic local response at site S5. The 1D model was derived considering down-hole tests and inversion of seismic noise data which also validated the plane and parallel approximation for the near surface geology of the area.

As mentioned in the introduction, the city of Cosenza has been affected by many earthquakes; in order to characterize the historical seismicity of the city of Cosenza we consulted the "Catalogue of strong earthquakes in Italy from 491 BC to 1997" - ***CFTI***, "***P***arametric ***C***atalogue of ***I***talian earthquakes" (http://storing.ingv.it/cfti4med/ - CPTI11, "Italian macroseismic database"(http://emidius.mi.ingv.it/CPTI11/) - DBMI11 (http://emidius.mi.ingv.it/DBMI11/)" ***C***atalogue of the ***I***talian ***S***eismicity, 1981 to 2002" - CSI 1.1. Another important means used to characterize the seismicity of the Crati Basin is the ***DISS***, (***D***atabase of ***I***ndividual ***S***eismogenic ***S***ources - INGV, http://diss.rm.ingv.it/diss/) through which three individual seismogenetic sources have been defined in the study area: the Dipignano source, the Luzzi source and the Castiglion Cosentino source.

In order to quantify the seismic response of site S5, seismic inputs were applied to the metamorphic bedrock (*sbg*). For this, surface model previously described was linked to a crustal model used for the evaluation of three synthetic reference earthquakes (Figure 5.34); for further information see Tiberti et al., (2013). These inputs refer to:

(i) an event of magnitude Ms = 7.0 with epicentral distance of 5.3 km to S5 site, and having a PGA of 0.46g, which can be regarded as representative of the maximum expected seismicity in the urban area of Cosenza;

(ii) an event of magnitude Ms = 6.0 with epicentral distance of 0.71 km from the study area having a PGA of 0.31g;

(iii) an event of magnitude 5.0 with epicentral distance of 18 km from S5 having a PGA of 0.053g. The M6 earthquake can be representative of the Castiglion Cosentino source, while the earthquakes M5 and M7 can be regarded as representative of the Dipignano source.

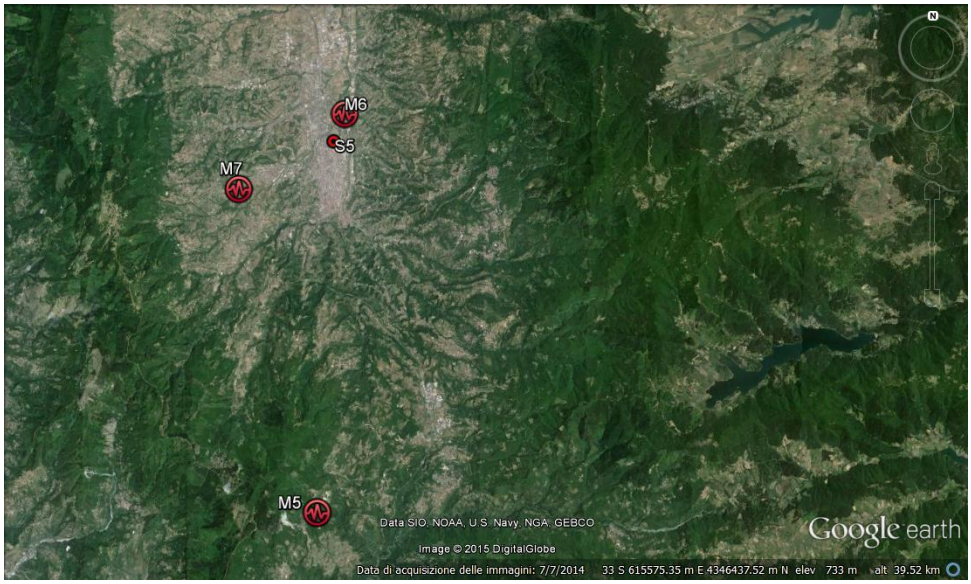

Figure 5.35 Localization of the seismic epicentres used for 1D model at Site S5.

The amplification function A(f) was evaluated in the 1–6 Hz frequency range; all the seismic inputs (both considering the E-W and N-S components of the synthetics) were applied at the metamorphic bedrock (Table 5.3, Figure 5.36b), and the A(f) function was computed as out-crop spectral ratio.

In order to quantify non-linear effects induced, two different normalized decay curves $G(\gamma)/G_0$ and damping curves $D(\gamma)$ were applied to level SCS (silty-clay sands), respectively the founded model obtained by interpolating function (Figure 5.28) and the Idriss model for sands (1990). The results of 1D modelling in the case of synthetic seismograms are shown in Figures 5.37 and 5.39. The amplification functions exceeds the values of 2 at about 0.8 Hz (first resonance frequency) and other frequency values, for both the aforementioned models. A good agreement is observed with the H/V peak at 0.8 Hz observed by seismic noise analysis.

Vertical deformation profiles versus depth (Figures 5.38 and 5.40) show that in the cases of PGA 0.3g and 0.46g, referred to magnitudes of M6 and M7, corresponding to epicentral distances of 0.71 km and 5.38 km, respectively, linear and plastic conditions are reached for all the layers where Laboratory tests were performed in both seismic inputs. In the case of PGA of 0.053g, referred to an earthquake of magnitude M5, corresponding to an epicentral distance of 18 km, linear and volumetric thresholds determined by laboratory tests are exceeded only in correspondence of S5_C4 sample considering both seismic inputs.

level	group	lithology	thickness (m)	Vs (m/s)	density (kg/m³)	Damping (%)
I	F	fill	5	300	1800	5
II	A	alluvia	8	460	1850	5
III	SC	silts and clays	17	350	1800	5
IV	SCS	silty-clay sands	40	540	1850	1
V	S1	sands	50	620	1900	1
VI	S2	sands	90	920	1900	1
VII	*sbg*	altered bedrock	30	1400	2300	0.4
VII	sbg	bedrock	4740	2490	2400	0.4

Table 5.9 Geophysical Stratigraphy and Dynamic Characteristics for site S5 used for 1D modelling. The yellow box indicates where proposed model and Idriss model for decay curve and damping were applied.

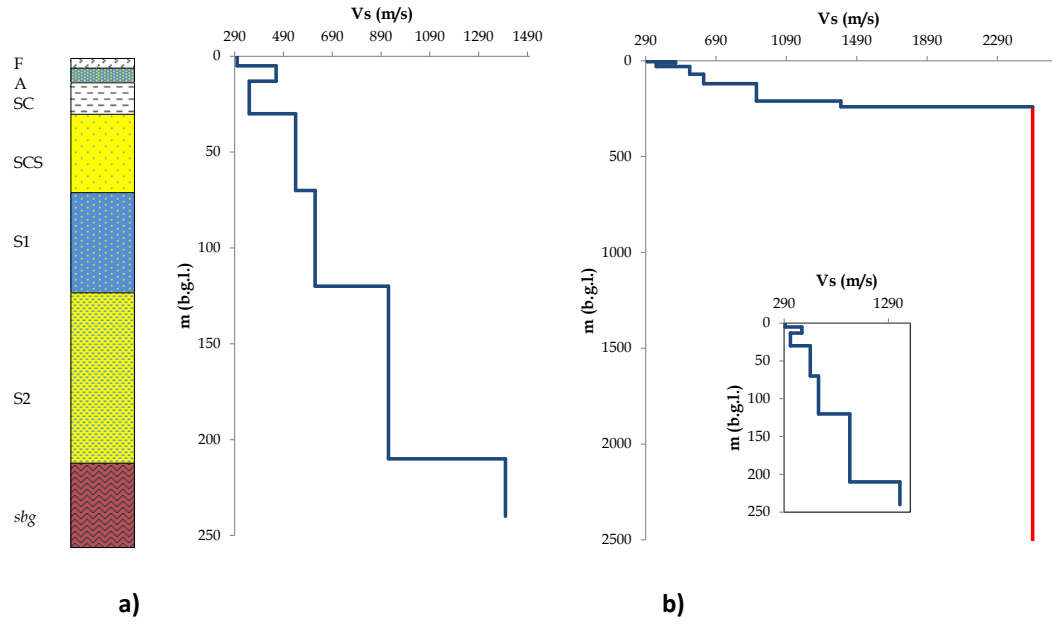

Figure 5.36) a) Surface Vs profile obtained by surface wave inversion and geological interpretation; b) Vs profile used for 1D modelling; the box shows a detail of the surface profile on left.

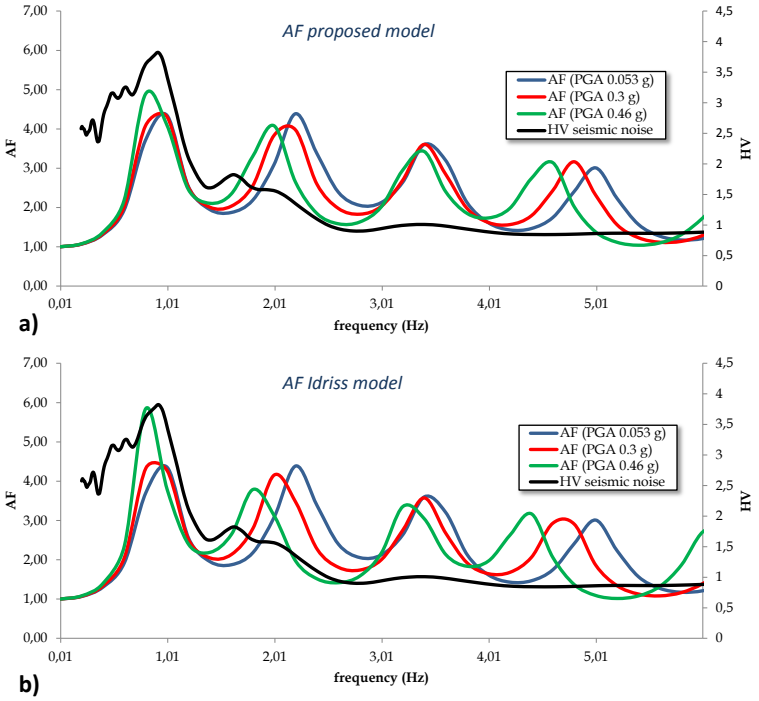

Figure 5.37 Amplification functions obtained by 1D numerical modelling of the subsoil profile in Table 2 applying the E-W component of the seismic input, assuming proposed function for SCS layer and Idriss model; comparison with the H/V function observed by seismic noise.

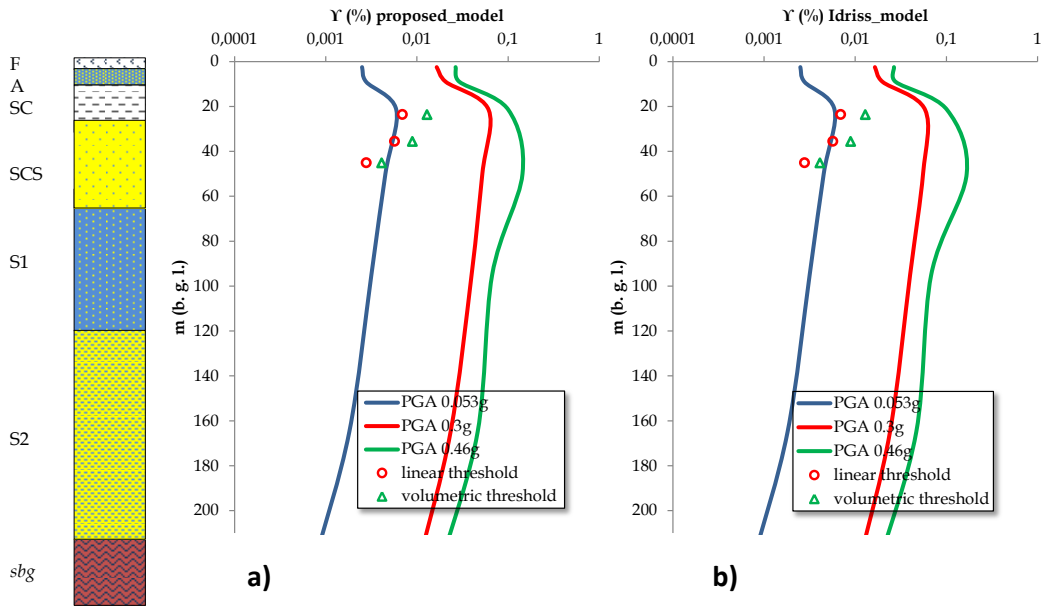

Figure 5.38 Maximum shear strain vs depth resulting from 1D numerical modelling of subsoil profiles in Table 5.9 in the case of E-W component of the synthetics; a) left proposed model for layer SCS; b) right Idriss model for layer SCS.

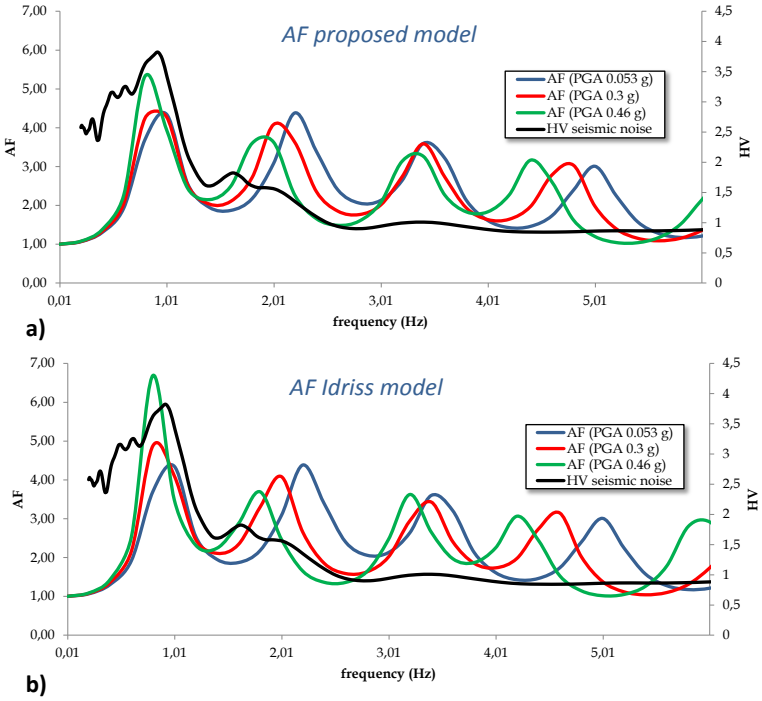

Figure 5.39 Amplification functions obtained by 1D numerical modelling of the subsoil profile in Table 2 applying the N-S component of the seismic input, assuming proposed function for SCS layer and Idriss model; comparison with the H/V function observed by seismic noise.

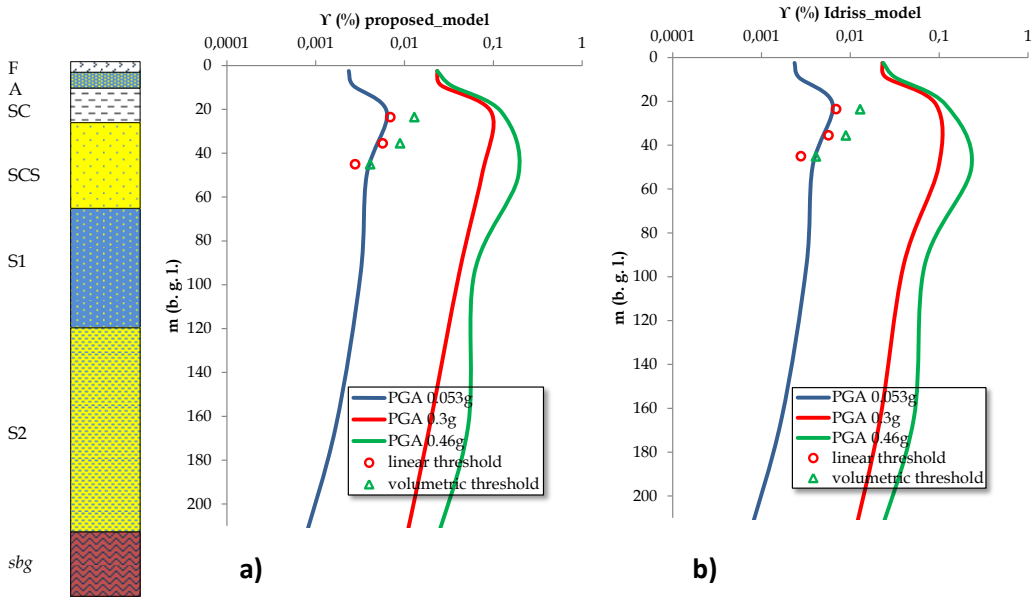

Figure 5.40 Maximum shear strain vs depth resulting from 1D numerical modelling of subsoil profiles in Table 5.9 in the case of N-S component of the synthetics; a) left proposed model for layer SCS; b) right Idriss model for layer SCS.

6. CONCLUSIVE REMARKS

A comprehensive study was conducted on alluvial and marine sedimentary covers in area of the city of Cosenza, in order to give new data for potential assessing of ground motion in this urban area. In this Section we summarize the results performed during this study.

6.1 Ambient Vibration Analysis: H/V

Use of the Nakamura technique allowed to identify the resonance frequencies for the study sites: from 6 Hz to 4.2-1.2 Hz in the area of the Test Site, 1.2 Hz for piazza Haring, 0.8 Hz for Site S5, 0.9 Hz for Site Agriturismo, 0.4 Hz for Site B&B and 0.3 Hz for Site Arcavacata. The results revealed a complex dynamic response for the area of the Test Site, probably referred to an high heterogeneity in the near surface geology and different metamorphic bedrock depths; in the case of the other Sites, the resonance frequencies indicate a probable deepening of the contact between sedimentary covers and metamorphic bedrock from the area of the Test Site to North direction (Site Arcavacata).

6.2 Boreholes

The results of seismic noise analysis allowed to identify positions where perform some boreholes in the study Sites. Three boreholes (S2, S3 and S4) were drilled in the area of the Test Site, in order to obtain the actual stratigraphy and justify the complex dynamic response of the area, and one borehole (S1) was drilled at the beginning of the Crati Valley, inside a private property, with the aim to identify possible lateral discontinuities and to install a permanent seismic sensor; finally, another borehole (S5) was drilled 1 km northern away from Site of piazza Haring, in order to obtain a reference stratigraphy of the High Crati Valley.

In the area of the Test Site the position of the top of the metamorphic bedrock was encountered at different depths, between 20-40 m below the ground level, whereas for Site S5, until the depth of 120 m below the ground level, the aforementioned contact was not encountered, revealing a deeper position.

6.3 *Ambient Vibrations Analysis: Seismic Arrays*

Use of seismic arrays allowed to obtain a complete Vs velocity profile for site S5, able to reach the depth of the metamorphic bedrock forming the basement of the Crati Basin and for Site of piazza Haring. The shear-wave velocity profile for Site S5 revealed a good agreement with the one obtained by down-hole Test for the first 60 m. The same analysis was performed for piazza Haring Site.

6.4 *Geological Reconstruction of the Contact Sedimentary Covers-Metamorphic Bedrok*

The results obtained by boreholes and seismic noise analysis (inversion of dispersion curve) allowed to realize two simple geological model for the area of the Test Site and for the High Crati Valley. In the first (Test Site area) case a very critical position was identified for the Test Site of San Agostino, located between two different lithologies, marine sands and alluvial deposits; this result represents a fundamental data for engineers and architects responsible for safety of the building with the aim to perform any study involving the interaction between soil and structure. A preliminary study performed by Gaudiosi et al. (2015) revealed that the critical position of the Test Site can generate possible differential oscillation modes in the structure. In the second case (High Crati Valley area) a deepening of the contact between sedimentary covers and top of the metamorphic bedrock was confirmed from the area of the Test Site (S1) to Site S5.

6.5 *Laboratory Tests: Testing Liquefaction Risk*

The amount of data provided during boreholes, in particular grain size analysis on sampled soils, supplied a useful tool for a preliminary liquefaction assessment of the study area. Testing liquefaction risk following the simplified procedure proposed by Andrus and Stokoe (2000), shows that none of the study sites is susceptible to liquefy. The study for potential liquefaction risk was performed even if all critical conditions of NTC 2008 were not completely satisfied; in fact, a more detailed study for potential liquefaction risk needs geotechnical analysis such SPT (Standard Penetration Test) and/or CPT (Cone Penetration Test) that were not possible to perform in the study sites considering the particular conditions of the soils encountered during boreholes.

6.6 Laboratory Tests: Resonant Column and Cyclic Torsional Shear Tests

The particular soil conditions encountered during the drilling operations for Site S5 allowed to collect three undisturbed samples in three distinct layer. The samples were tested by RC and TTC at 1 Hz in order to obtain decay curves for shear-modulus $G(\gamma)/G_0$ and damping $D(\gamma)$ and identify possible linear and volumetric thresholds. The theoretical model of Hardin and Drnevich, in the modified form after Yokota et al. applied for sample S5_C4, allowed to obtain a decay curve in a broader range of deformation values.

6.7 1D Modelling

Considering the shear-wave velocity profile obtained, and decay curves $G(\gamma)/G_0$ and damping curves $D(\gamma)$ obtained for layer SCS in site S5, simulations were performed with the software EERA in order to reconstruct vertical profiles of the maximum shear deformations that could be obtained in the sedimentary covers in response of the maximum expected earthquakes for the city of Cosenza. The 1D modelling, obtained for the site S5, located in central part of the High Crati Valley, reveals that critical non-linear effects can be induced on the aforementioned layer of silty-clay sands (level SCS); furthermore, good agreement with the resonance frequency observed by seismic noise analysis was observed, validating the dynamic-stratigraphic model previously obtained.

6.8 Future Research

All the results obtained by the present work represents the basics for any study involving the interaction between soil and structures. For more detailed studies another fundamental data are required:

1. Identification of positions where perform new boreholes, in order to refine the geological reconstruction of the Test Site area and for the High Crati Valley.

2. Perform, where possible, SPT and CPT in specific geological layers, in order to obtain fundamental data to assess new potential liquefaction risk using different simplified procedures and more detailed techniques.

3. Collect, where possible, new undisturbed samples, in order to obtain by RC and TTC tests more accurate decay curves for shear-modulus and damping.

Recently, the installation of a permanent sensor down to the drilling depth in Site S1 (see Figure below) and also in Site S5 will give the possibility to record actual seismic input at the top of the metamorphic bedrock of the Crati Basin. Furthermore, installation of permanent sensors inside the Test Site will aim to identify the preliminary seismic response of the masonry building. The use actual seismic input to the metamorphic bedrock, and more detailed decay curves, will allow to perform new 1D simulations and compare the previous models obtained.

Figure 5.41 Installation of the borehole sensor at the top of the metamorphic bedrock in Site S5 (march 2014).

ACKNOWLEDGMENTS

I would like to express my gratitude to all the people who collaborated with me during my PhD, and who made it possible.

First of all I would like to thank my supervisor, Prof. Giuseppe Della Monica, for his encouragement to undertake his first PhD doctorate and for the constant trust he put in me for my work.

At the same time, I warmly want to express my gratitude to Dr. Arrigo Caserta: he has been a scientific guide and a friend for me for four years, during which we have been working side-by-side, always together in the field work, where he offered me in particular his personal experience.

A special thanks to the researchers of INGV who helped and encouraged me during my work: Dott. Giuliano Milana, Dott. Aladino Govoni, Dott. Antonella Megna, Dott. Fabrizio Cara.

To all people of the "Sciences Group": Francesco Basile, Giorgia Carlucci, Elena Capentieri: I will never forget you.

I am very grateful with Dott. Marcello Martinelli and his Group of CNG (Rome), for his constant help and friendship.

To my friend Simone Racano, a special geologist and friend, always ready to help me.

To Prof. Anastassios Tassos Kotsakis, a very scientific guide and master in every moments.

To Prof. Maurizio Mariottini, a great Master, a second father, a big friend, always ready to comfort me. I'll never forget all you did for me…

How to not remember Ares and Simone, my second brothers, my hearth and my mind, I would never think my life without them…

Le mie ultime parole vanno poi alle persone a cui devo tutto, la possibilità di affrontare non una, ma due lauree, il continuo amore e affetto che oggigiorno sono sempre più rari anche da coloro che sono sempre con noi …

semplicemente

Papà e Mamma

BIBLIOGRAPHY

AKI K., Richards P.G. (1980). Quantitative seismology: theory and methods – 2 vol., Freeman, S. Francisco.

AL-HUSSEINI, Glover, J. B. and Barley, B. J. (1981). Dispersion patterns of the ground-roll in eastern Saudi Arabia. *Geophysics* 46, no. 2, 121–137.

ANDRUS, R.D. and Stokoe, K. H., II, (2000). Liquefaction resistance of soils from shear-wave velocity. *J. Geotech. Geoenviron. Eng.*, ASCE. 126(11), 1015-1025.

ANSAL, A., Kurtulus, A., Tonuk, G. (2010). Seismic microzonation and earthquake damage scenarios for urban areas. *Soil Dyn Earthq Eng* 30:1319–1328.

ASTEN, M. W., and Henstridge, J. D. (1984). Array estimators and the use of microseisms for reconnaissance of sedimentary basins. *Geophysics*, 49, 1828–1837.

ASTM D424-54 (1971). Standard Method of Test for Plastic Limit (Withdrawn 1982).

ASTM D422-63 (2007). Standard Test Method for Particle-Size Analysis of Soils.

ASTM D4015-07 (2007). Standard test methods for the determination of the modulus and damping of soils by the resonant-column method. ASTM International, West Conshohocken, PA.

ASTM D1586-84 (2014). Standard Test Method for Standard Penetration Test (SPT) and Split-Barrel Sampling of Soils.

ASTM D7400-08 (2008). Standard tests methods for down-hole seismic testing. ASTM International, West Conshohocken, PA.

BARD P. Y., (1998). Microtremor measurements: A tool for site effect estimation? *Proceeding of the Second International Symposium on the Effects of Surface Geology on Seismic Motion.* Yokohama, Japan. **3** 1251-1279.

BONNEFOIT-CLAUDET, S. (2004). Nature du Bruit du Fond Sismique: Implications pour les Études des Effets de Site, Doctoral Thesis, Observatoire de Grenoble et Laboratoire de Géophysique Interne et de Tectonophysique, Université Joseph-Fourier Grenoble I.

BONNEFOIT-CLAUDET S., Cotton F., Bard P.-T., (2006). The nature of noise wavefield and its applications for site effects studies. A literature review. *Earth Sciences Review*.

BOORE, D. M., and Brown L. T. (1998). Comparing shear-wave velocity in profiles from inversion of surface-wave phase velocities with downhole measurements: systematic differences between the CXW method and downhole measurements at six USC strong-motion sites. *Seism. Res. Lett.*, **69**, 222-229.

BOZZANO, F., Caserta, A., Govoni, A., Marra, F., Martino, S. (2008). Static and dynamic characterization of alluvial deposits in the Tiber River Valley: New data for assessing potential ground motion in the City of Rome. *Journal of Geophysical Research*, 113.

CAPON, J. (1969). High-resolution frequency-wavenumber spectrum analysis, in the *Proc. IEEE*, 57 (8), 1408-1418.

CAPON J. (1969). High-Resolution Frequency-Wavenumber Spectrum Analysis, *Proceeding of the IEEE*, **57** n.8, 1408-1418.

CAROBENE, L., and A. V. Damiani (1985) Tettonica e sedimentazione pleistocenica nella media valle del F. Crati. Area tra il T. Pescara ed il F. Mucone (Calabria). *Boll. Soc. Geol. It.*, 104, 93-114.

CASSA PER LE OPERE STRAORDINARIE DI PUBBLICO INTERESSE NELL'ITALIA MERIDIONALE (CASSA PER IL MEZZOGIORNO), 1977, Progetto Speciale 26: Studio organico delle risorse idriche sotterranee della Calabria.

CELICO P. B., Monacelli G., Tranfaglia G., (2000). Carta idrogeologica dell'Italia Meridionale, scala 1:250.000. Progr. INTERREG IIC, Presidenza del Consiglio dei Ministri - Dipartimento per i Servizi Tecnici Nazionali & Università degli Studi di Napoli "Federico II"- Dipartimento di Geofisica e Vulcanologia. Roma.

CRESPELLANI, T., and Facciorusso, J. (2010). Dinamica dei terreni per le applicazioni sismiche. Dario Flaccovio Ed.

DARENDELI, M. B. (2001). Development of a new family of normalized modulus reduction and material damping curves. Austin, Texas: The University of Texas.

DI FRANCESCO, R. Lesioni degli edifici, Applicazioni di geotecnica e geofisica nell'analisi dei cedimenti delle fondazioni, HOEPLI.

DI GIULIO, G., Cornou, C., Ohrberger, M., Wathelet, M., Rovelli, A., (2006). Deriving Wavefield Characteristics and Shear-Velocity Profiles from Two-Dimensional Small-Aperture Arrays Analysis of Ambient Vibrations in a Small-Size Alluvial Basin, Colfiorito, Italy. *Bulletin of the Seismological Society of America*, 96, No. 5, pp. 1915–1933.

DOBRY, R., Stokoe, K. H., II, Ladd, R. S., and Youd, T. L. (1981). Liquefaction susceptibility from S-wave velocity, *Proc., ASCE Nat. Convention, In Situ Tests to Evaluate Liquefaction Susceptibility*, ASCE, New York.

FÄH, D., Ruttener, E., Noack, T., Kruspan, P. (1997). Microzonation of the city of Basel. *J. Seismol*. 1:87–102.

FÄH D., Kind F., Giardini D., (2001). A Theoretical Investigation of Average H/V Ratios, *Geophys. J. Int.*, 145, 535–549.

FACCIOLI, E., (1999). The Catania project: studies for an earthquake damage scenario. *J Seismol*. (special issue).

FOTI, S., Lai, G. C., Rix, G. J., and Strobbia, C. (2015). Surface wave methods for near surface site characterization, CRC Press.

FOTI, S. (2000). Multistation Methods for Geotechnical Characterization using Surface Waves. *PhD thesis*, Politecnico di Torino, Italy.

FOTI, S., Sambuelli, L., Socco, L. V., and C Strobbia, C. (2003). Experiments of joint acquisition of seismic refraction and surface wave data. *Near Surface Geophysics*, 1:119–129.

FRIGO, M. and Johnson, S. (2005). The Design and Implementation of FFTW3. *Proceedings of the IEEE*, 93:216–231.

GABRIELS, P., Snieder R., Nolet, G. (1987). In situ measurements of shear-wave velocity in sediments with higher-mode Rayleigh waves. *Geophys. Prospect*., vol. 35, pp. 187-196

GAFFET, F. (1998). A dense array experiment for the observation of waveform perturbations. *Soil Dynamics and Earthquake Engineering*, 17:475 – 484.

GALLI, P., (2000). New empirical relationships between magnitude and distance for liquefaction. *Tectonophysics*. 324, 169-187.

GAUDIOSI, J., Caserta, A., Porco, A., Govoni, A., Galli, G., Piersanti, M. (2015). Frequencies identification from ambient vibration data in a masonry heritage building. *Il Giornale delle Prove non Distruttive Monitoraggio Diagnostica,* 1/2015.

GOLDSTEIN, P., and Archuleta, R. J. (1987). Array analysis of seismic signals *Geophysical Research Letters,* vol. 14, no. 1, 13-16.

GRAFF, K. F. Wave motion in elastic solids, Dover, 1991.

HARDIN, B. O., and Drnevich, V. P. (1972a), Shear modulus and damping in soils: Measurement and parameter effects. *J. Soil Mech. Foundation Eng. Div. ASCE,* 98(6), 603-624.

HARDIN, B. O., and Drnevich, V. P. (1972b), Shear modulus and damping in soils: Design equations and curves. *J. Soil Mech. Foundation Eng. Div. ASCE,* 98(7), 667-692.

HAUBRICH, R. (1968). Array Design. *Bulletin of the Seismological Society of America,* vol. 58 no. 3, 977-991.

IDRISS, I. M., (1990). Response of Soft Soil Sites during Earthquakes. *Proceedings, Memorial Symposium to honor Professor Harry Bolton Seed*, Berkeley, California, Vol. II, May.

IWASAKI, T., Tatsuoka, F., Takagi, Y. (1976). *Dynamic Shear Deformation Properties of Sand for Wide Strain Range.* Tokyo, Japan: Civil Engineering Institue, Ministry of Construction.

JIMENEZ, M.J., Garcia-Fernandez, M., Zonno, G., Cella, F. (2000). Mapping soil effects in Barcelona, Spain, through an integrated GIS environment. *Soil Dyn Earthq Eng* 19:289–301.

JOHNSON DON, H., and Dudgeon, D. E. Array Signal Processing, concepts and techniques, PTR PH.

KANAI, K., and Tanaka T. (1961). On Microtremors VIII. *Bull. Earthquake Res. Inst. Tokyo Univ.* 39, 97 – 114.

KIND, F. (2002). Development of microzonation methods: application to Basle, Switzerland. PhD thesis, Swiss Federal Institute of Technology, Zurich, Switzerland. Dissertation ETH No. 14548.

KIND. F., Fäh D., Giardini D. (2005). Array Measurements of *S*-wave Velocities from Ambient Vibrations**.** *Geophys. J. Int.* 160, 114–126.

KONNO, K. and Ohmachi T. (1998). Ground-motion characteristics estimated from spectral ratio between horizontal and vertical components of microtremor. *Bulletin of the Seismological Society of America,* 88-1, 228-241.

LACOSS, R. T., Kelly, E. J. and Toksoz, M. N. (1969). Estimation of seismic noise structure using arrays. *Geophysics,* 34, 21-38.

LANZAFAME, G., and Tortorici, L., (1981). La tettonica recente del Fiume Crati (Calabria). *Geografia Fisica e Dinamica Quaternaria* 4, 11–21.

LANZO, C., Silvestri, F. Risposta Sismica Locale (1999), Hevelius Edizioni.

LERMO J., Chávez-García F. J., (1993). Site Effect Evaluation Using Spectral Ratios with only one Station, *Bullettin of the Seismological Society of America*, 83, n.5, pp. 1574-1594.

MALISCHEWSKY P. and Scherbaum, F. (2004). Love's formula and H/V-ratio (ellipticity) of Rayleigh waves. *Wave Motion,* 40-1, 57-67.

MELETTI C., and Valensise G., (2004). "Zonazione Sismogenetica ZS9" – App.2 al Rapporto Conclusivo, Appendice 2 al documento "Redazione della Mappa di Pericolosità Sismica prevista dall' Ordinanza PCM del 20 marzo 2003, n. 3274, All.1" – Rapporto Conclusivo, Istituto Nazionale di Geofisica e Vulcanologia, http://zonesismiche.mi.ingv.it/.

MONACO C., Tortorici L., (2000). Active faulting in the Calabrian Arc and eastern Sicily. *Journal of Geodynamic*s 29, 407–424.

NAKAMURA, Y. (1989). A method for dynamic characteristics estimation of subsurface using microtremor on ground surface. *Q. Rep. Railway Tech. Res. Inst., 30(1), 25-33.*

NAKAMURA, Y. (2000). Clear identification of fundamental idea of Nakamura's technique and its applications, in *Proc. 12th World Conference on the Earthquake Engineering*, Auckland, New Zealand.

NOGOSHI, M., and Igarashi T. (1971). On the amplitude characteristic of microtremor (part 2) (in Japanese with English abstract). *J. Seismol. Soc. Jpn.*, 24, 26–40.

NOVOTNY, O. (1999). Seismic Surface Waves. Lecture notes for post-graduate studies, Instituto de Fisica, Instituto de Geosciencias.

NTC (2008). Approvazione delle nuove norme tecniche per le costruzioni. Gazzetta Ufficiale della Repubblica Italiana, n. 29 del 4 febbraio 2008-Suppl. Ordinario n. 30, in Italian.

OLSEN, R. S. (1997). Cyclic liquefaction based on the cone penetrometer test. *Proc., NCEER Workshop on Evaluation of Liquefaction Resistance of Soils, Tech. Rep. NCEER-97-0022*, T. L. Youd and I. M. Idriss, eds., National Center for Earthquake Engineering Research, Buffalo, 225–276.

PANZA, G. F., Alvarez, L, Aoudia, A., Ayadi, A., Benhallou, H., Benouar, D., Bus Z., Chen, Y., Cioflan, C., Ding, Z., El-Sayed, A., Garcia, J., Garofalo, B., Gorshkov, A., Gribovszki, K., Harbi, A., Hatzidimitriou, P., Herak, M., Kouteva, M., Kuzntzov, I., Lokmer, I., Maouche, S., Marmureanu, G., Matova, M., Natale, M., Nunziata, C., Parvez, I., Pasckaleva, I, Pico, R., Radulian, M., Romanelli, F., Soloviev, A., Suhadolc, P., Szeidovitz, G., Triantafyllidis, P., Vaccari, F. (2004). Realistic modelling of seismic input for megacities and large urban areas. *J. Tecch. Environ. Geol.* 1:6–42.

PARK, C.B., Miller, R.D., and Xia, J. (1999). Multimodal Analysis of High Frequency Surface Waves. *The Symposium on the Application of Geophysics to Engineering and Environmental Problems*, Conference Proceedings, March 14-18, Oakland, CA, 115- 121.

PICOZZI, M., Parolai, S., Richwalski S. M. (2005). Joint inversion of H/V ratios and Dispersion Curves from Seismic Noise: Estimating the S-wave Velocity of Bedrock *Gephysical Research Letters*. (32).

RAPTAKIS, D., Makra, K., Anastasiadis, A., Pitilakis, K. (2004). Complex site effects in Thessaloniki (Greece): soil structure and comparison of observations with 1D analysis. *Bull. Earthquake Eng.* 2:271–300.

RAYLEIGH, L., (1985). On waves propagated along the plane surface of an elastic solid. *Proceeding of the Mathematical Society of London*, vol. 17, 4-11.

ROBERTSON, P. K., and Wride, C. E. (1998). Evaluating cyclic liquefaction potential using the cone penetration test. *Can. Geotech. J.*, Ottawa, 35(3), 442–459.

SAMBRIDGE, M. (1999a). Geophysical inversion with a neighbourhood algorithm—I. Searching a parameter space. *Geophys. J. Int.,* 138**,** 479– 494.

SAMBRIDGE, M. (1999b). Geophysical inversion with a neighbourhood algorithm—II. Appraising the ensemble. *Geophys. J. Int.,* 138**,** 727–746.

SATOH T., Kawase H., and ShinIchi, M. (2001). Estimation of S-wave velocity structures in and around the Sendai Basin, Japan, using arrays records of microtremors. *Bulletin of the Seismological Society of America*, 91(2): 206 – 218.

SEED, H. B., and Idriss, I. M. (1970). *Moduli and Dynamic Factors for Dynamic Response Analyses.* University of California, Berkeley: Earthquake Engineering Research Center.

SEED, H.B. and Idriss, I.M. (1971). Simplified procedure for evaluating soil liquefaction potential. *J. Geotech. Engrg. Div., ASCE*, 97(9), 1249–1273.

SEED, H. B. (1979). 'Soil liquefaction and cyclic mobility evaluation for level ground during earthquakes.' *J. Geotech. Engrg. Div.*, ASCE, 105(2), 201–255.

SEED, H. B., and Idriss, I. M. (1982). *Ground motions and soil liquefaction during earthquakes*, Earthquake Engineering Research Institute, Berkeley, Calif.

SEED, H. B., Idriss, I. M., and Arango, I. (1983). Evaluation of liquefaction potential using field performance data. *J. Geotech. Engrg.*, ASCE, 109(3), 458–482.

SEED, H. B., Tokimatsu, K., Harder, L. F., and Chung, R. M. (1985). The influence of SPT procedures in soil liquefaction resistance evaluations. *J. Geotech. Engrg.*, ASCE, 111(12), 1425–1445.

SEED, H. B., and de Alba, P. (1986). Use of SPT and CPT tests for evaluating the liquefaction resistance of sands. *Use of in situ tests in geotechnical engineering, Geotech. Spec. Publ.* No. 6, ASCE, New York, 1249–1273.

SESAME European research project WP03 – Deliverable D09.03 (2003). H/V Technique: Data Processing Report on the Multiplatform H/V Processing Software J-SESAME.

SESAME European research project WP12 – Deliverable D23.12 (2004). Guidelines for the implementation of the H/V spectral ratio on ambient vibration measurements: processing and interpretation.

SESAME European research project WP06 – Deliverable D18.06 (2004). User Manual for Software Package CAP A Continuous Array Processing toolkit for ambient vibration Array analysis.

SESAME European research project WP06 – Deliverable D19.06 (2005). Report on FK/SPAC Capabilities and Limitations University of Potsdam, Germany. Derivation of dispersion curves.

SESAME European research project WP13 – Deliverable D24.16 (2005). Recommendations for quality array measurements and processing.

SHERBAUM, F., Riepl, J., Bettig, B., Ohnberger, M., Cornou, C., Cotton F., and Bard P.-Y. (2003). Dense array measurements of ambient vibrations in the Grenoble basin to study local site effects. *EOS transaction AGU*, 80(46):F707.

SOCCO, L., and Strobbia, C. (2004). Surface wave methods for near-surface characterisation, a tutorial. *Near surface Geophysics*, 2, 165-185.

SPINA V., Tondi E., Galli P., Mazzoli S., (2009). Fault propagation in a seismic gap area (northern Calabria, Italy): implication for seismic hazard. *Tectonophysics* 476, 357–369.

SPINA V., E. Tondi, and S. Mazzoli, S. (2011). Complex basin development in a wrench-dominated back-arc area: Tectonic evolution of the Crati Basin, Calabria, Italy, *J. Geodynamics*, 51, 90-109.

STARK, T. D., and Olson, S. M. (1995). Liquefaction resistance using CPT and field case histories. *J. Geotech. Engrg.*, ASCE, 121(12), 856–869.

STEPHENSON, W.R, (2003). Factors bounding prograde Rayleigh-wave particle motion in a soft-soil layer, *Pacific Conference on Earthquake Engineering*, Christchurch, New Zealand.

STOKOE, K. H., II, Nazarian, S., Rix, G. J., Sanchez-Salinero, I., Sheu, J.-C., and Mok, Y. J. (1988a). In situ seismic testing of hard-to-sample soils by surface wave method. *Earthquake engineering and soil dynamics II – Recent advances in ground-motion evaluation, Geotech. Spec. Publ. No. 20*, J. L. Von Thun, ed., ASCE, New York, 264–289.

STOKOE, K. H., II, Roesset, J. M., Bierschwale, J. G., and Aouad, M. (1988b). Liquefaction potential of sands from shear wave velocity. *Proc., 9th World Conf. on Earthquake Engrg.*, Vol. III, 213–218.

STUCCHI, M., R. Camassi, A. Rovida, M. Locati, E. Ercolani, C. Meletti, P. Migliavacca, F. Bernardini and R. Azzaro 2007 DBMI04, il database delle osservazioni macrosismiche dei terremoti italiani utilizzate per la compilazione del catalogo parametrico CPTI04. INGV Milano. http://emidius.mi.ingv.it/DBMI04/.

SYKORA, D. W. (1987). Creation of a data base of seismic shear wave velocities for correlation analysis. *Geotech. Lab. Miscellaneous Paper GL-87-26*, U.S. Army Engineer Waterways Experiment Station, Vicksburg, Miss.

TANSI C., Iovine G., Folino Gallo M., (2005a). Tettonica attiva e recente, e manifestazioni gravitative profonde, lungo il bordo orientale del graben del Fiume Crati (Calabria Settentrionale) (Present and recent tectonics, and deep-gravitational phenomena, along the eastern boundary of the R. Crati graben (Northern Calabria)). *Bollettino della Società Geologica Italiana* 124 (3), 563–578.

TANSI, C., Tallarico A., Iovine G., Folino Gallo, Falcone, G., (2005b). Interpretation of radon anomalies in seismotectonic and tectonic-gravitational settings: the south-eastern Crati graben (Northern Calabria, Italy). *Tectonophysics* 396, 181–193.

TANSI C., Muto F., Critelli S., Iovine G., (2007). Neogene-Quaternary strike-slip tectonics in the central Calabrian Arc (southern Italy). *Journal of Geodynamics* 43, 393–414.

TARANTOLA, A. Inverse Problem Theory and Methods for Models Parameters Estimation, SIAM.

TIBERTI M.M., D'Amico M., Russo E., Pacor F., Basili R. (2014). PON – MASSIMO (Monitoraggio in Area Sismica di Sistemi Monumentali), Unità di Ricerca Analisi delle sorgenti sismogenetiche, *Rapporto tecnico sugli stati d'avanzamento intermedi* (n.3 dal 01/06/2013 al 30/11/2013), p. 1-23.

TOKIMATSU, K., and Uchida, A. (1990). Correlation between liquefaction resistance and shear wave velocity. *Soils and Found.*, Tokyo, 30(2), 33–42.

TOKIMATSU K. (1995). Geotechnical site characterization using surface waves, in the *Proceedings of the 1st Intl. Conf. Earthquake Geotechincal Engineering*, edited by K. Ishihara, pp. 1333– 1368, Balkema, Leiden.

TORTORICI L., Monaco, Tansi, C., and Cocina O. (1995). Recent and active tectonics in the Calabrian arc (South Italy), *Tectonophysics,* 243, 37-55.

TORTORICI, G., Bianca, M., Monaco, C., Tortorici, L., Tansi, C., De Guidi, G., Catalano, S., (2002). Quaternary normal faulting and marine terracing in the area of Capo Vaticano and S. Eufemia plain (Southern Calabria). *Studi Geologici Camerti* 1, 155–171.

VAN DIJK, J. P., Bello M., Brancaleoni, G. P., Cantarella G., Costa, V., Frixa, A., F. Golfetto, F., Merlini S., Riva, M., Torricelli, S., Toscano, C., Zerilli, A. (2000). A regional structural model for the northern sector of the Calabrian Arc (southern Italy). *Tectonophysics,* 324, 267-320.

VUCETIC, M., and R, D. (1991). Effect of Soil Plasticity on Cyclic Response. *Journal of the Geotechnical Engineering Division, ASCE*, 89-107.

VUCETIC, M. (1994). Cyclic threshold shear strains in soils. *J. Geotechnical Eng.*, vol. 120 (12), ASCE, pp. 2208-2228.

WATHELET M., (2005). Array Recordings of Ambient Vibrations: Surface-Wave Inversion, Doctoral Thesis, *Université de Liège, Faculté des Sciences Appliquées*.

WATHELET, M., (2008). An improved neighborhood algorithm: parameter conditions and dynamic scaling. *Geophysical Research Letters,* 35.

WATHELET M., Jongmans D., Ohrnberger M., (2004). Surface-Wave Inversion Using a Direct Search Algorithm and its Application to Ambient Vibration Measurements, *Near Surface Geophysics,* 211-221.

WATHELET, M., (2005). Array recordings of ambient vibrations: surface-wave inversion. *Doctoral Thesis*, Université de Liège.

WATHELET, M., Jongmans D., Ohrnberger M., Bonnefoit-Claudet S., (2008). Array performances for ambient vibrations on a shallow structure and consequences over *Vs* inversion, *J. Seismol.*, 12:1–19 DOI 10.1007/s10950-007-9067-x.

WOODS, J. W., and Lintz P. R. (1973). Plane waves at small arrays. *Geophysics,* 38(6), 1023-1041.

XIA, J., Miller, R. D. and Park, C. B. (1999). Estimation of near-surface shear-wave velocity by inversion of Rayleigh waves. *Geophysics* 64(3), 691-700.

XIA, J., Miller, R. D., Park, C. B., and Ivanov, J. (2000). Construction of 2-D vertical shear-wave velocity field by the multichannel analysis of surface wave technique. In the *Proceedings of the Symposium on the Application of Geophysics to Engineering and Environmental Problems* Arlington, Va., February 20-24, p. 1197–1206.

YOKOTA K., Imai, T., Konno M. (1981). Dynamic deformation characteristics of soils determined by laboratory tests. *OYO Technical Report,* No. 3 – 1981, pp. 13-36.

YOUD, T. L., et al. (1997). Summary report. *Proc., NCEER Workshop on Evaluation of Liquefaction Resistance of Soils, Tech. Rep. NCEER- 97-0022*, T. L. Youd and I. M. Idriss, eds., National Center for Earthquake Engineering Research, Buffalo, 1–40.